Harald Matthias Fitzek, Dipl.-Ing., BSc

A new simulation method for Surface-Enhanced Raman Spectroscopy applicable to rough and highly irregular substrates

DOCTORAL THESIS

to achieve the university degree of

Doktor der technischen Wissenschaften

submitted to

Graz University of Technology

Supervisor

Dipl.-Ing., Dr.techn. Univ.-Doz., Peter Pölt

Institute of Electron Microscopy and Nanoanalysis

Graz, September 2018

AFFIDAVIT

I declare that I have authored this thesis independently, that I have not used other than the declared sources/resources, and that I have explicitly indicated all material which has been quoted either literally or by content from the sources used. The text document uploaded to TUGRAZonline is identical to the present doctoral thesis.

Date

Signature

Acknowledgment

Am Beginn möchte ich all jenen danken die mir, direkt oder indirekt, bei der Erstellung dieser Arbeit geholfen haben. Hierbei handelt es sich natürlich um eine lange Liste und ich entschuldige mich gleich einmal bei allen die ich vergesse zu erwähnen. Zu meiner Verteidigung, ich schreibe diese Zeilen ganz am Schluss und bin des langen ausschweifenden Schreibens zu diesem Zeitpunkt auch schon ziemlich überdrüssig.
Beginnen möchte ich mit den wunderbaren Menschen mit denen ich in den letzten Jahren zusammengearbeitet habe. Peter, du hast mich die ganze Zeit hindurch bestens unterstützt und wenn ich nachdem gehe was ich von vielen anderen Dissertanten so höre, bis du einer der besten Betreuer. Johannes, ohne die wunderbare Zeit die ich während der Diplomarbeit bei dir hatte hätte ich diese Arbeit vermutlich nie begonnen. Hartmuth und Ferdinand, danke für die wunderbare organisatorische Unterstützung und die vielen Freiheiten die ihr euren Mitarbeitern lasst. Thomas und Jürgen, ihr hab sehr viel Geduld mit mir bei der Einschulung am AFM gehabt. Judith, Angelina, Roland, Robert, Robert II, Robert III, Jürgen, Lukas, Thomas, Manfred, Daniel, Georg, Franz, Regina, Martina, Evelin, Stefan, Cornelia, David und Johanna danke für die vielen entspannenden Kaffeepausen, Feiern und anderen Freizeitaktivitäten der letzten Jahre. Johanna, danke für die Email mit dem Vorschlag für einen Stammtisch, die du mir gestern geschickt hast, jeder der in der Liste oben fehlt ist jetzt deine Schuld ;).
Als nächstes möchte ich meiner Familie danken. Bernhard und Christine (oder Mama und Papa, normalerweise verwende ich nicht euer Vornamen aber Symmetrie in der Satzstruktur und so) danke für die großartige Unterstützung während meines ganzen Lebens und die wohl doch ganz erfolgreiche Erziehung. Andreas (inklusive Verena, Hanna und Alexander), danke für die schöne Ablenkung vom Alltag die jeder Besuch bei euch ist.
Abschließend möchte ich meinen besten Freunden danken. Lukas, Bettina und Bernhard danke, dass ich so viel Zeit mit so wunderbare Menschen wie euch verbringen kann. Ja ich weiß es ist nicht besonders spezifisch, aber es ist spät und ich weiß ihr werdet das verstehen.

Kurzfassung

In den meisten Simulationen, die sich mit der Berechnung der elektrischen Nahfelder im Zusammenhang mit oberflächenverstärkter Ramanspektroskopie (SERS) beschäftigen, wird nicht die tatsächliche Geometrie der Nanostrukturen berücksichtigt. Dies hat zweierlei Gründe. Einerseits sind sehr genaue mikroskopische Messungen von 3D-Nanostrukturen eine große experimentelle Herausforderung, andererseits benötigen Computersimulationen von komplexen Geometrien eine beträchtliche Rechenleistung und diese sind weiters schwerer in die Software zu implementieren. In den meisten Fällen wird daher eine vereinfachte Geometrie der die Oberflächenverstärkung verursachenden Nanostruktur angenommen. In dieser Arbeit wird ein Simulationsansatz vorgestellt, der die tatsächliche Geometrie, so genau wie sie gemessen werden kann, verwendet. Dies ist besonders interessant in Hinblick auf die Tatsache, dass der größte Teil der Verstärkung auf die elektrischen Nahfelder zurückzuführen ist. Weiters sind auch die Depolarisierung der Raman-Streuung und Effekte betreffend der Molekülorientierung nur mit Hilfe von exakt bekannten elektrische Nahfeldern erklärbar.
Die Zielsetzung dieser Arbeit wurde in zwei Schritten erreicht, zunächst musste die 3D-Nanostruktur so präzise wie möglich vermessen werden, dann musste das elektromagnetische Streuproblem für die vermessene Geometrie gelöst werden. Die Vermessung der Nanostruktur wurde mittels Rasterkraftmikroskopie (AFM) und Rasterelektronenmikroskopie (SEM) durchgeführt. Hierbei wurde das AFM zur Charakterisierung der 3D-Strukutur der Oberfläche eingesetzt, während SEM-Messungen zur Abschätzung und Minimierung des Einfluss der Spitzenfaltung herangezogen wurde. Für die Implementation der Oberflächenstruktur in die Simulationssoftware wurde zunächst ein Matlab-Skript programmiert, dass aus einer AFM-Messung ein 3D Modell der Nanostruktur auf einem diskreten Gitter erstellt. Dieses Model hat eine höhere Pixelauflösung als die AFM-Messung, wodurch die vollständige Information der Messung erhalten bleibt. Die elektrischen Nahfelder konnten auf diesem Gitter dann mittels einer selbst programmierten Implementierung der diskreten Dipolnäherung (DDA) berechnet werden.

Die DDA-Implementierung wurde ausgiebig getestet und für diese spezielle Anwendung optimiert.
Dieser kombinierte Ansatz aus AFM-Messungen und DDA-Simulationen wurde auf selbst hergestellten Substraten mit sehr rauer Oberflächenstruktur getestet. Diese Substrate werden mittels Sputtern von Au auf Si-Wafern und anschließendem Ausheizen dieser Sputterschichten hergestellt. Bei diesem Herstellungsprozess entstehen SERS-aktive Au-Nanoinseln, welche eine besondere Herausforderung sowohl für die AFM-Messungen (wegen der Größenverteilung) als auch für die DDA-Simulationen (da keine Regelmäßigkeiten oder fixen Begrenzungen vorliegen) darstellen. Die betreffenden Substrate wurden mit einer Monolage von 4-Methylbenzenethiol funktionalisiert, und daraufhin die Verstärkungsfaktoren und die Depolarisierung der Raman-Streuung gemessen und mit den berechneten Werten verglichen. Für die berechneten und gemessenen Werte der Depolarisierung der Raman-Streuung ergab sich eine sehr gute Übereinstimmung, während die Verstärkungsfaktoren von Banden ohne chemische Verstärkung innerhalb eines Faktors von 2 vorhergesagt werden konnten. Diese ausgezeichneten Ergebnisse beweisen, dass der hier gewählte Ansatz eine gute Möglichkeit zur Untersuchung von SERS-Substraten und der Voraussage der Höhe der damit erreichbaren Verstärkung darstellt. Die Übertragbarkeit dieses Ansatzes auf andere Substrate wird hauptsächlich davon abhängen, ob mikroskopische Charakterisierungen dieser Substrate mit hinreichender Qualität möglich sind.

Abstract

In simulations of the electric nearfields in connection with surface-enhanced Raman spectroscopy (SERS), usually a profound gap exists between the geometry that is being used in the simulations and the geometry of the real nanostructure. The underlying cause is that in case of highly irregular substrate structures a full and precise 3D microscopic characterization of the respective structures is extremely challenging, and additionally simulations of complex geometries are computationally expensive and difficult to implement. It is thus common practice to assume a simplified geometry of the nanostructures, causing the surface enhancement. In this thesis an approach is presented that incorporates the real substrate geometry, best as it can be measured. This is highly desirable, as the bulk of the enhancement of the Raman signal is attributed to the nearfields, and also depolarization or orientation effects can only be fully understood with a precise determination of the underlying nearfields.

Two distinct steps were necessary to reach this aim: firstly the precise measurement of the 3D geometry of nanostructures and secondly the solution of the electromagnetic scattering problem for said nanostructures. To measure the 3D geometry, both atomic force microscopy (AFM) and scanning electron microscopy (SEM) were used. In this combination, AFM enables the 3D recording of the substrate surface, whereas SEM provides a way to assess and minimize tip convolution in connection with the image recording. Subsequently a home-made Matlab program automatically turns the AFM measurement into a discretized 3D reconstruction with a resolution higher than the pixel resolution of the AFM measurement (thus at no loss of information). Finally, the electric nearfields are calculated for this 3D discretization using a homemade implementation of the discrete dipole approximation (DDA). This implementation has been thoroughly tested and optimized for the task at hand.

This approach, combining AFM measurements and DDA simulations, was tested using homemade SERS substrates with a highly irregular surface structure. The substrates are manufactured by sputtering of Au on Si

wafers and subsequent annealing these sputter layers. This generates highly irregular SERS active Au nanoisland films, which are particularly challenging to both the image recording by AFM (because of the size distribution) and the calculations by DDA (because of the lack of periodicity and clear boundaries). Said substrates were functionalized with a monolayer of 4-methlybenzenethiol and the enhancement factors and depolarization ratios were measured and compared to the predictions from the simulations. Excellent agreement was found for the depolarization ratios, and the enhancement factors of bands without chemical enhancement were correctly predicted within a factor of 2. Thus, the predictive capabilities and accuracy of the presented approach could be demonstrated, and its application to a larger variety of SERS substrates hinges mostly on the quality of microscopic measurements that can be obtained.

Contents

Acknowledgment i

Kurzfassung ii

Abstract iv

1 Introduction 1

2 SERS substrate manufacture & characterization 3
2.1 Substrate manufacture 6
2.1.1 Sputtering Au nanoislands onto glass substrates 6
2.1.2 Self assembled monolayer deposition 10
2.1.3 Sputtering Au nanoislands onto Si substrates 15
2.2 Microscopic characterization 19
2.2.1 Atomic force microscopy on glass substrates 20
2.2.2 Atomic force microscopy & scanning electron microscopy on Si substrates 22
2.3 Measurement of the SERS enhancement factors 28
2.3.1 Determination of the effective scattering height 29
2.3.2 Reference measurements 31
2.3.3 SERS intensity measurements 34
2.3.4 Depolarization ratios 36
2.4 Summary 39

3 Near-Field simulations & calculation of SERS-EF 41
3.1 Fundamentals of the discrete dipole approximation (DDA) . . 44
3.1.1 Deriving the fundamental equation of the DDA 44
3.1.2 The integrated tensor approach 48
3.1.3 The fast Fourier transformation acceleration of the DDA 49
3.1.4 Dealing with the substrate in the DDA 54
3.2 The main DDA program 57

3.2.1 Partial tensor integration . . . 57
3.2.2 Numbering and storage convention . . . 59
3.2.3 The fast Fourier transformation acceleration algorithm 61
3.2.4 Implementation of the image approximation . . . 65
3.2.5 Generation of the 3D-discretization form an AFM image 67
3.3 Algorithm and parameter test . . . 75
3.3.1 Verification of the DDA program . . . 75
3.3.2 Choice of the discretization step size . . . 77
3.3.3 Choice of the minimal relative residuum . . . 81
3.4 Relating electric near-fields to enhancement factors . . . 85
3.5 Summary . . . 89

4 Results and Discussion **91**
4.1 Measured enhancement factors and depolarization ratios [84] . 92
4.2 Simulation results . . . 94
4.2.1 Main results [84] . . . 94
4.2.2 Detailed results (depolarization ratios) . . . 97
4.3 Simulations vs Measurement [84] . . . 102

5 Conclusion & Outlook **105**

References **109**

List of publications **117**

A Appendix **122**
A.1 Input parameter list . . . 122
A.2 Output variables & preprogrammed plots . . . 126
A.3 Source code DDA program . . . 132
A.3.1 Run file . . . 132
A.3.2 getAFM.m . . . 136
A.3.3 DDAcore.m . . . 137
A.3.4 getpar.m . . . 137
A.3.5 IAlpha.m . . . 138
A.3.6 dtight.m . . . 139
A.3.7 getInosurf.m . . . 141
A.3.8 getalpha.m . . . 142
A.3.9 getEin.m . . . 143
A.3.10 solveDDA.m . . . 144
A.3.11 conAIT.m . . . 145
A.3.12 AtimesP.m . . . 149

A.3.13 Atimesv.m 150
A.3.14 CalcC.m 150
A.3.15 NearCalc.m 152
A.3.16 NearfieldBig.m 154
A.3.17 Nearfield.m 154
A.4 Instrumentation 157
A.4.1 Raman microscope 157
A.4.2 Atomic force microscope 158
A.4.3 Scanning electron microscope 159
A.4.4 Sputter coater 160
A.4.5 Computational resources 161

Chapter 1

Introduction

Ever since its discovery in 1974 by Fleischmann et al. [1], surface enhanced Raman spectroscopy (SERS) has become a powerful analytical technique and is used in a wide range of research [2–4]. The main feature of SERS is the enhancement of the usually relatively weak Raman signal by several orders of magnitude, even to the point where single molecule Raman spectroscopy becomes possible [5]. This enhancement is accomplished by use of nanostructured substrates, and a large variety of manufacturing procedures for the respective substrates is available, ranging from rather simple methods such as sputtering [6], vapor deposition [7] or electro-chemical roughening of surfaces [8] to high-end methods such as electron beam lithography [9] or focused ion beam milling [10].
The origin of this extraordinary enhancement has been the subject of much debate over the years [11, 12]. Eventually it was concluded that the enhancement is caused by a combination of several interconnected effects, namely the amplification of the electric near fields (electromagnetic enhancement), a modification Raman tensor of the adsorbed molecule (chemical enhancement), and the orientation of the adsorbed molecule on the surface (surface selection rules) [13–16]. The main contribution, and also the only one that is (mostly) dependent on the SERS substrate and not the probe molecule, is the electromagnetic enhancement. Thus, a detailed knowledge of the electric nearfields at a given substrate is crucial for a complete understanding of SERS experiments.
It is unsurprising that computer simulations of the electric near fields are often used in SERS research, however in most cases these simulations are based on a roughly approximated geometry of the nanostructures [17–21]. In addition, fundamental properties of the enhancement are usually examined on basic geometric structures and highly ordered arrangements of such structures [22], but rarely on the more easily fabricated substrates with their

usually highly irregular structures.
The aim of this thesis is the combination of microscopic methods and computer simulations, in order to perform simulations using the actual geometry of the nanostructures, at least as far as attainable by measurements, and additionally to make it possible to readily perform simulations on highly irregular substrates. The main microscopic technique used is atomic force microscopy (AFM), because it is a highly versatile technique applicable to a wide range of substrates and providing precise 3D information about nanostructures, given that tip convolution can be minimized. Therefore, scanning electron microscopy (SEM) is applied as a secondary technique in order to assess and minimize tip convolution.
One aim of this thesis is the automated generation of a 3D discretization of the substrate surface, with a resolution higher than the pixel resolution of the AFM measurement, and the solution of the electromagnetic scattering problem on this discretization using a homemade implementation of the discrete dipole approximation (DDA). The DDA is used because its FFT-accelerated version allows for a much larger number of discretization steps compared to other versions [23], and no input apart from the target geometry, the dielectric functions of the materials involved, and the incident electric field is required [24].
Apart from the development of this approach combining microscopy and simulations, SERS substrates with highly irregular surfaces were manufactured. Sputtering and subsequent annealing of Au on cleaned Si wafers proved to provide best results concerning surface roughness and repeatability. By and large this is a simple and common way to fabricate SERS substrates [6, 25], while at the same time providing a challenging substrate consisting of highly irregular Au nanoislands. The geometry of these substrates is particularly challenging both for the AFM measurements, because of the size distribution of the structures, and also the DDA, because of the lack of periodicity and clear boundaries. Nevertheless, good agreement between simulated and measured enhancement factors and depolarization ratios on those substrates was found.

Chapter 2

SERS substrate manufacture & characterization

The aim of this thesis is the comparison of results from simulations of SERS substrates with measured enhancement factors. In order to accomplish this, the manufacture and thorough characterization of SERS substrates is necessary. This chapter will deal with the four basic experimental task that have to be mastered to reach this aim. These four tasks are the manufacture of the substrate (chapter 2.1.1 & 2.1.3), the deposition of a (monolayer of a) probe molecule on the substrate (chapter 2.1.2), the characterization of the substrate by microscopic methods (chapter 2.2) and the measurement of the SERS enhancement factors and depolarization ratios (chapter 2.3).
The first task is to manufacture nanostructures that are suitable to enhance the Raman signal (and electric near fields). Usually these nanostructures are made from Au, Ag or Cu, due to the suitable dielectric constants of those materials [26], and they need to have a suitable shape to produce strong field enhancement [27]. A great variety of methods to manufacture SERS substrates exist, ranging from advanced nanostructuring techniques such as electron beam lithography [9] or focused ion beam milling [10] to self-assembly based methods [28], and including also rather simple methods such as thin film sputtering [6], vapor deposition [7] and electro-chemical roughening of surfaces [8]. In this work thin film sputtering (and annealing) of Au was chosen for the substrate manufacture, because sputtered and annealed Au-nanoisland films are a common and simple SERS substrate. Additionally, these Au-nanoisland films are highly irregular and non-periodic, which makes the implementation of these substrates into the simulations far more challenging than that of highly ordered structures produced by more advanced methods. Thus, any simulation that succeeds in the calculation on enhancement factors using sputtered Au-nanoisland films as substrate

will likely be suitable for substrates of different structure manufactured by other methods. From a practical point of view several procedures need to be optimized to produce suitable Au-nanoisland films. These procedures include the choice of the type of substrate (glass slides and Si-wafers were tested in this thesis) and the cleaning method for the substrate surface. Additionally, the sputtering and annealing parameters (mean film thickness, sputter current, sputter pressure, annealing temperature ...) need to be optimized. Finally, the reproducibility needs to be checked. All of this is addressed in chapter 2.1.1 & 2.1.3.
The second task is the deposition of a probe molecule on the surface of the substrates, which serves for the measurement of SERS spectra. For the measurement of the enhancement factors the deposition of a perfect monolayer of the molecule at the substrate would be highly desirable [29]. The most common way of doing this is the deposition of a self-assembled monolayer (SAM) [18, 30, 31]. Apart from the practical challenges of depositing a SAM (suitable concentration of the solution + suitable cleaning of the substrate after the deposition), a molecule used to determine SERS enhancement factors (especially electro-magnetic enhancement factors) needs to fulfill some additional requirements. Firstly a conventional Raman spectrum of the molecule has to be measurable in solution, secondly the molecule should have some Raman bands with an isotropic tensor (depolarization ratio = 0 in solution [32, 33]) and thirdly the molecule should have at least one Raman band with little or no chemical enhancement (a band with the same Raman shift in solution and on the SERS substrate). Although early measurements were performed with Methylene blue and Rohdamine B, ultimately 4-methlybenzenzthiol (4-MBT), which has been used in several SERS-EH studies [30, 33] before and fulfills all the requirements mentioned above, was chosen as the probe molecule. The details of the SAM deposition are addressed in chapter 2.1.2.
The third task is the characterization of the substrates by microscopic methods. For this purpose atomic force microscopy (AFM) was chosen, because AFM is a versatile technique that can readily be applied to a wide range of SERS substrates, and also provides the 3D information necessary for the discretization of the nanostructure in the simulations. The main challenge with this method is the assessment and minimization of tip convolution. Additional scanning electron microscopy (SEM) measurements were used to assess the tip convolution and a careful choice of both the cantilever parameters (spring constant, resonance frequency, ...) and the particular tip used in the measurements helped to minimize tip convolution. The details and results of the AFM measurements are addressed in chapter 2.2.

The fourth and final task is the measurement of the SERS enhancement factors and depolarization ratios. An excellent and widely accepted procedure to do this has been outlined by [29] and that procedure is used in this thesis as well. The measurement procedure involves measuring three key quantities: the intensity of the SERS signal, the intensity of the Raman signal in a reference solution and the effective height of the scattering volume in that reference solution. Since the procedure itself is well established, the discussion in this thesis will focus on the reproducibility and error analysis of the measurements of these three key quantities. The details of the measurements of SERS enhancement factors can be found in chapter 2.3.

2.1 Substrate manufacture

The first step is the generation of a simple cleaning-sputtering-annealing procedure that produces SERS substrates with an acceptable reproducibility. This was accomplished by sputtering Au onto cleaned glass substrates and the subsequent annealing of the substrate. To get strong SERS signals finally spin coating of the sample with suitable probe molecules (RohdaminB and Methylene Blue) was necessary. The second step is the modification of this manufacturing process in such a way that it is both suitable for the measurement of SERS enhancement factors (use SAMs of non-fluorescent molecules; see chapter 2.1.2) and also for high quality AFM measurements of the surface structure (use of Si-substrates instead of glass substrates, see chapter 2.1.3). This chapter will focus on the initially established manufacturing process (chapter 2.1.1) and will then discuss the changes that were necessary to make those substrates applicable for the task at hand (chapter 2.1.2, 2.1.3).

2.1.1 Sputtering Au nanoislands onto glass substrates

In the first attempts to manufacture SERS substrates Au was sputtered onto glass substrates (glass microscope slides), as glass substrates are cheap and readily available. For these substrates the cleaning-sputtering-annealing-procedure was optimized by trial and error. But for the measurement of the enhancement factors the deposition of a probe molecule is necessary. The probe molecules used for these first attempts were RohdaminB and Methylene Blue. All results presented in this subchapter were obtained using Methylene Blue, which was spin coated onto the sample using a 10^{-4} M solution in water and a spin coating setting of 4200 rpm for 24 sec. Spin coating of blank glass slides with this solution gave a negligible Raman signal, whereas spin coating of a glass substrate coated with the Au layer yielded a high Raman (SERS) signal.
With the deposition of the probe molecule established, there were still two other requirements that demanded an optimization of the manufacturing process. Firstly, the results should be as reproducible as possible. Secondly, the sputtered Au films should not be too thick, as this might make the AFM measurement of the height of the gold structures with respect to the underlying substrate more difficult (see chapter 2.2). Note that a strong enhancement was regarded secondary and no attempts were made to optimize for particularly high enhancement factors. The manufacturing steps, which were optimized mainly by trial and error with some inspiration form literature [6, 25, 34–36], are summarized below. Note that with this

procedure it is possible to generate large batches (up to about 30) of small (1.5x1.5 cm) SERS substrates with a single sputtering process.

1. The transparent (smooth) part of a (fresh and clean!) glass microscope slide is cut into pieces of approximately 1.5x1.5 cm
2. The pieces are cleaned using the following steps:
   (a) Wipe with ultrapure isopropanol and optical fiber tissues
   (b) Dry with a CO_2 spray
   (c) Put into an ultrasonic bath using ultrapure isopropanol for 10 minutes
   (d) Dry with a CO_2 spray
3. The pieces are sputtered in the Leica ACE 600 sputter coater (appendix x) using the following parameters
   (a) Thickness: 2nm
   (b) Pressure: 0.05 mbar
   (c) Working distance: 30 mm
   (d) Tilt: 0°
   (e) Rotation: 2
   (f) Sputter current: 15 nA
4. Finally, the pieces are annealed at 200 $C°$ for 30 minutes in dry air

Since reproducibility is the main concern, extensive testing of different kinds of variations of the SERS-signal has been done. These are the variation of the SERS signal measured at different regions of different size on a single substrate, its variation as a function of the position of the substrate in the sputter coater during Au-sputtering (between samples of the same batch) and its variation with respect to subsequent sputter processes (with identical parameters).
First the variation of the SERS signal across a substrate surface was tested by recording spectral maps of the strongest Raman band of Methylene Blue (1623 cm^{-1}) on two length scales. Large mappings (0.5x0.5 mm; pixel size approximately 50 µm) were recorded using the x10 Objective (NA 0.25), a laser wavelength of 633 nm (8 mW), an acquisition time of 0.5 second (x2 accumulations) per spectra and deploying the duo scan system to ensure full

coverage of the scanned area (instrumentation see appendix A.4.1). Small mappings (40x40 µm; pixel size approximately 5 µm) were recorded using the x100 Objective (NA 0.9), a laser wavelength of 633 nm (0.16 mW), and an acquisition time of 0.5 second (x2 accumulations) per spectra. Figure 2.1 shows examples of a large and small mapping areas.

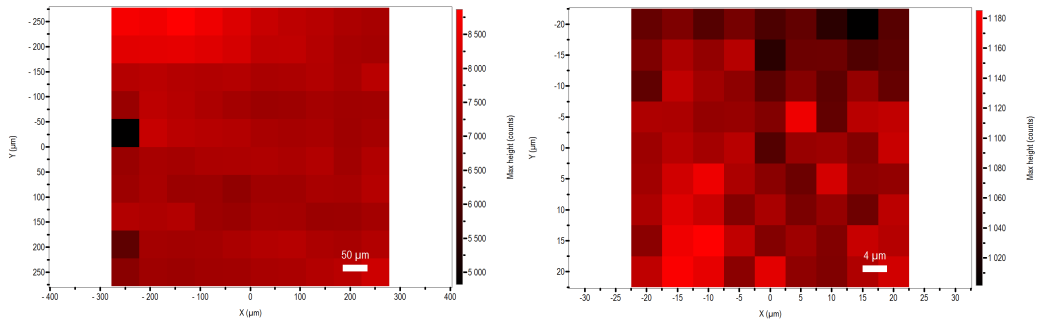

Figure 2.1: Examples of spectral mappings at a large (0.5x0.5 mm) and a small (40x40 µm) area used to determine the variation of the SERS signal across the area of a substrate

Several such mappings have been performed on samples from three different batches to estimate the variation of the SERS signal across a single substrate on two length scales. The averages of the standard deviation of the signals from those mappings are summarized in table 2.1. The overall results (3-8% variation of the SERS signal on the substrate) are comparable to what would be expected from the literature [6, 37, 38].

Table 2.1: Summary of the measurements to estimate the variation of the SERS signal on a single substrate

Batch	*LargeMaps* $\sigma(I_{1623})$	*SmallMaps* $\sigma(I_{1623})$
1	5%	3%
2	8%	4%
3	5%	5%

Secondly, the variation of the SERS signal at different substrates from the same batch (depending on the position in the sputter coater) was tested. This was done by placing 2 batches of 12 samples each at defined positions in the sputter coater. On each sample 3 mappings equivalent to the large mapping in figure 2.1 were measured and the average signal from those three mappings was calculated. The resulting average intensities

of the 1623 cm-^{1} band of Methylene Blue are plotted in figure 2.2 as a function of the position at the sample on the table of the sputter coater (instrumentation see appendix A.4.4). A clear-cut dependence of the SERS signal on the positions of the samples is not observable. The standard deviation of the signal strength as a function of sample position is 7 % for batch 1 and 12 % for batch 2 and is comparable to the deviations found for the variation on a single substrate. Additionally, it is comparable to the deviations between substrates to be expected from results published in literature [6, 37, 38]. Therefore, the positioning of the samples in the sputter coater plays only a minor role concerning the strength of the SERS signal.

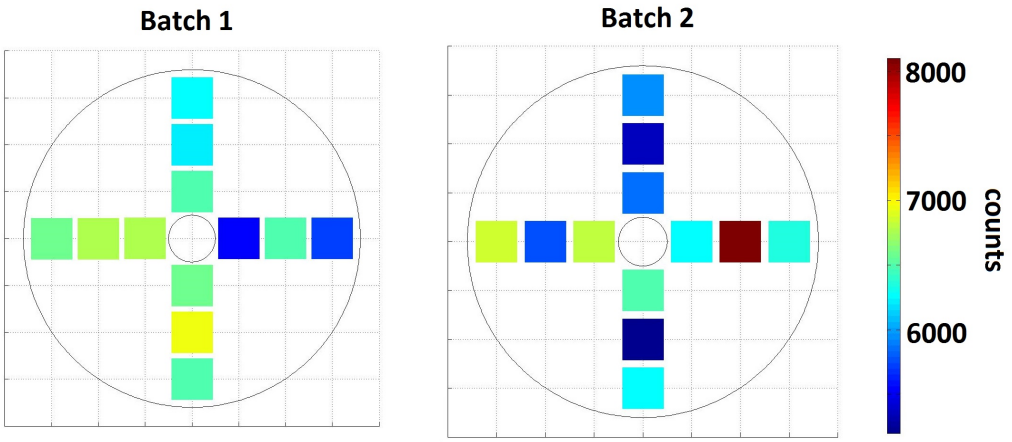

Figure 2.2: Intensity of the SERS signal of the 1623 cm^{-1} band of Methylene Blue as a function of the position of the sample on the table of the sputter for two batches

Thirdly, the variation of the SERS signal between substrates from different batches (or substrate to substrate variation) can trivially be estimated form the measurement results underlying table 2.1 and figure 2.2. It is approximately 10 %.
To sum up, a cleaning-sputtering-annealing procedure for the deposition of Au nanoislands on glass substrates that achieves good reproducibility (when spin coated with Methylene Blue) was established. However, for the determination of SERS enhancement factors the deposition of a monolayer of a not fluorescent molecule is necessary. Thus neither the strongly fluorescent Methylene Blue (or RohdaminB) nor spin coating can be used. This introduces a significant new source of uncertainty and is discussed in chapter 2.1.2. Additionally, it turned out that the replacement of the glass substrate by an

Si-wafer would be highly desirable in order to achieve a better quality regarding the AFM measurements (see chapter 2.2). However, using Si-wafers necessitated some changes in the cleaning procedure, which will be the topic of chapter 2.1.3.

2.1.2 Self assembled monolayer deposition

For the measurement of SERS enhancement factors, using the approach developed in this work (see chapter 2.3; [29]), the deposition of a monolayer of a non-fluorescent molecule on the surface of the substrate is necessary. To this aim mostly self-assembled monolayers (SAMs) were used. For this work 4-methlybenzenzthiol (4-MBT) was chosen as a probe molecule, because it forms a SAM by bonding of the molecule to Au via the SH-group. Furthermore its absorption behavior on Au has been thoroughly investigated [39, 40] (including its behavior with regard to chemical enhancement on Au [41]), and it has also been the probe molecule used in previous studies comparing DDA simulations to measured enhancement factors [30].
For a full description of the theory and application of SAMs the reader is referred to the relevant literature [42]. In brief: in the first step the molecule is deposited by immersing the substrate into an appropriate solution with the molecule in immediate contact to the Au surface, binding to it via the SH - group as indicated in figure 2.3. The second step is the removal of the molecules that did not bind to the surface by a suitable cleaning procedure.

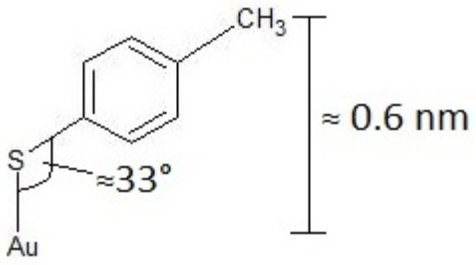

Figure 2.3: Schematic drawing, showing how a 4-MBT molecule binds to Au by replacing the S-H bond with a S-Au bond; the angle and height of the molecule is based on [39]

From a practical perspective, this means that the concentration of the solution and the immersion time must be high enough that a close to complete monolayer is formed. Whereas the cleaning procedure must be

thorough enough that no significant Raman signal is measured from excess molecules not bound to the Au, whilst being as gentle as possible to avoid damaging the substrate and monolayer.
Luckily, the Raman signal from 4-MBT bonded to Au can be clearly distinguished from the Raman signal of regular 4-MBT. This is possible because the strongest band in the Raman spectrum of 4-MBT (1100 cm^{-1}) is due to the ν(C-S) vibration and shifts significantly when the –SH is replaced by –SAu [16, 30, 43, 44]. This is demonstrated in figure 2.4 using the example of a SERS spectrum and a Raman spectrum from a solid reference of 4-MBT. Thus, the cleaning procedure was sufficient, if no Raman band at 1100 cm^{-1} is visible. Alternatively, one can also check for the Raman band at 2560 cm^{-1}, which is due to the ν(S-H) vibration, and obviously vanishes when there is no more H.

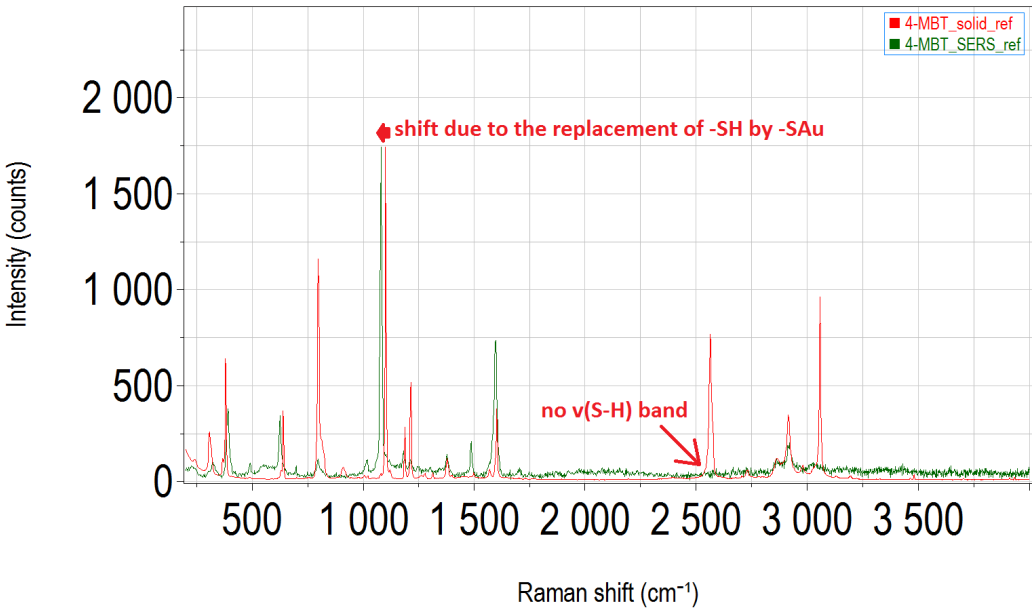

Figure 2.4: Demonstration of the shift of the Raman band at 1100 cm^{-1} of 4-MBT caused by bonding of the molecule to the Au-surface and of the missing band at 2560 cm^{-1} due to the replacement of H by Au

Inspired by examples of cleaning procedures found in literature [30, 33], a rather simple and gentle procedure was tried. Immediately after the immersion of the substrate in the 4-MBT solution, the samples were dipped into ultrapure ethanol for a couple of seconds and subsequently carefully dried with a CO_2 spray. This cleaning procedure was always sufficient to ensure that no bands at 1100 cm^{-1} and 2560 cm^{-1} were visible in the SERS

spectra. It is important to note that also the 4-MBT solution used to deposit the monolayer had a very low concentration (10^{-4}), thus minimizing the amount of excess 4-MBT on the substrate from the start.
The starting point for the determination of the concentration of the solution and the immersion time for the deposition of the monolayer were the parameters used previously for the spin coating of Methylene Blue and RohdaminB (10^{-4} M). Subsequently the concentration was varied by a couple orders of magnitude (10^{-3}-10^{-6} M), and the resulting SERS intensities were measured. A batch of 4 substrates (Au on glass, see chapter 2.1.1) was prepared, each substrate was immersed in a different solution of 4-MBT for 1 h and subsequently cleaned as stated above. Solutions of 10^{-3} M in ethanol and $10^{-4}/10^{-5}/10^{-6}$ M in water were used. The Raman spectra in figure 2.5 are the average spectra of 400x400 µm maps (10x10 pixel), which were recorded using a laser wavelength of 633 nm (4 mW), an x10 Objective (NA 0.25) and an acquisition time of 1 second (x2 accumulations) per spectrum.

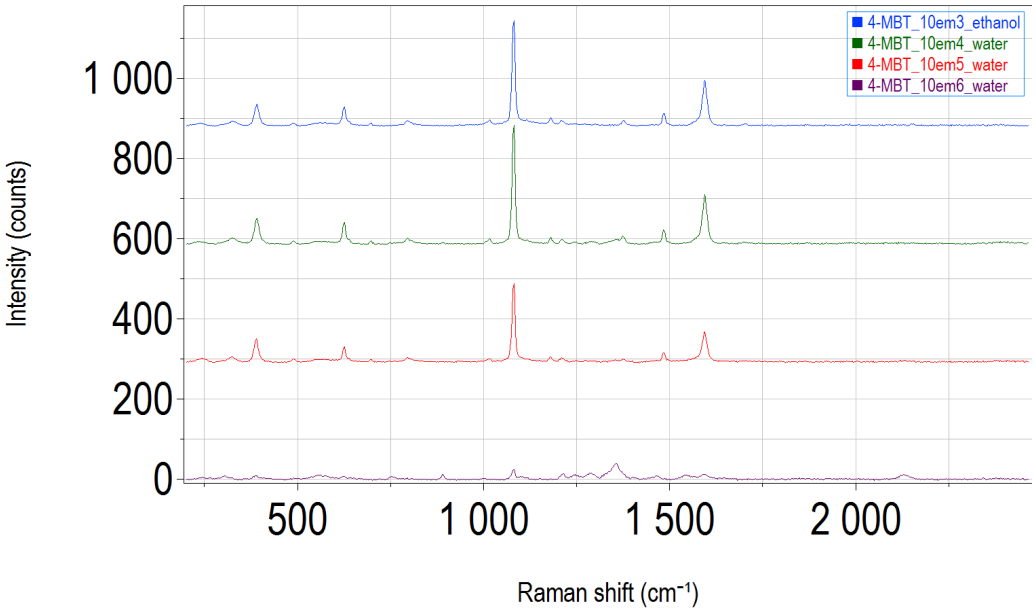

Figure 2.5: SERS intensities measured at substrates from the same batch, but immersed in different solutions of 4-MBT for 1 h and subsequently cleaned as stated above

The intensities of the SAMs gained from the immersion of the substrate in the 10^{-3} and 10^{-4} M solutions are comparable (10^{-4} M is insignificantly higher), whereas the intensity of the SAM from the 10^{-5} M solution is somewhat lower. The immersion in the 10^{-6} M solution apparently failed to

produce a monolayer as only a very small signal of 4-MBT is measureable and significant bands from contamination appear in the region between 1000-1500 cm^{-1}. Thus, a concentration of 10^{-4} M in the solution is sufficient to get a closed monolayer. Note that an as low concentration as possible should be used to avoid excess 4-MBT on the substrate.
Since there is no difference in the results gained from both the 10^{-3} and 10^{-4} M solutions, it can already be inferred that the immersion time of 1 h (at 10-4 M) is sufficient to create a saturated monolayer. However, as double check the immersion time was reduced and the resulting SERS intensities were measured. Just as above, a batch of 4 substrates (Au on glass see chapter 2.1.1) was prepared and immersed in a solution of 10^{-4} M 4-MBT in water for 1h, 30 minutes, 10 minutes and a short dip (a couple of tens of seconds). The Raman spectra in figure 2.6 are the average spectra of 200x200 µm maps (5x5 pixel), which were measured using a laser wavelength of 633 nm (4 mW), a x10 objective (NA 0.25) and an acquisition time of 16 second (x2 accumulations) per spectrum.

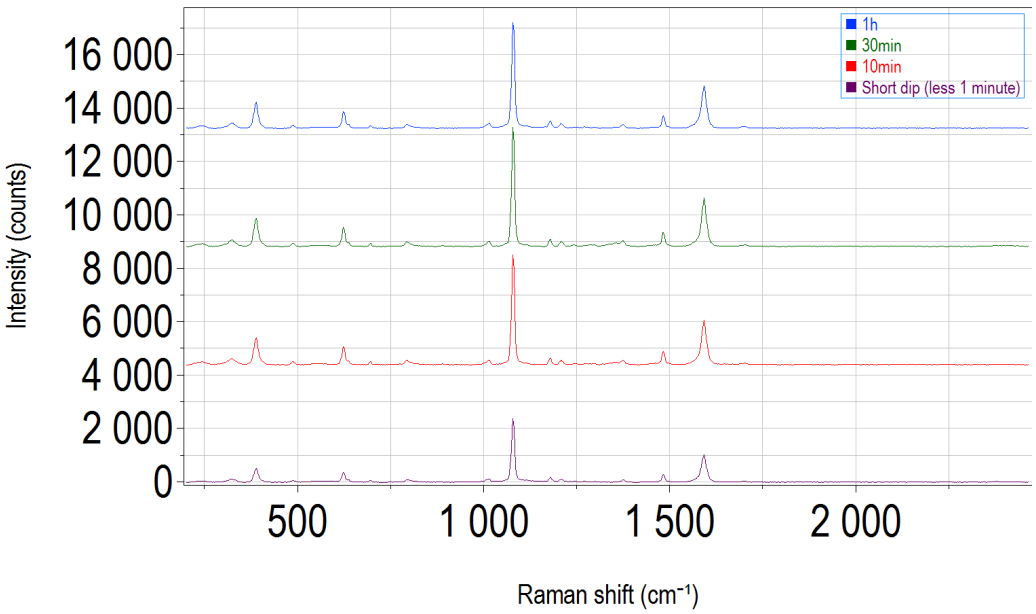

Figure 2.6: SERS intensities measured at substrates from the same batch, immersed in a solution of 10^{-4} M 4-MBT in water for 1h, 30 minutes, 10 minutes and a short dip (a couple of tens of seconds)

No significant differences in the spectra recorded from samples with immersion times of 1h, 30 minutes and 10 minutes could be observed, indicating that full coverage is reached somewhere in the range between

1 and 10 minutes. Since there was no trouble with excess 4-MBT on the substrate, an immersion time of 1h was chosen, as it is both practical (not ridiculously long) and well above the estimated time range necessary to get a saturated monolayer.
To sum up, the procedure for the deposition of the 4-MBT SAM is as follows:

1. The substrate is immersed in a 10^{-4} M solution of 4-MBT in water for 1 h
2. The substrate is dipped into ultra pure ethanol for about 10 seconds
3. The substrate is carefully dried with a CO_2 spray

To conclude the chapter on the deposition of the 4-MBT SAM, it is important to point out that using a SAM rather than a layer generated by spin coating reduced the reproducibility of the SERS signal. This is attributed to the fact that with spin coating certainly several layers are deposited, which will always lead to a saturated SERS signal (including contributions from layers other than the first one). With the SAM deposition an attempt is made to deposit a monolayer. While it is necessary to assume a perfect monolayer for the measurement of the enhancement factors and the comparison with the results from the simulations, in practice this adds a huge potential for errors, as there is no way to guarantee a perfect and closed monolayer is deposited every time. Every change in the coverage of the substrate translates directly into a change of the measured SERS intensity. Additionally Ikeda et al. [41] found a dependence of the chemical enhancement of 4-MBT on the crystallographic orientation of the Au substrate, which is impossible to control on sputtered substrates.
The variation of the signal across a single substrate using the 4-MBT SAM was assessed in a similar way as used for the spin coated samples. 400x400 µm maps (10x10 pixel) of samples with an immersion time of 10 minutes, 30 minutes and 1 h (see figure 2.6) were recorded using a laser wavelength of 633 nm (4 mW), a x10 Objective (NA 0.25) and an acquisition time of 1 second (x2 accumulations) per spectrum (comparable to the large mapping in figure 2.1). The standard deviation found in those maps was 10-18 % (compared to 5-8 % from the spin-coated samples).
To assess the variation of the signal per immersion into the 4-MBT solution, a batch of 4 samples was prepared. On each sample three 200x200 µm mapping (5x5 pixel) were measured using a laser wavelength of 633 nm (4 mW), a x10 objective (NA 0.25) and an acquisition time of 8 second (x2 accumulations) per spectrum. The average spectra of all three maps of

each sample are shown in figure 2.7. The standard deviation of the band intensities of these spectra are 17-20%.

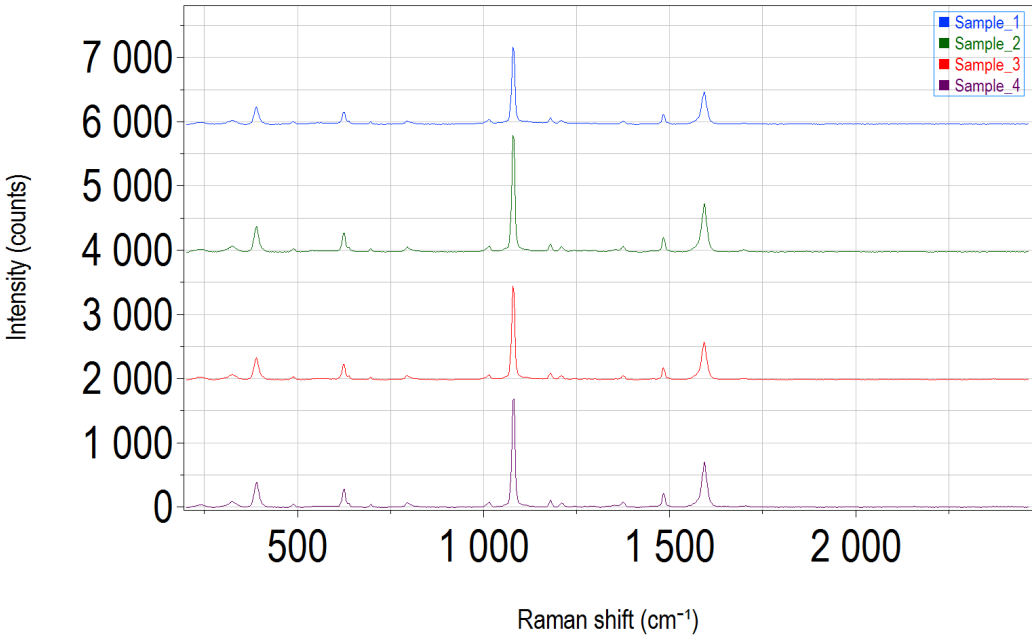

Figure 2.7: Average Raman spectra of four samples from the same batch measured in order to assess the per immersion reproducibility of the 4-MBT SAM deposition

2.1.3 Sputtering Au nanoislands onto Si substrates

As already mentioned above, the change from glass substrates to Si wafers took place in order to improve the quality of the AFM measurements (see chapter 2.2). Unfortunately, the first trials with Si wafer substrates led to highly unreproducible results. This could later be attributed to the fact, that contrary to the microscope slides, which were new and removed from the original packing, the pieces of Si wafer were cut off from samples stored in the laboratory for longer times under conditions not ideal, and therefore these wafers were already contaminated. The problem was solved by using a more elaborate cleaning procedure, and then reproducibility similar to that got with the 4-MBT SAM on glass slides was achieved. Additionally, the annealing procedure was varied by trial and error. The final procedure applied to deposit Au nanoislands on Si-substrates is summarized below.

1. Pieces with an area of approximately 1.5x1.5 cm are cut off from a Si wafer
2. The pieces are cleaned using the following steps:
   (a) Wipe with ultrapure acetone and optical fiber tissues
   (b) Dry with a CO_2 spray
   (c) Wipe with ultrapure toluene and optical fiber tissues
   (d) Dry with a CO_2 spray
   (e) Wipe with ultrapure isopropanol and optical fiber tissues
   (f) Dry with a CO_2 spray
   (g) Repeat 1-6 until no streaks are visible anymore
   (h) Put into an ultrasonic bath using ultrapure isopropanol for 10 minutes
   (i) Dry with a CO_2 spray
3. The pieces are sputtered in the Leica ACE 600 sputter coater (appendix x) using the following parameters
   (a) Thickness: 2nm
   (b) Pressure: 0.05 mbar
   (c) Working distance: 30 mm
   (d) Tilt: 0°
   (e) Rotation: 2
   (f) Sputter current: 15 nA
4. Finally,the pieces are annealed at $C°$ for 2 h in dry air

With this newly established procedure the reproducibility was assessed again in the same way as for the glass slide substrates (chapter 2.1.1), but using a 4-MBT SAM at the substrate instead of a spin coated layer. The variation of the signal across a single substrate was again measured using the approach mentioned in figure 2.1. Three 0.5x0.5 mm mappings (pixel size approximately 50 µm) were measured on three samples from the same batch respectively, using the x10 Objective (NA 0.25), a laser wavelength of 633 nm (4 mW), and an acquisition time of 1 second (x2 accumulations) per spectrum. The standard deviation of the strongest band of 4-MBT (1080 cm^{-1}) found in these mappings was around 20 %, comparable to the results

using the 4-MBT SAM on glass slide substrates.
The variation between substrates of the same batch was assessed using three batches (two batches of 4 samples and one batch of 7 samples). Again spectra of each sample were measured using the x10 Objective (NA 0.25), a laser wavelength of 633 nm (4 mW), and an acquisition time of 1 second (x16 accumulations) per spectra. The standard deviation of the strongest band of 4-MBT (1080 cm^{-1}) was 19-24 %, slightly worse than what was achieved on glass substrates but still acceptably close.
Finally, the reproducibility between batches was tested by taking the average spectrum per batch from the measurements used to determine the variation between substrates of the same batch. The results are shown in figure 2.8.

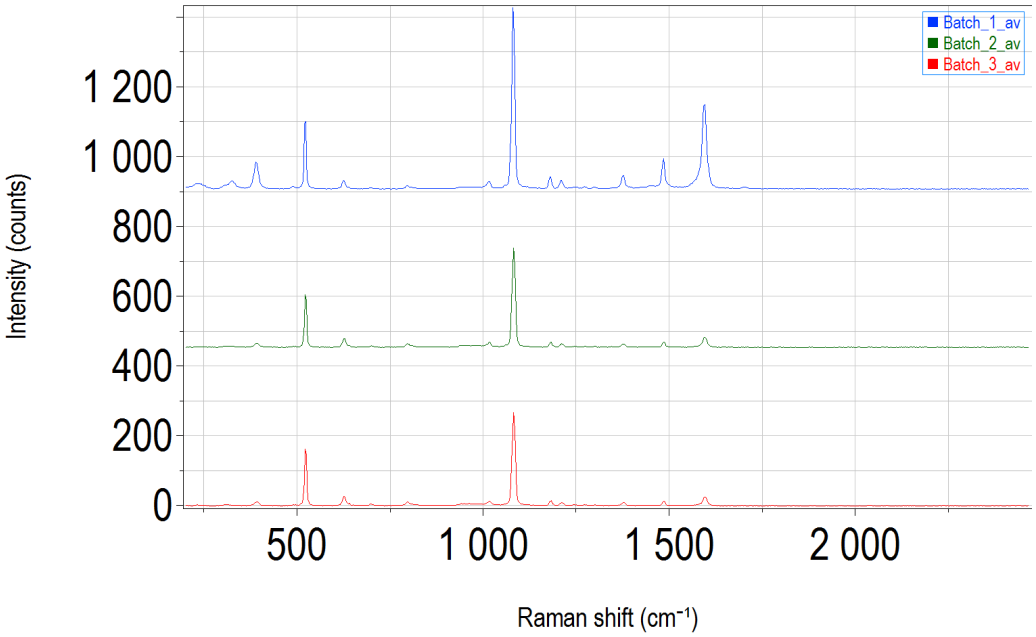

Figure 2.8: Average spectrum of each of the batches used to determine the variation between samples of the same batch

It is immediately obvious that there are large differences between samples from different batches. More importantly, the differences are not only due to an overall increase or decrease off the signal, but also due to different relative intensities between bands. Most strikingly is the change in the relative intensity between the strongest band at 1080 cm^{-1} and the usually second strongest band at 1590 cm^{-1} (Note that the band at 520 cm^{-1} is from the Si substrate). These changes in the relative intensities can be attributed to variations of the average thickness of the Au film that is sputtered onto the

substrate and consequently variations in the size of the Au nanoislands. It can be assumed that problems with the sputter coater are responsible for the variations of the film thickness, because batches that were sputtered consecutively on the same day (as batch 2 and 3 above for instance) tended to have similar spectra. Additionally, minor problems with regards to the vacuum quality and other maintenance issues of the sputter coater were observed in other experiments at the institute at the same time. The extremely thin films that were sputtered in this work are particularly vulnerable with this regard. Furthermore, substantial variations in the mean film thickness and the mean roughness between batches were confirmed by AFM measurements. This can explain the large differences in spectra from different batches, as the mean roughness has been shown to be vital to the electro-magnetic enhancement of thin Au films [25]. Additionally, the chemical enhancement of 4-MBT was shown to depend on the crystallographic orientation of the Au substrate [41], and DFT simulations have also revealed a dependence of the chemical enhancement of similar molecules on the adsorption sites [45]. Finally, it should be noted that while batch to batch reproducibility would of course be desirable, it is not critical to the task at hand, which is the comparison of the results of detailed simulations of the real geometry to measurements. Any variation in film thickness or roughness is measured by the AFM and thereby taken into account in the computer simulations.

2.2 Microscopic characterization

The microscopic characterization of the substrates was mostly done by atomic force microscopy (AFM), as 3D information about the surface topology is crucial for the implementation of the substrates into the simulations. AFM is particularly well suited for the aim of providing a combined measurement-simulation based characterization toolbox of SERS substrates, as it is a versatile technique that can provide precise information on the nm scale. AFM can readily be applied for the characterization of most SERS substrates, provided that the subjacent substrate is reasonably flat. Additionally, AFM does not require a vacuum (contrary to other techniques with sufficient resolution) and can even be applied in liquids (even for in situ studies), providing further flexibility. Unfortunately, AFM also has some drawbacks that need to be considered. For instance, AFM is incapable of properly measuring overlapping surfaces (in which case only the top surfaces can be measured), making the investigation of complex 3D structures that are sometimes seen in high-end SERS substrates [18] difficult or even impossible. Additionally, material contrast is limited and only the topmost atomic layer of the substrate can be investigated, which could be a problem if composite nanostructures [46] or core shell nanostructures [47] are used. Finally, the biggest drawback of AFM is the strong dependence of the quality of the images on the quality of the tip used. This is why strict best practice guidelines regarding the choice of the tip had to be implemented, and scanning electron microscopy (SEM) was used as a secondary microscopic technique to assess the influence of tip convolution. This chapter will focus on those best practice guidelines and present how the AFM images, that were ultimately used for the simulations, were measured. Additionally, AFM and SEM images from samples from the two batches used for the simulations will be presented.
But first a short detour will be taken, demonstrating the difficulties that were encountered with AFM imaging, when instead of Si wafers glass slides were used as substrates. All AFM images presented in this chapter were recorded with a Bruker Fast Scan Bio AFM (see appendix A.4.2), using tapping mode in an air-conditioned environment and an acoustic enclosure. A MPP-12220-10 cantilever (spring constant 5 N/m) was used for all AFM images. The data analysis, including correction steps such as background leveling and scar removal, was done in Gwyddion. Additionally, for all AFM images the set point, gain control drive amplitude and scan rate were optimized before the start of the measurements to obtain high resolution images without distortion at a low force exerted on the sample. All SEM measurements presented in this chapter were conducted with a FEI Quanta

600 ESEM (see appendix A.4.3) using the low vacuum mode (with water vapor as imaging gas). Either the large field detector (LFD, SE) or the solid-state backscatter electron detector (SSD, BSE) was used, as always indicated in the data bar of the images. All other relevant SEM parameters are also included in this data bar. For detailed information about the theory of SEM [48] and AFM [49, 50] the reader is referred to the literature.

2.2.1 Atomic force microscopy on glass substrates

As already mentioned before at first microscope glass slides were used as substrates (see chapter 2.1.1). This lead to some difficulties with the AFM measurements, which also points towards a fundamental limit when using AFM measurements in this context. This is best illustrated by showing an example of a measurement of Au nanoislands on a glass substrate (figure 2.9).

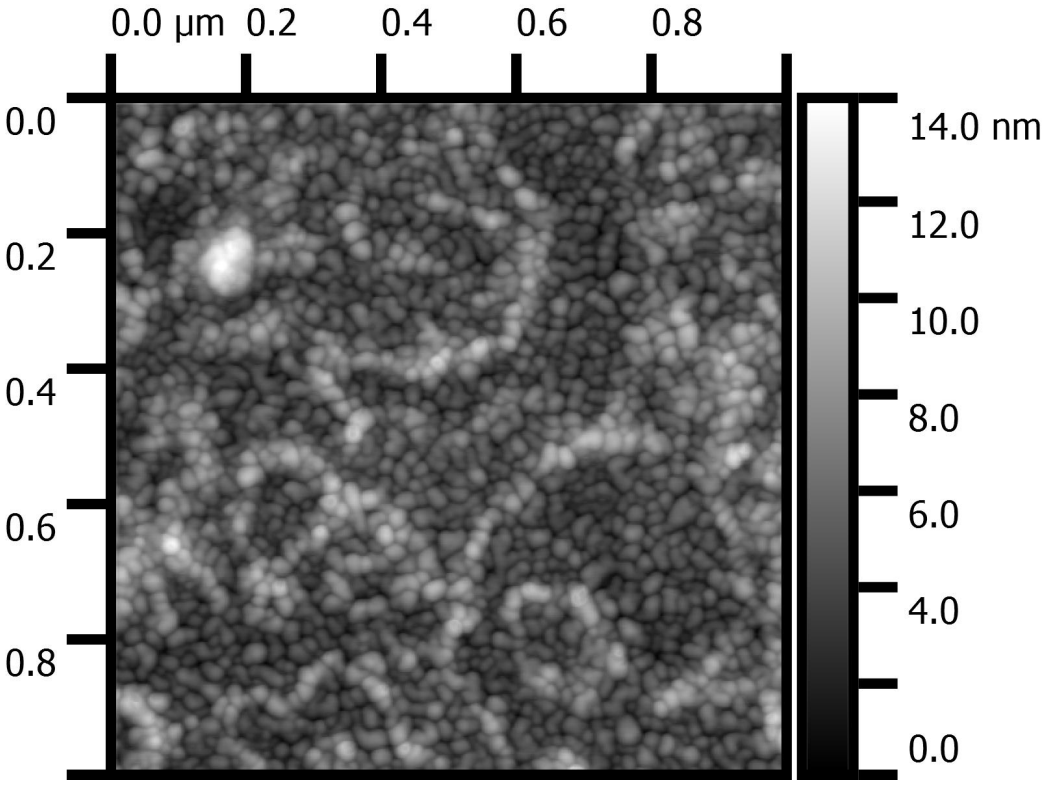

Figure 2.9: AFM image of an Au nanoisland film on a glass substrate; there appear to be large structures in addition to the nanoislands

It is obvious that the Au nanoisland film is textured by larger string and pore like structures. These structures can be attributed to the glass substrate. If the AFM images of a blank glass substrate and an Au film on a substrate are compared (figure 2.10), it becomes immediately apparent that the larger structures are due to the roughness of the glass slides.

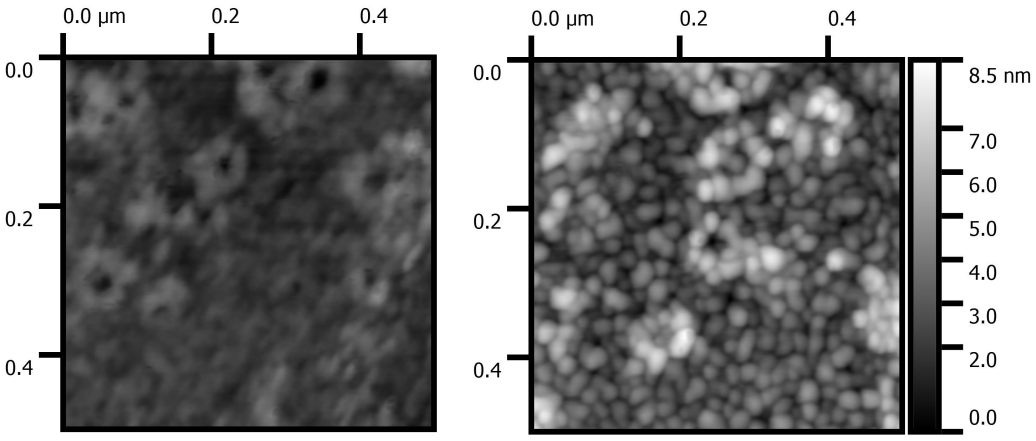

Figure 2.10: AFM image of a blank glass slide; Right: AFM image of Au nanoislands on a glass slide; both images have the same gray bar

The structures seen in the left of figure 2.10 and resulting from the roughness of the substrate have approximately the same height as the Au nanoisland (around 5 nm). Thus, the assumption of a perfectly flat substrate (as is done by the algorithm, see chapter 3.2.5) is not valid, and the surface roughness has to be dealt with in a different way. In the case of this work the glass substrates were replaced by Si wafers avoiding the problem altogether.
While this is fine in the context of this work, it points to a limiting factor of the AFM. To put it bluntly, what if simulations on a rough substrate, beneath a coating, are of importance? This is a rather interesting question, since assuming the dielectric boundary to be perfectly flat is a prerequisite for the mirror dipole approximation used in the simulation (see chapter 3.1.4). Essentially two possible approaches exist, and for both of them the first step would be an estimation of the structure of the substrate surface. This could be done for instance by marking a sufficiently large number of points situated on the substrate in the AFM image, and then fitting a suitable surface function through these points such that the resulting calculation of the surface reasonably resembles AFM images of the blank substrate. With an estimation of the substrate surface at hand, the simplest

procedure would be to subtract it from the AFM image. This of course means that a somewhat different geometry than the actual one is being simulated (due to the only estimated substrate surface) and would certainly cause some artefact in the image. The other possibility would be to put the perfectly flat substrate at the lowest point of the image implemented in the simulation and use the estimation of the surface structure to introduce an additional (rough) layer of dipoles representing the surface roughness. This would for the most part conserve the original geometry, but also necessitate some changes to the algorithm (note that neither speed nor resolution of the simulation are likely to be significantly reduced). Additionally, simulating an array of glass dipoles on top of a perfectly flat dielectric boundary of glass in the framework of the mirror dipole approximation should be thoroughly check for mathematical pit falls.
While the incorporation of rough underlying substrates into the simulation is certainly an interesting challenge for a future improvement for this work, in the present case the glass slides were replaced by near perfectly flat Si-wafers, whose characterization will now be discussed.

2.2.2 Atomic force microscopy & scanning electron microscopy on Si substrates

The best way to start this crucial chapter is a demonstration of the large influence that the tip has on AFM measurements of such delicate nanostructures as used in this work. Figure 2.11 shows two AFM images of the same sample (Batch 1, sample C from chapter 2.3.3). The right image is a high quality image recorded with a good tip which was later used for the simulation, whereas the left image was measured with a bad tip clearly showing the importance of minimizing tip convolution.

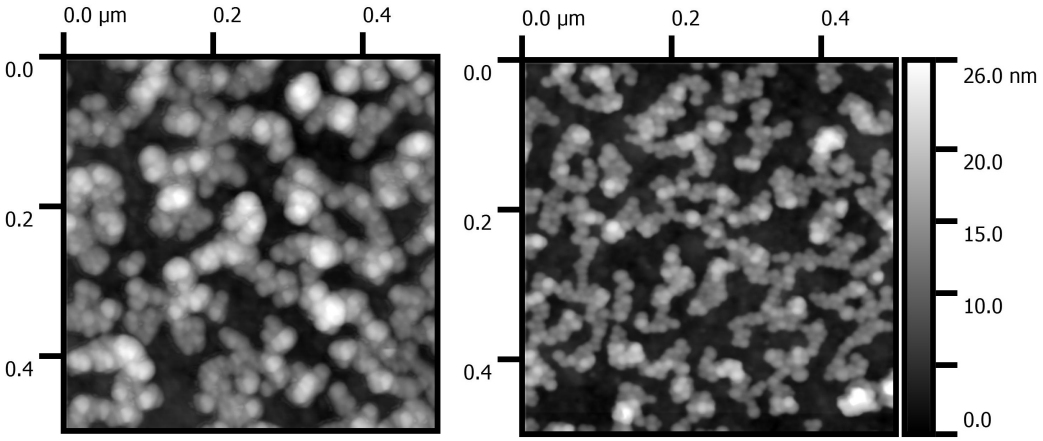

Figure 2.11: AFM images of one of the samples C from batch 1 (from chapter 2.3.3), measured with a bad tip (left) and a good tip (right)

As there is no easy way to a priori identify the quality of the tip, the large dependence of the image quality and size of the nanostructures on the tip quality makes the use of a secondary microscopic technique necessary to get some idea of the size of the nanoislands to be expected. In this work SEM was used to this end. With some idea of the general size of the nanoislands, it becomes much easier to assess the tip quality during AFM measurements (by simple inspection of the images), which both safes time and helps establish best practices guidelines to ensure good image quality.
At this point it is important to point out that the Au nanoisland films examined in this work are relatively challenging structures both for the simulations and AFM measurements. The reasons are their high irregularity and their (broad) size distribution (with some individual island being relatively small even for plasmonic nanostructures). Therefore, the procedure discussed below was developed for the AFM measurements of the Au nanoisland films, and it should translate well to other samples.
The procedure will be explained by using the example of the sample C from batch 1 (see chapter 2.3.3). The AFM images from this sample were also used for the computer simulation (see chapter 4.2 and 4.3). It is very convenient to start with SEM measurements to get a general idea of the size distribution of the nanostructures. For a later visual comparison with the AFM images an SE image of an area of about 2x2 µm turned out to be a good choice. Figure 2.12 shows an example of two SEM images recorded from batch 1, sample C (see chapter 2.3.3) before performing the AFM measurements.

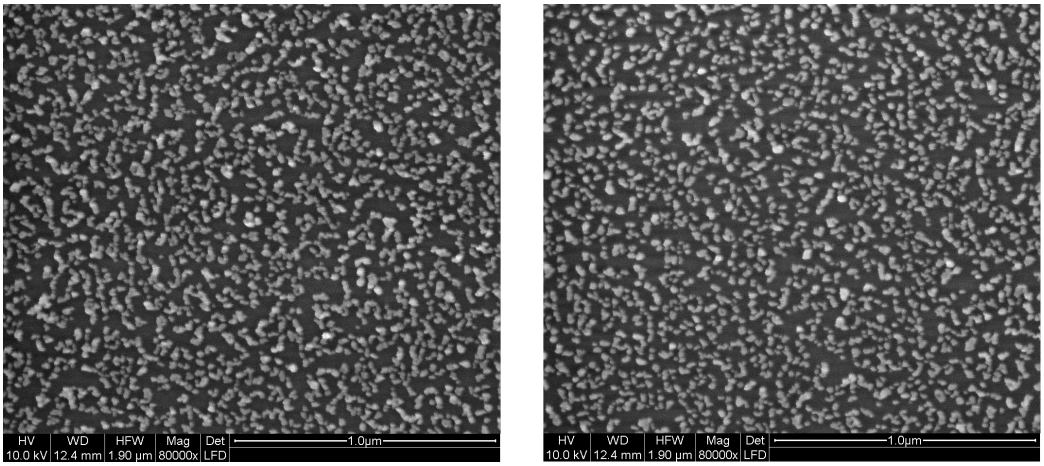

Figure 2.12: Two exemplary SEM images of batch 1, sample C (from chapter 2.3.3), taken before the recording of the AFM images to get an idea of the size distribution of the Au nanoislands

The next and often most frustrating step is the mounting of an appropriate cantilever at the scan head. The best choice of the cantilevers available was the Bruker MPP-12220-10 cantilever (spring constant 5 N/m). For the kinds of measurements reported in this work always a fresh cantilever should be used. As is standard and best practice in AFM measurements, great care must be taken when placing the cantilever at the scan head and executing the appropriate calibration steps. Should the cantilever at any point during the calibration or subsequent measurements show suspicious behavior, then it needs to be replaced immediately and the whole procedure has to start again. In addition, if the measured structures appear clearly inconsistent with those visible in the SEM images, again the whole procedure should be started again. Additionally, one must keep in mind that the tip can be damaged during measurements (by picking something up from the substrate for instance), thus a small number of images to be recorded should be defined at the start of the investigation (as a tip damage towards the end might ruin the whole session). After the respective images are taken, for checking purposes images with the same area as the SEM images (2x2 µm) should be recorded. In case of sufficient agreement with the SEM images, the AFM images taken beforehand (possibly different scale!) can be regarded of high quality as well. Figure 2.13 shows the comparison of a control image that was recorded after the AFM images of batch 1, samples C (from chapter 2.3.3) with one of the SEM images from figure 2.12. A bright colormap with multiple colors was chosen for the display of the AFM images in order to enhance the contrast between the substrate (black areas)

and the nanostructures.

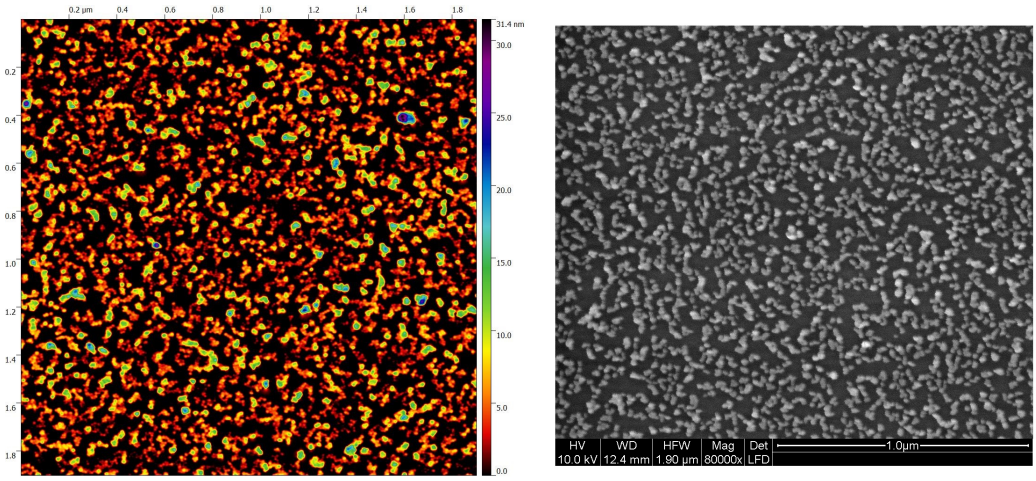

Figure 2.13: Comparison of an AFM and SEM image of batch 1, samples C (see chapter 2.3.3), the areas are approximately 2x2 µm

The sizes of the Au nanoislands in both images match very well, thus the AFM images recorded beforehand can be accepted as high-quality images suitable for the simulations. Figure 2.14 shows two examples of these high-quality images, with the right image ultimately used for the simulation with batch 1 chosen as substrate (in chapter 4.2 and 4.3). Note that the images that were used as a basis for the simulations usually had a width of 500 nm and a resolution of 512x512 pixel, which turned out to be a useful choice especially with regard to the measurement time and the quality of the images.

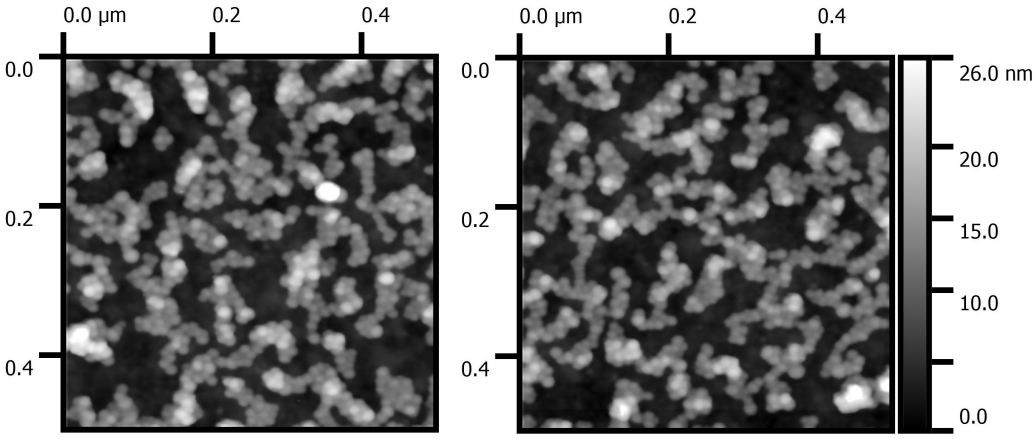

Figure 2.14: High quality AFM images of batch 1, samples C (see chapter 2.3.3) measured immediately before the control images shown in figure 2.13. The right image was ultimately used as substrate in the simulations of batch 1 (in chapter 4.2 and 4.3)

The same procedure was applied to the samples A from batch 2 (see chapter 2.3.3). The results are summarized in figure 2.15 showing again the control AFM image, the SEM image and two of the high-quality AFM images, with the right one used in the simulations.

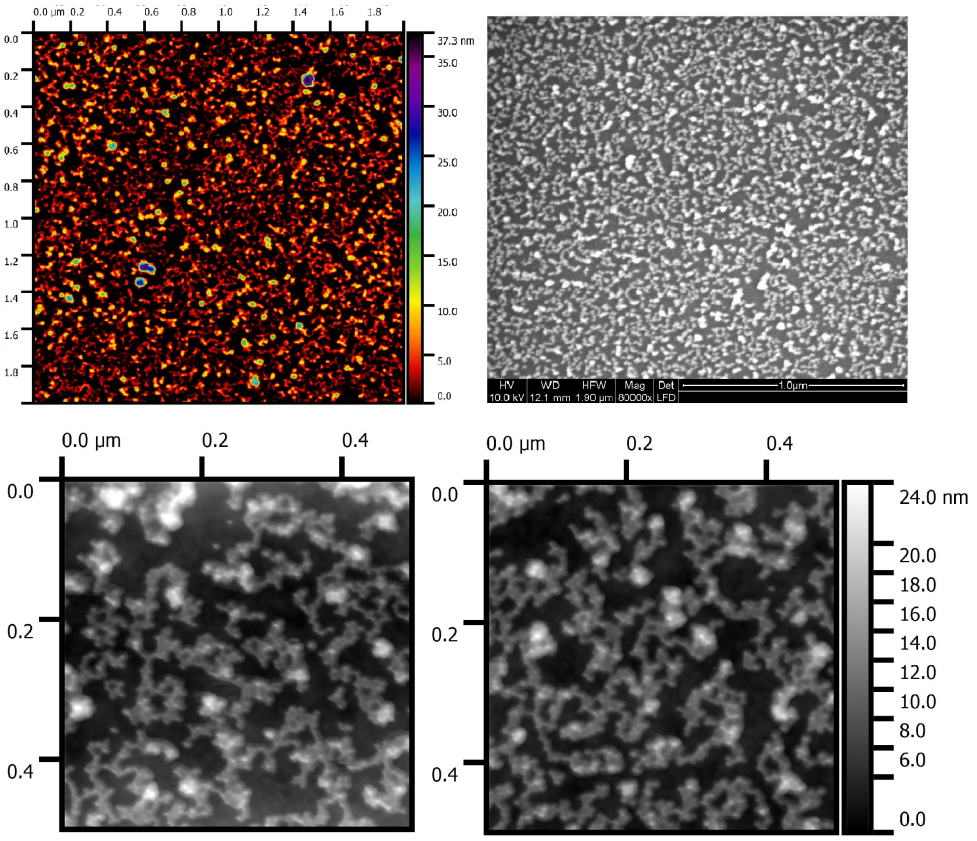

Figure 2.15: AFM images from batch 2, sample A (see chapter 2.3.3). Top left: AFM control image; Top right: SEM image for comparison; bottom left: AFM image of a 500x500 nm area; bottom right: AFM image used in the simulations in chapter 4.2 and 4.3

In addition to providing the crucial geometry input for the simulations, the AFM images were also used to determine the ratio between the surface area and the projected area (A, see chapter 2.3) necessary for the calculation of the enhancement factors. This can trivially be done with preprogrammed routines in Gwyddion, and it was found to be between 1.1-1.2 in all of the 500x500 nm sized images, and thus it was chosen as 1.15 for the calculation of the enhancement factors.

2.3 Measurement of the SERS enhancement factors

Both the theoretical basis and practical procedures for the measurement of SERS enhancement factors were established in a series of papers by Le Ru, Etchegoin et al. [13–15, 29], culminating in a book that summarizes their work [32]. The study of these works is highly recommended to the reader with deeper interest in the theoretical background of SERS and SERS enhancement factors. For the measurement of the SERS enhancement factors in this work the procedure outline in [29] is used. For the comparison between the results from the simulations and the measurements the SERS substrate enhancement factor, which is also the most widely used enhancement factor, has to be used. This enhancement factor measures the average enhancement of the signal of a single molecule at the substrate surface and is defined as in equation 2.1:

$$EF = \frac{I_{SERS}/N_{SERS}}{I_{Ref}/N_{Ref}} \tag{2.1}$$

with I_{SERS} the intensity of the SERS signal, I_{Ref} the intensity of the reference measurements, N_{SERS} the total number of molecules contributing to the SERS signal and N_{Ref} the total number of molecules contributing to the reference measurements.
This equation can be rewritten in terms of more accessible parameters as shown below (eq. 2.2-2.5).

$$N_{SERS} = \mu_S \cdot A \cdot A_{Spot} \tag{2.2}$$

$$N_{Ref} = c_{Ref} \cdot V_{eff} = c_{Ref} \cdot A_{Spot} \cdot H_{eff} \tag{2.3}$$

$$H_{eff} = \frac{V_{eff}}{A_{Spot}} \tag{2.4}$$

$$EF = \frac{I_{SERS} \cdot c_{Ref} \cdot H_{eff}}{I_{Ref} \cdot \mu_S \cdot A} \tag{2.5}$$

with μ_S the surface density of the molecule, A the ratio between the surface area of the nanostructure and the projected area, A_{spot} the size of the

laser spot in the focal plane, c_{Ref} the concentration of the reference solution, V_{eff} the effective scattering volume in the reference solution and H_{eff} the effective height of the scattering volume as defined by eq. 2.6.
Eq. 2.5 contains 6 parameters that need to be determined. Thereof the concentration of the reference solution is known ($c_{Ref} = 0.5M$), the surface density of 4-MBT is taken from the literature ($\mu_S = 5.3nm^{-2}$, [33]) and the ratio between the surface area and the projected area is determined from the AFM measurements ($A = 1.15$, see chapter 2.2). Thus, three parameters are left that need to be measured: the effective height of the scattering volume ($H_{eff} = 174\mu m$), which is an instrument dependent parameter with its measurement described in chapter 2.3.1, the intensities of the Raman signal from the reference solution (I_{Ref} see chapter 2.3.2) and the intensity of the SERS signal (I_{SERS} see chapter 2.3.3).
Additionally, the depolarization ratios both in solution and on the SERS substrate were measured (see chapter 2.3.4), as they provide an additional and unarguably superior way of checking the reliability of the computer simulations (see chapter 3.4) as well as the information about the symmetries of the Raman tensors involved.
This chapter deals only with the details of the measurements, whereas the summary of all the measurement results is provided in chapter 4.1.

2.3.1 Determination of the effective scattering height

The measurement of the effective scattering height was performed as detailed in the supporting information of [29]. A Si-wafer was scanned from well out off focus through the focal plane to well out off focus again and the Intensity of the 520 cm^{-1} band of Si was measured. Figure 2.16 shows an example of one such measurement. It is crucial that the parameters for the pinhole setting, slit setting, objective and laser wavelength are exactly the same as those used for the measurements of I_{Ref} and I_{SERS}. Thus for all measurements of H_{eff} a slit size of 300 µm, a pinhole size of 200 µm, a laser wavelength of 633 nm (16 mW) and an x10 objective (NA 0.25) were used. The integration time was 0.5 seconds (x2 accumulations).

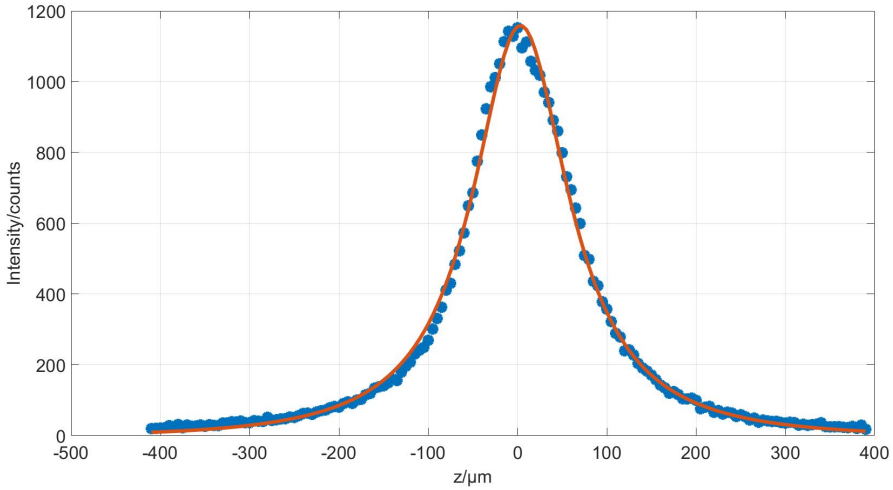

Figure 2.16: Example of a measurement of H_{eff} by scanning a Si-wafer through the focus. The blue asterisks are the measured intensities of the 520 cm^{-1} band and the red line is a Gauss-Lorentz fit approximating the measured data

From the results of this measurement H_{eff} can be calculated by equation 2.6 [29]. The integral in equation 2.6 can either be evaluated using the Gauss-Lorentz fit approximating the data or it can be calculated numerically from the measurement data directly as indicated. Both ways of calculating Heff produced consistent results and the fit-based integral was used for the data in table 2.2:

$$H_{eff} = \int_{-\infty}^{\infty} \frac{I(z)}{I_0} dz \approx \sum_{z_{min}}^{z_{max}} \frac{I(z)}{I_{max}} \cdot \Delta z \tag{2.6}$$

with $I(z)$ the intensity as a function of z, I_0 the intensity in the focal plane, I_{max} the maximum intensity measured, Δz the step size in the z-direction and z_{max} (z_{min}) the highest (lowest) z-position.
A subtle aspect of the measurement of H_{eff} is the refraction at the air/solution interface. This refraction might influence the results, especially since no immersion objective was used and the reference measurements were carried out in several different solutions. Therefore, measurements in five media with increasing refractive index (3 measurements per media) were performed. The respective media were air (n = 1), water (n = 1.33), ethanol

(n = 1.36, reference solution), isopropanol (n= 1.38, reference solution) and dimethylsulfoxid (n = 1.48). The results of these measurements are summarized in table 2.2.

Table 2.2: Results of the measurements of H_{eff} in five different media

Media	1. $H_{eff}/\mu m$	2. $H_{eff}/\mu m$	3. $H_{eff}/\mu m$	$\langle H_{eff} \rangle \pm \sigma(H_{eff})/\mu m$
Air (n=1)	173	170	171	171 ± 2
Water (n = 1.33)	173	177	176	175 ± 2
Ethanol (n = 1.36)	178	179	178	178 ± 1
Isopropanol (n= 1.38)	179	178	176	178 ± 2
Dimethylsulfoxid (n = 1.48)	168	169	166	168 ± 2

Since the overall influence of the refractive index appears to be rather small, the average of all measurements in table 2.2 (with the corresponding standard deviation) was used as the value of H_{eff}.

$$H_{eff} = 174 \pm 4\mu m$$

2.3.2 Reference measurements

The reference measurement is a fairly straightforward procedure, if a suitable reference solvent is available. The requirements for a good reference solvent are that the molecule can be dissolved in a reasonably high concentration, and that the Raman bands of the molecule can be measured without interference from the Raman bands of the solvent. For the molecule 4-MBT ethanol turned out to be a near perfect reference solvent as is demonstrated by the spectra of solid 4-MBT, pure ethanol and a 0.5 M solution of 4-MBT in ethanol in figure 2.17. The spectra were measured using a slit size of 300 µm, a pinhole size of 200 µm, a laser wavelength of 633 nm (16 mW) and an x10 objective (NA 0.25). The integration time was 1 second (x64 accumulations) and the laser was focused deep enough into the solution to get the maximum intensity of the Raman bands. Additionally, the spectra in figure 2.17 were normalized to clearly show the interference between the bands of ethanol and 4-MBT.

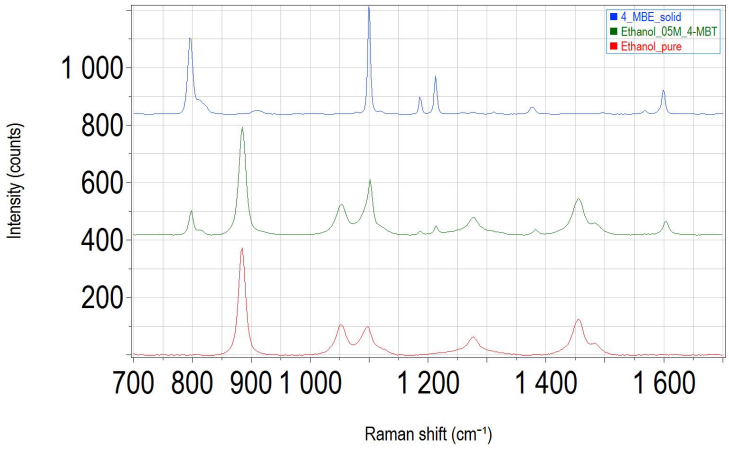

Figure 2.17: Comparison between the spectra of solid 4-MBT, a 0.5 M solution of 4-MBT in ethanol and pure ethanol

In the spectral region between 700 cm^{-1} and 1700 cm^{-1} that was later used for the determination of the enhancement factors, all bands of 4-MBT except the one at 1100 cm^{-1} can be measured in ethanol without interference from any ethanol bands. Next Isopropanol was tried as a reference solvent, and it was possible to extract the intensity of the 1100 cm^{-1} band from a peak fit of the band triplet between 1100-1200 cm^{-1}. The spectra are shown in figure 2.18 (all normalized), and the same measuring parameters were used as those for the measurement in ethanol.

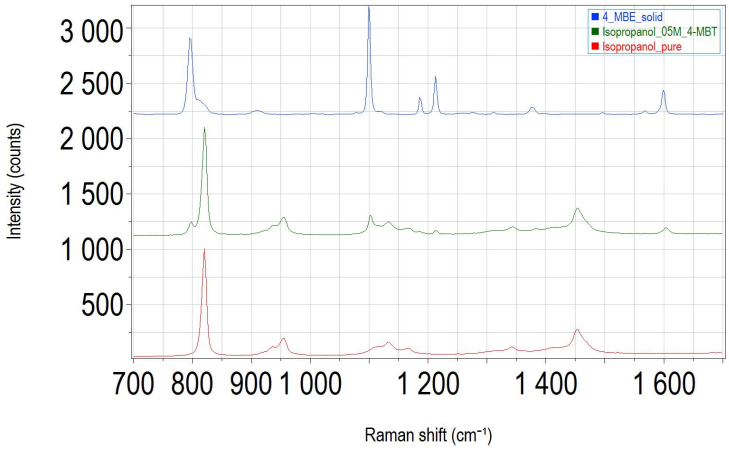

Figure 2.18: Comparison between the spectra of solid 4-MBT, a 0.5 M solution of 4-MBT in isopropanol and pure isopropanol

The combination of measurements in both isopropanol and ethanol is sufficient to determine all the band intensities for 4 MBT, but the reference measurements have always to be performed in addition to the measurements of the SERS intensities. Therefore the limitation to only one solvent would be highly desirable, as this both eliminates sources of errors (two solutions could have slightly different concentrations for instance) and makes the preparation for the EH measurements less laborious. Luckily, the relative band intensities of the molecule in solution are fixed. Thus, under the assumption that the intensity ratio between the bands is known, the intensity of the 1100 cm^{-1} band can be extracted from the measurement in ethanol by use of its relative intensity to another band of 4-MBT. From the measurement in isopropanol the intensity of the 1100 cm^{-1} band was determined to be 2.33 times the intensity of the band at 1598 cm^{-1}. This ratio was confirmed by an additional measurement of a 1 M solution of 4-MBT in acetone (figure 2.19, all spectra normalized). The measurement in acetone was again performed applying the same parameters as for the measurements in ethanol and isopropanol.

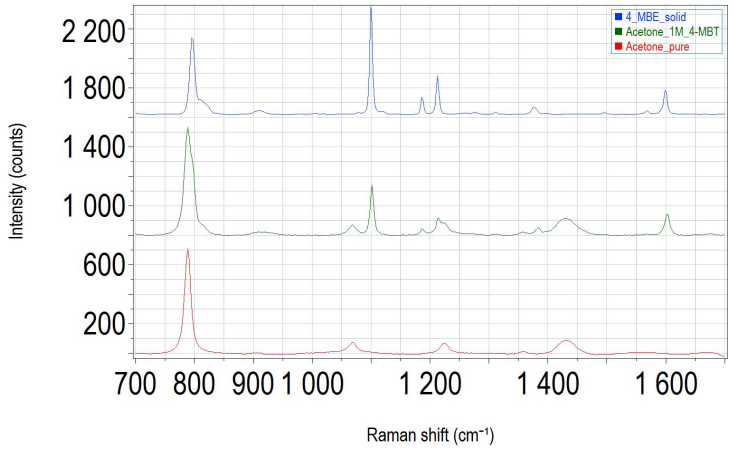

Figure 2.19: Comparison between the spectra of solid 4-MBT, a 1 M solution of 4-MBT in acetone and pure acetone

To sum up, a reference measurement of a 0.5 M solution of 4-MBT in ethanol is sufficient to determine all the band intensities, with the intensity of the 1100 cm^{-1} band being fixed as 2.33 times the intensity of the 1598 cm^{-1} band. The reference measurement has to be performed alongside the measurement of the SERS intensities. It is carried out by focusing the laser so deep (approximately a couple of 100 µm below the surface) into the solution that the signal from the solution is saturated. Additionally

the reference measurement has to be performed with the same parameters as the SERS measurement, with the possible exception of using more accumulations. As standard parameters a slit size of 300 µm, a pinhole size of 200 µm, a laser wavelength of 633 nm (4 mW) and an x10 objective (NA 0.25) were chosen.

2.3.3 SERS intensity measurements

Given the results of chapter 2.1, which show that the reproducibility within one batch is approximately consistent with the reproducibility across a single substrate, whereas batches differ due to variations in the mean film thickness and roughness, thus the average spectra of a batch was used for the determination of the SERS intensities. Two batches of 8 samples each were manufactured as detailed in chapter 2.1. A Raman spectrum of each sample was measured, and the average spectra of the samples of one batch were used to determine the SERS enhancement factors in chapter 4.1. The standard deviation between the samples of the same batch is used for the error estimates in chapter 4.3. Note that for the computer simulations the AFM image of a substrate, which provided a spectrum close to the average spectrum of the batch, was used.
The SERS measurements were performed in a straightforward manner by simply focusing on the substrate surface (in air). The integration time was 1 second (x16 accumulations). The spectra of batch 1 are represented in figure 2.20.

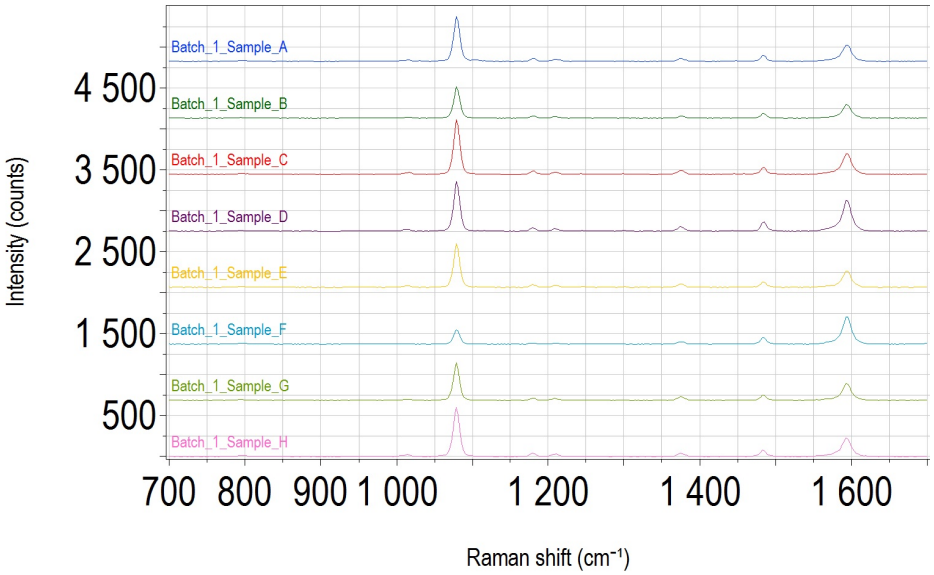

Figure 2.20: SERS spectra measured form the 8 samples of batch 1

Note that the spectrum of batch 1, sample F differs significantly from the other spectra. This sample was dropped once during the manufacturing process and thus excluded from the averaging. The AFM images of batch 1, sample C were used for the simulations (see chapter 4.2 and 4.3). The spectra of batch 2 are represented in figure 2.21.

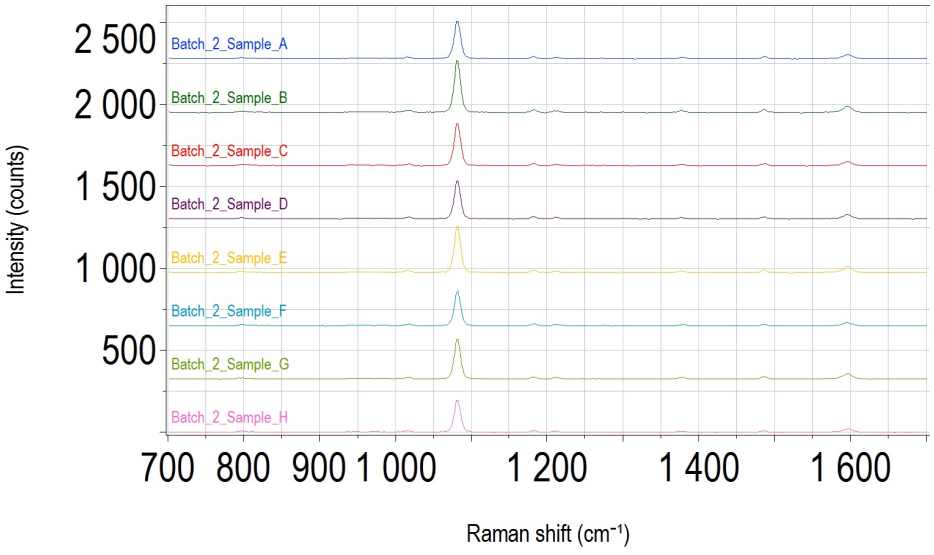

Figure 2.21: SERS spectra measured from the 8 samples of batch 2

The AFM images of batch 2, sample A were also used for the simulations (see chapter 4.2 and 4.3). Note that the resulting enhancement factors of batch 1 and 2 are summarized in chapter 4.1 and 4.3.

2.3.4 Depolarization ratios

Depolarization ratios were measured both on the SERS substrates and in solution. The depolarization ratios in solution are crucial as they contain information about the symmetry of the Raman tensor [32]. Furthermore, as explained in chapter 3.4, using Raman bands with a depolarization ratio close to 0 in solution is highly desirable for the comparison of the measurements to the simulations.
The depolarization ratios from the SERS substrates are a very interesting quantity for the comparison of the measurements and simulations as well. As outlined in chapter 3.4, using the depolarization ratios rather than the enhancement factors eliminates the requirement of a small difference in Raman shift between the SERS and reference measurements (no chemical enhancement). Thus a comparison of the calculated depolarization ratios to the measured ones is possible for more bands than for the enhancement factors. Additionally, depolarization ratios can be measured much more reliably than enhancement factors. The depolarization ratios are simply the ratio of two spectra recorded at the same position with a different polarizer setting. This eliminates the need for a reference measurement as well as all the other parameters (A, H_{eff}, μ_S, c_{ref}) necessary for the calculation of the enhancement factors. Furthermore, variations in the quality of the monolayer are less significant for the measurement, as the ratio of two spectra from the same monolayer is taken. Thus, depolarization ratios can be more reliably measured and are theoretically easier to predicted by simulation.
The depolarization ratio is the ratio between Raman spectra with a perpendicular and parallel polarization relative to the laser beam. Since our spectrometer (see instrumentation) cannot measure spectra with a defined polarization by default, an improvised setup had to be used. The polarization filter from another microscope was inserted in front of the slit of the spectrometer as shown in figure 2.22. Luckily, the orientation of the laser at the entrance slit is known (up down), thus by turning the inserted filter accordingly spectra with a defined polarization relative to the laser beam can be measured.

Figure 2.22: Improvised setup for the measurement of Raman spectra with a polarized beam. A polarization filter is placed in front of the entrance slit of the spectrometer

The polarization dependent Raman spectra in solution were measured using both ethanol and isopropanol (c = 0.5 M) as a reference solvent. The results are shown in figure 2.23. The integration time was 8 seconds (x8 accumulations).

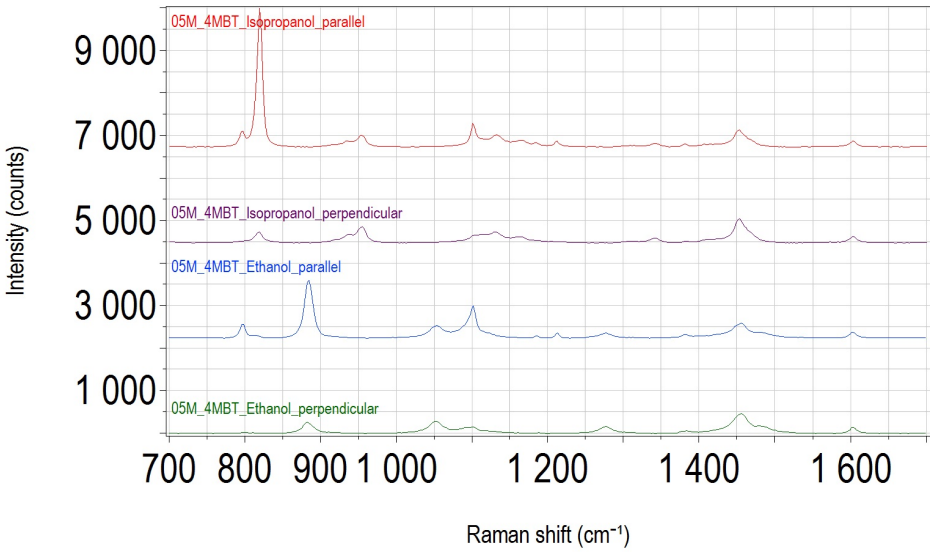

Figure 2.23: Raman spectra of 4-MBT measured in a 0.5 M solution in both ethanol and isopropanol measured with polarized laser beams.

For the measurement of the polarized SERS spectra two samples with spectra close to the average spectra from each batch (see chapter 2.3.3) were chosen. The samples used were batch 1, sample C, batch 1, sample G, batch 2, sample A and batch 2, sample C. For each sample a mapping of an area of 200x200 µm (5x5 pixel) was performed, and the average spectra from this measurements were taken. The integration time was 16 seconds (x2 accumulations). The resulting SERS spectra are show in figure 2.24.

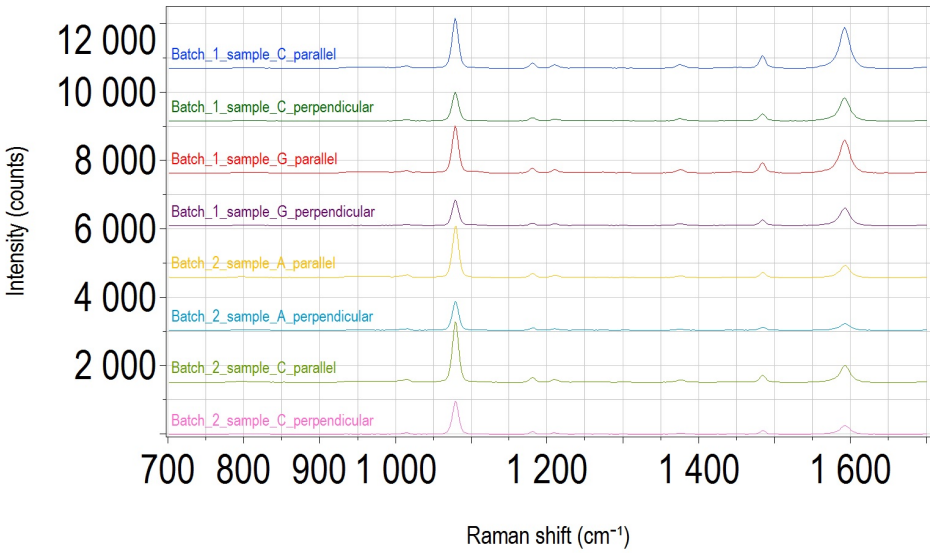

Figure 2.24: SERS spectra of batch 1, sample C, batch 1, sample G, batch 2, sample A and batch 2, sample C measured with polarized laser beams.

The resulting depolarization ratios of batch 1 and 2 are summarized in chapter 4.1 and 4.3.

2.4 Summary

In this chapter the necessary experimental steps to achieve the results in chapter 4 were discussed. These involved manufacturing the SERS substrates, depositing a suitable SAM at the substrate, characterizing the substrates with two complementary microscopic technique and finally measuring the enhancement factors and depolarization ratios.
Everything starts with the substrate manufacturing process, where first glass slides were sputtered with Au and subsequently annealed to produces Au nanoisland films. This process was optimized with regard to a good reproducibility. Methylene Blue and RohdaminB, spin coated as thin films on the substrate, were used as probe molecules. Because of the relatively large roughness of the glass slides, which posed a problem for the AFM measurements, the glass slides were finally replaced by Si wafers. This necessitated a more elaborate cleaning procedure, as only Si wafers with a rather high surface contamination were available. Additionally, because of their high fluorescence, Methylene Blue and RohdaminB had to be replaced for the measurement of the reference spectra (and also enhancement factors). 4-methlybenzenzthiol (4-MBT) was chosen, as it forms a SAM on Au, its absorption behavior on Au is thoroughly investigated [39, 40] (including its behavior with regard to chemical enhancement on Au [41]), and it has also been the probe molecule in previous studies comparing DDA simulations to measured enhancement factors [30]. The procedure for the deposition of the 4-MBT SAM was optimized. In the final procedure at first the substrate is immersed in a 10^{-4} M solution of 4-MBT in water for 1 h and subsequently dipped for a couple of seconds into pure ethanol, followed by a careful drying the substrate using a CO_2 spray.
With the substrate manufacturing process established, the microscopic characterization of the substrates was carried out primarily by AFM, with SEM serving as a secondary microscopic technique to assess the influence of tip convolution. Using this combination, best practice guidelines regarding the tip were established. By use of a SEM image in order to assess the quality of the AFM measurements, these guidelines basically boil down to the requirements that always a fresh tip has to be used and, due to rather quick tip degradation, only a limited number of images should be measured with the same tip. With these guidelines high quality AFM mappings of substrates suitable for the implementation in the computer simulations were accomplished, and the ratio between the surface area of the nanoislands and the projected area, which is an important parameter for the measurement of SERS enhancement factors, could be measured.
Finally, the measurement of SERS enhancement factors was carried out, us-

ing the procedure outlined by Le Ru et al. [29], and with the single steps discussed in chapter 2.3. In addition to the Raman intensities of the SERS substrate and the reference, several other key parameters are necessary for the determination of SERS enhancement factors. The ratio between the surface area of the nanostructure and the corresponding projected area was determined from the AFM measurements. The surface density of 4-MBT was taken from the literature [33], and the effective height of the scattering volume was measured in several media with varying refractive indices, but no significant dependence on the refractive index could be found. A procedure was established, that besides the SERS measurements requires only one reference measurement of a 0.5 M solution of 4-MBT in ethanol. To this aim the relative intensity of the only band of 4-MBT, that is masked by the bands of ethanol (1100 cm^{-1}), to another band of 4-MBT in solutions of isopropanol and acetone was measured. The SERS intensities were measured as per batch average (of 2 batches of 8 samples each), due to the variations in the average thickness of the Au films between the batches. Last but not least, the depolarization ratios of 4-MBT (see chapter 4.1) were measured using an improvised setup described in chapter 2.3.4. Polarization dependent Raman spectra of 0.5 M solutions of 4-MBT in ethanol and isopropanol as well as at 4 SERS substrates (2 from each batch) were recorded.

Chapter 3

Near-Field simulations & calculation of SERS-EF

After the discussion of both the substrate manufacture and the measurement of the SERS total enhancement factors in chapter 2, this chapter focuses on the theoretical aspects of SERS enhancement factors, especially the electromagnetic enhancement factors. An introduction to the main points and challenges for calculating electric nearfields is given, followed by a detailed account of the specific computational method used in this work, the discrete dipole approximation (DDA). Additionally, the DDA-script developed in this work is presented, especially all computational parameters are discussed, and a variety of test simulations are used to verify the correctness of the script, justify the parameter choices and provide an error estimate. Finally, the theoretical connection between the calculated fields and the measured enhancement factors is discussed with a focus on the limitations of the predictability of the enhancement factors when compared to measured enhancement factors.

The first important point that needs to be addressed is that the real (measured) SERS-enhancement can be split into three contributions – electromagnetic enhancement, chemical enhancement and surface selection rules (or orientation effects). The dominant factor of these three is the electromagnetic enhancement, which is also the only enhancement factor that is (mostly) independent of the probe molecule. Whereas chemical enhancement refers to the change of the Raman tensor of the probe molecule when it adsorbs on the surface of the substrate. Therefore, it is not only molecule specific but also Raman band specific. Additionally, chemical enhancement can only be derived from quantum mechanical calculations. Surface selection rules refer to effects that arise due to a combination of the symmetry of the Raman tensor (which is band specific) and preferred

orientations of the molecule on the surface relative to the nearfields. Surface selection rules are very difficult to deal with in cases were the Raman tensor is non-isotropic, requiring detailed knowledge of the Raman tensor of the adsorbed molecules (quantum mechanics) and the adsorption geometry of the molecule. The discussion in this work is therefore often restricted to the isotropic cases. Luckily, chemical enhancement and surface selection rules combined usually play only a minor role compared to electromagnetic enhancement (on the order of approximately 0.1-10). Furthermore, difficulties resulting from the surface selection rules can be avoided by choosing bands with isotropic tensors. Since the focus of this work is large scale (classical by limit of computational power) calculation of the nearfields on the substrate, chemical enhancement and surface selection rules will not be included in the calculations and only discussed as a limitation of the accuracy of the predicted enhancement factors, which in in this work are always electromagnetic enhancement factors.

Electromagnetic enhancement is caused by the enhancement of the electric field of the excitation laser in the nearfield of nanostructures, as well as the nanostructure acting as an antenna for the emission of the Raman signal of the molecules. Since intensity scales with E^2 and the enhancement is the product of the excitation and the emission, the overall enhancement of the Raman signal scales with E^4. Thus, it is this 4^{th}-power relation that is responsible for the extremely high enhancements happening in SERS. Because the electromagnetic enhancement is essentially a combination of two field enhancement effects at the surface of nanostructures, the calculation of the electric nearfields is the key for the prediction of the SERS enhancement factors.

To calculate the electric nearfields it is necessary to solve the equations of electromagnetic scattering problem, which for general geometries can only be solved numerically. Usually this is done by discretization of either the differential or integral equation for the electric field resulting from Maxwell's equations for the electromagnetic scattering problem. The most common methods are the finite difference time domain method (FDTD), the finite element method (FEM), the discrete dipole approximation (DDA) and the boundary element method (BEM). The aim of this dissertation is to calculate the electric fields for an as exact representation of the real geometry of the substrate structures as possible. The main requirement for any method is therefore a very fine discretization of large areas of the substrates. In general methods based on the integral equations (DDA, BEM) are better suited for large numbers of discretization steps, as both FEM and FDTD require a discretization domain larger than the scattering particle. Additionally, the computing time and memory requirements of the DDA (in

the FFT-accelerated variant) and the BEM scale in case of a decrease of the step size better than FDTD and FEM. Furthermore, with regard to the total number of discretization steps the (FFT-accelerated) DDAs computing time and memory requirements scale significantly better than BEMs. Though, the BEM has the advantage that only the surface of the scatterer has to be discretized, which means that a smaller number of discretization steps is required than in the volume based DDA. However, this advantage is largely nullified for the substrates studied in this thesis (and for many other SERS substrates), because of the high surface to volume ratio of the nanostructures, making the DDA the best choice concerning discretization. The DDA also has the advantage of a straightforward discretization process, simplifying implementation of all required physical inputs (geometry, dielectric functions and incident electric fields). Additionally, the DDA offers some specific advantages for the calculation of SERS substrates, which may be relevant to further research. For example is it possible to include periodic structures analytically in the framework of the DDA, which could be very interesting for the investigation of highly ordered SERS substrates (like those produced by lithography or self-assembled polystyrene spheres). Moreover, in the DDA it is possible to include additional dielectric layers at the surface of the scatterer at little computational cost. This could be used to include the dielectric influence of the probe molecule or even rudimentary quantum mechanical models of the variation of the dielectric constant close to the surface.
However, before a DDA algorithm can be implemented and used to calculate electric nearfields a couple of things needs to be carefully considered, such as the inclusion of the Si-substrate in the simulation, the solution of the system of equations resulting from the discretization and, most importantly, the determination of the polarizabilities from the dielectric constants. This will be the starting points for our discussion of the fundamentals of the discrete dipole approximation.

3.1 Fundamentals of the discrete dipole approximation (DDA)

This chapter discusses the theoretical aspects of the DDA script that was developed for the calculation of the enhancement factors in this thesis, whereas the practical aspects of the implementation are summarized in chapter 3.2 and appendix A.3. The discussion starts with the fundamental equations, which are directly derived from Maxwell's equations, and goes through all the necessary simplifications and their implications to the script. Where necessary, the reader will be pointed to the subchapter in chapter 3.2 (and appendix A.3) that deals with the implementation of a specific theoretical step. For the best overall understanding of the DDA script I recommend reading this chapter once without interruption and then reading it a second time stopping at every reference to chapter 3.2 (appendix A.3) to read the corresponding subchapter there. A good review of the DDA was written by Yurkin and Hoekstra [51] and an interesting review of the electromagnetic scattering problem in general is provided by Kahnert [52]. Both reviews are recommended to the interested reader.

3.1.1 Deriving the fundamental equation of the DDA

The DDA was first developed by [53] based on phenomenological arguments and later refined and converted into a publicly available computer code by [54–56]. It was thoroughly derived from Maxwell's equations by [57], which opened the possibility for a further refinement of the DDA [58–62]. The fact that the exact deviation was done only after the first version of DDA had been developed is also the reason why two mathematically equivalent versions of the fundamental equation of the DDA exist. The "experimentalists" approach (eq. 3.1) expresses the equations in terms of polarization, which is the one used in the script presented in this work. Whereas, the "theorists" approach (eq. 3.2) expresses the equations in terms of excitation fields.

$$\vec{E}_i^{inc} = \bar{\bar{\alpha}}_i^{-1} \cdot \vec{P}_i - \sum_{i \neq j} \bar{\bar{G}}_{ij} \cdot \vec{P}_j \tag{3.1}$$

$$\vec{E}_i^{inc} = \vec{E}_i^{exc} - \sum_{i \neq j} \bar{\bar{G}}_{ij} \cdot \bar{\bar{\alpha}}_j \cdot \vec{E}_j^{exc} \tag{3.2}$$

$$\vec{P}_i = \bar{\bar{\alpha}}_i \cdot \vec{E}_i^{exc} = V_i \cdot \chi_i \cdot \vec{E}_i \tag{3.3}$$

$$\chi_i = \frac{\epsilon_i - 1}{4\pi} \tag{3.4}$$

with $\vec{E}^{inc}$ the incident electric field, $\vec{E}^{exc}$ the excitation electric field, $\vec{E}$ the total electric field, $\vec{P}$ the polarization, $\bar{\bar{\alpha}}$ the polarizability tensor, $\bar{\bar{G}}$ the Green tensor, χ is the susceptibility of the scatterer, ϵ is the dielectric constant of the scatterer and V is the volume of a single discretization unit. The indices i and j denote the position on the discretization grid (for example $\vec{E}_i = \vec{E}(\vec{r}_i)$).
In both cases the polarizability appears as a variable and the main difference between various versions of the DDA is how the polarizability is determined from the dielectric constants of the involved materials. The original DDA depicts the scatterer as an array of dipoles and uses the Clausius-Mossotti polarizability [53], but the polarizability was later refined by several corrections, such as the radiative reaction (RR) [54, 63] or the lattice dispersion relation (LDR) [55]. The LDR has also been implemented in our script for test purposes but was not used in the simulations presented in this work. It is therefore stated explicitly here.

$$\bar{\bar{\alpha}}^{LDR} = \bar{\bar{I}} \cdot \frac{\alpha^{CM}}{1 + \alpha^{CM}/d^3 \cdot [b_1 + m^2 \cdot b_2 + m^2 \cdot b_3 \cdot S] \cdot (k_0 \cdot d)^2} \tag{3.5}$$

$$\alpha^{CM} = \frac{3d^3}{4\pi} \cdot (\frac{m^2 - 1}{m^2 + 1}) \tag{3.6}$$

$$S = \sum_i (a_i \cdot e_i)^2 \tag{3.7}$$

with $\bar{\bar{I}}$ the identity tensor, d the discretization step size, m the refractive index of the scatterer, a_i the components of the propagation vector of the incident field, e_i the components of the polarization vector of the incident field, $b_1 = -1.8915316$, $b_2 = 0.1648469$ and $b_3 = -1.7700004$.

Further improvements became possible only after the rigorous derivation of the DDA, which gives the connection between the polarizability (α),

the dielectric constant (ϵ) and the self-term of the Green's tensor ($\bar{\bar{G}}_{ij}$). The main two versions of the DDA based on this connection are the filtered coupled-dipoles (FCD) approach [60] and the integrated tensor (IT) approach [61]. The respective improved polarizabilities are of particular importance for high refractive index materials [60, 61] like those used in this work. Therefore, a variant of the IT approach is used in our DDA script, and the deviation of the equations 3.1, 3.2 and the IT approach will now be briefly discussed, following mostly the arguments given by [61].
We start the discussion with equation 3.8, which is the fundamental volume integration equation for the electric fields for the electromagnetic scattering problem that can be derived directly (and without simplifications) from Maxwell's equations [52].

$$\vec{E}(\vec{r}) = \vec{E}^{inc}(\vec{r}) + \int_{V_S} \bar{\bar{G}}(\vec{r}, \tilde{\vec{r}}) \cdot \chi(\tilde{\vec{r}}) \cdot \vec{E}(\tilde{\vec{r}}) d\tilde{\vec{r}} \tag{3.8}$$

with $\vec{E}(\vec{r})$ the total electric field, $\vec{E}^{inc}(\vec{r})$ the incident electric filed, $\bar{\bar{G}}(\vec{r}, \tilde{\vec{r}})$ the Green's function in the background medium, $\chi(\tilde{\vec{r}})$ the susceptibility of the scatterer, V_S the volume of the scatterer and $\vec{r}$ the position vector.
In order to solve equation 3.8 for arbitrary volumes (arbitrary geometries) it is necessary to discretize the electric field. The aim of this is to convert the integral of the electric field in equation 3.8 into a sum, which will ultimately make it possible to write equation 3.8 as a solvable system of linear equations for the unknown electric fields. This is done by assuming that the electric field is constant in small volumes (denoted as V_J in equation 3.9). Additionally, it is assumed that the dielectric function (ϵ) is constant in that small volumes. An assumption that is nearly always made [51] and always justified for sufficiently small volumes. These two assumptions immediately lead to equation 3.9.

$$\vec{E}_i = \vec{E}_i^{inc} + \sum_{j=1}^{N} \int_{V_J} \bar{\bar{G}}(\vec{r}_i, \tilde{\vec{r}}) d\tilde{\vec{r}} \cdot \chi_j \cdot \vec{E}_j \tag{3.9}$$

with V_j the discretization volume centered at $\vec{r}_j$, N the total number of discretization units and $\vec{E}_i = \vec{E}(\vec{r}_i)$ as given in equation x-z.
In principle equation 3.9 could already be used to calculate the electric fields, however there is a subtle mathematical problem hidden in it. The

Green's function has a singularity at $(r = \tilde{r})$, which occurs in the sum at the self-term $(j = i)$. This singularity plays a key role in the DDA, as it is closely connected to the polarizability term. Rewriting eq.3.9 in a way similar to eqs 3.1 and 3.2 will make this obvious. This is done by bringing all the unknown fields on one side and removing the singular self-term from the sum and instead writing it explicitly.

$$\vec{E}_i^{inc} = \left(\bar{\bar{I}} - \int_{V_i} \bar{\bar{G}}(\vec{r}_i, \widetilde{\vec{r}}) d\widetilde{\vec{r}} \cdot \chi_i\right) \cdot \vec{E}_i - \sum_{j=1; j\neq i}^{N} \int_{V_j} \bar{\bar{G}}(\vec{r}_j, \widetilde{\vec{r}}) d\widetilde{\vec{r}} \cdot \chi_j \cdot \vec{E}_j \quad (3.10)$$

We can now define the polarizability in terms of the dielectric constant and the self-term of the Green's tensor. Additionally, using eq. 3.3 we get an equation that is almost identical to the original DDA equation (Eq.3.12).

$$\bar{\bar{\alpha}}_i := \bar{\bar{I}} \cdot \frac{V_i \cdot \chi_i}{1 - \int_{V_i} \bar{\bar{G}}(\vec{r}_i, \widetilde{\vec{r}}) d\widetilde{\vec{r}}} \quad (3.11)$$

$$\vec{E}_i^{inc} = \bar{\bar{\alpha}}_i^{-1} \cdot \vec{P}_i - \sum_{j=1; j\neq i}^{N} \frac{\int_{V_j} \bar{\bar{G}}(\vec{r}_i, \widetilde{\vec{r}}) d\widetilde{\vec{r}}}{V_j} \cdot \vec{P}_j \quad (3.12)$$

The last assumption necessary to get back to eq.3.1 is to assume that the Green's function is constant over a discretization volume (for the none self-terms; eq. 3.13). Alternatively the Green's tensor (in eq. 3.1) can be defined in terms of the integral over the Green's function in eq. 3.12 (eq. 3.14).

$$\bar{\bar{G}}(\vec{r}_i, \widetilde{\vec{r}}) \approx const. in V_j => \frac{\int_{V_j} \bar{\bar{G}}(\vec{r}_i, \widetilde{\vec{r}}) d\widetilde{\vec{r}}}{V_j} = \bar{\bar{G}}(\vec{r}_i, \vec{r}_j) = \bar{\bar{G}}_{ij} \quad (3.13)$$

$$\bar{\bar{G}}_{ij} := \frac{\int_{V_j} \bar{\bar{G}}(\vec{r}_i, \widetilde{\vec{r}}) d\widetilde{\vec{r}}}{V_j} \quad (3.14)$$

Note that some of the assumptions made in the original DDA (eq. 3.5 and eq. 3.13) such as a constant Green's function in the discretization volume or a specific form of the polarizability are not necessary, as these assumptions could be eliminated by evaluating the integrals in eq 3.11 and eq 3.14. This is the central idea of the IT approach that will be discussed in the next subsection.

3.1.2 The integrated tensor approach

The main idea of the IT approach has already been introduced. Equation 3.11 is used to calculate the polarizabilities and equation 3.14 to calculate the tensor elements. However, in equation 3.11 the issue of the singularity in the integral over the self-term has not yet been addressed. Luckily, Chaumet et al. [61] managed to express the self-term (by Weyl expansion) in a way that can be numerically integrated.

$$\int_{V_i} \bar{\bar{G}}(\vec{r}_i, \widetilde{\vec{r}}) d\widetilde{\vec{r}} = \frac{16}{\pi} \cdot \bar{\bar{I}} \cdot (Int_1 + Int_2) \tag{3.15}$$

$$Int_1 = \int_{w_0=0}^{k_0} \frac{-k_0^2 \cdot (1 - e^{iw_0 d/2}) - w_0^2 e^{iw_0 d/2}}{w_0} \cdot \left[\int_{\Theta=0}^{\pi/2} F(\Theta, w_0) d\Theta \right] dw_0 \tag{3.16}$$

$$F(\Theta, w_0) = \frac{\sin\left(\sqrt{k_0^2 - w_0^2}\cos(\Theta) d/2\right) \cdot \sin\left(\sqrt{k_0^2 - w_0^2}\sin(\Theta) d/2\right)}{|k_0^2 - w_0^2| \cdot \cos(\Theta) \cdot \sin(\Theta)} \tag{3.17}$$

$$Int_2 = \int_{\beta=0}^{\infty} \frac{k_0^2 - (k_0^2 + \beta^2) \cdot e^{-\beta d/2}}{\beta} \cdot \left[\int_{\Theta=0}^{\pi/2} G(\Theta, \beta) d\Theta \right] d\beta \tag{3.18}$$

$$G(\Theta, \beta) = \frac{\sin\left(\sqrt{k_0^2 - \beta_0^2}\cos(\Theta) d/2\right) \cdot \sin\left(\sqrt{k_0^2 - \beta_0^2}\sin(\Theta) d/2\right)}{|k_0^2 - \beta_0^2| \cdot \cos(\Theta) \cdot \sin(\Theta)} \tag{3.19}$$

with k_0 the modulus of the wave vector of the incident field and d the discretization step size.

Combining eq 3.13 with eq.3.15-3.19 the polarizabilities can easily be calculated (the source code for the calculation of the polarizability can be found in appendix A.3.8). While calculation of the polarizabilities directly from the Green's function is certainly the main point of the IT approach, the significance of using the integrated tensor elements rather than the approximation that the Green's function is constant over a discretization volume should not be overlooked. It has already been shown by Chaumet et al. [61] in the publication introducing the IT that integration of the whole tensor is a significant improvement over merely getting the polarizabilities by integration of only the diagonal elements. This intuitively makes sense because all terms in the Green's function scale with $1/(r_i - r_j)^n$, which means that the closest dipoles have the strongest interaction and that the approximation ($\bar{\bar{G}}(\vec{r_i}, \widetilde{\vec{r}}) \approx const.inV_j$) is least true for short distances. Integration of the full tensor is easy in theory (eq.3.14 can be solved numerically), but from a practical point of view numerically solving an integral for every element of the Green's tensor can become computationally expensive. When using the FFT accelerated version of the DDA (see subchapter 3.1.3) the number of integrals that need to be evaluated can be at the order of 10^8, which is certainly linked with long computing time and high cost. This problem is treated in the DDA implementation by evaluating the full integral only to a certain maximum distance (for a certain number of off diagonal elements) and using eq 3.13 otherwise. This is possible, because eq 3.14 converges to eq 3.13 for large distances between the dipoles. For the details of this implementation (and approximation) see chapter 3.2.1 and appendix A.3.11.

3.1.3 The fast Fourier transformation acceleration of the DDA

It has been noticed early on that, if the dipoles are arranged on a rectangular grid [23], the DDA can be greatly be accelerated using the fast Fourier transformation (FFT). This is possible due to the symmetry of the Green's tensor, enabling the rearrangement of the tensor into a multilevel block-Toeplitz matrix for dipoles on a rectangular grid. At this point the main idea behind the FFT accelerated DDA and its implications for the discretization grid, processing speed and memory requirements will be

discussed. The details of the implementation of the FFT-acceleration can be found in chapter 3.2.3 and appendix A.3.5, A.3.12 & A.3.13.
To understand the idea of the FFT accelerated DDA it is important to look at eq. 3.1 from a computational point of view. To this aim eq. 3.1, which actually represents a system of equations marked by the index i, is rewritten in eq. 3.20 in terms of vectors of fields, polarizations and polarizabilities and a matrix of Green's tensors.

$$\vec{\tilde{E}}^{inc} = \vec{\tilde{\alpha}} \cdot \vec{\tilde{P}} + \bar{\bar{A}} \cdot \vec{\tilde{P}} \tag{3.20}$$

$$with \qquad \vec{\tilde{E}}^{inc} = \begin{pmatrix} \vec{E}_i^{inc} \\ \vec{E}_j^{inc} \\ \vdots \end{pmatrix} \vec{\tilde{P}} = \begin{pmatrix} \vec{P}_i \\ \vec{P}_j \\ \vdots \end{pmatrix} \vec{\tilde{\alpha}} = \begin{pmatrix} \bar{\bar{\alpha}}_i \\ \bar{\bar{\alpha}}_i \\ \vdots \end{pmatrix} \bar{\bar{A}} = \begin{pmatrix} 0 & \bar{\bar{G}}_{ij} & \cdots \\ \bar{\bar{G}}_{ji} & 0 \cdots & \\ \vdots & \vdots & \ddots \end{pmatrix}$$

The linear system of equations in eq. 3.20 needs to be solved for the vector $\vec{\tilde{P}}$, which can be performed by both direct and iterative methods [51]. In most cases iterative methods will be more efficient for large numbers of dipoles. A variety of iterative algorithms is available such as conjugate gradient (CG), biconjugate gradient (Bi-CG), quasi-minimal residual (QMR) or generalized minimal residual (GMRES; used in this work). All of these have in common that for every iterative step the right hand side of eq. y has to be evaluated for one or several "test" vectors $\vec{\tilde{P}}$ (with the "test" vectors converging towards the solution). Therefore, the computationally most expensive step is the calculation of the product $\bar{\bar{A}} \cdot \vec{\tilde{P}}$ and the memory requirements are mainly predetermined from storage of the matrix $\bar{\bar{A}}$. The matrix $\bar{\bar{A}}$ contains the interaction term (Green's tensor) of every possible dipole combination, meaning that it has the size NxN (N being the total number of dioples). Therefore the memory requirement scales with O(N^2) and the processing time for one matrix-vector multiplication is also of O(N^2). It is now interesting to see what the matrix $\bar{\bar{A}}$ looks like on a rectangular grid.
On a rectangular grid the position of any dipole can be defined by its indices (in x, y and z) and the distance vector between two dipoles can be defined in terms of the difference of their indices (see eq. 3.21 & 3.22). It is important to note that all the elements of the Green's tensor are defined by the distance vector between the two interacting dipoles. Therefore, the Green's tensor elements can also be easily defined in terms of the difference

of indices between the interacting dipoles (eq.3.23).

$$\vec{r} = \begin{pmatrix} i_x - 1 \\ i_y - 1 \\ i_z - 1 \end{pmatrix} \cdot d \wedge \vec{i} := \begin{pmatrix} i_x \\ i_y \\ i_z \end{pmatrix} \tag{3.21}$$

$$\vec{r_{\vec{i}}} = (\vec{i} - 1) \cdot d \qquad \vec{r_{\vec{i}}} - \vec{r_{\vec{j}}} = (\vec{i} - \vec{j}) \cdot d \tag{3.22}$$

$$\bar{\bar{G}}(\vec{r_{\vec{i}}}, \vec{r_{\vec{j}}}) = \bar{\bar{G}}(\vec{r_{\vec{i}}} - \vec{r_{\vec{j}}}) = \bar{\bar{G}}(\vec{i} - \vec{j}) = \bar{\bar{G}}_{\vec{i}-\vec{j}} \tag{3.23}$$

It is now apparent that on a rectangular grid the matrix $\bar{\bar{A}}$ has many redundant elements, because many dipole pairs will have the same distance vector (see fig 3.1). In fact the total number of unique distance vectors follows from the total number of possible values of i-j. On a grid of size ix=1...nx, iy=1...ny and iz=1...nz there are 2nx-1 (-nx+1,...,0,...,nx-1) possible values for ix-jx and the same for the y- and z-coordinate (2ny-1; 2nz-1). This is a total of (2nx-1) x (2ny-1) x (2nz-1) $\approx$ 8xN unique values and accordingly the memory requirements scale only with O(N). However, the processing time for one matrix-vector multiplication is still of O(N^2). At this point now the multilevel block-Toeplitz symmetry of the matrix $\bar{\bar{A}}$ on a rectangular grid becomes relevant.
At the start it is important to define the term multilevel block-Toeplitz symmetry. A Toeplitz matrix is a matrix with the same elements along the diagonal [64]. A block-Toeplitz matrix is a matrix of blocks with the same blocks along the diagonal and in a multilevel block-Toeplitz matrix accordingly the blocks themselves are block-Toeplitz matrices, containing possibly further sub-blocks with block-Toeplitz symmetry at several levels [64]. The equations 3.24-3.26 demonstrate the concept.

$$Toeplitz = \begin{pmatrix} a & e & f & g \\ b & a & e & f \\ c & b & a & e \\ d & c & b & a \end{pmatrix} \tag{3.24}$$

$$block - Toeplitz = \begin{pmatrix} a & d & i & l \\ c & v & k & j \\ e & h & a & d \\ g & f & c & b \end{pmatrix} = \begin{pmatrix} A & C \\ B & A \end{pmatrix} \tag{3.25}$$

$$with \qquad A = \begin{pmatrix} a & d \\ c & b \end{pmatrix} B = \begin{pmatrix} e & h \\ g & f \end{pmatrix} C = \begin{pmatrix} i & l \\ k & j \end{pmatrix}$$

$$multilevelblock - Toeplitz = \begin{pmatrix} a & c & g & h \\ b & a & i & g \\ d & f & a & c \\ e & d & b & a \end{pmatrix} = \begin{pmatrix} A & C \\ B & A \end{pmatrix} \tag{3.26}$$

$$with \qquad A = \begin{pmatrix} a & c \\ b & a \end{pmatrix} B = \begin{pmatrix} d & g \\ f & d \end{pmatrix} C = \begin{pmatrix} g & h \\ i & g \end{pmatrix}$$
$$and\ possibly\ \alpha = \begin{pmatrix} \alpha & \gamma \\ \beta & \alpha \end{pmatrix}$$

In the next step it will be proven that the matrix $\bar{\bar{A}}$ is definitely a multilevel block-Toeplitz matrix. Figure 3.1 demonstrates how on a rectangular grid, if two indices are held constant, the resulting matrix for the 3rd index would be a Toeplitz matrix, as moving along the diagonals of the matrix is equivalent to moving both interacting dipoles by the same amount.

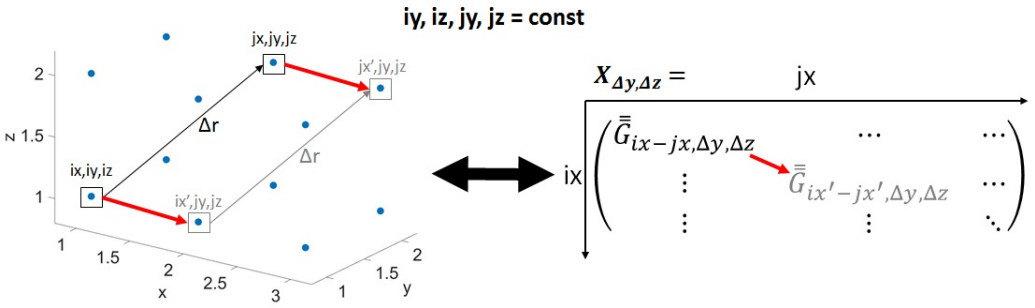

Figure 3.1: Demonstration of the Toeplitz symmetry of $X_{\Delta y,\Delta z}$, if iy, iz, jy and jz are held constant

The total matrix $\bar{\bar{A}}$ can now be constructed as a multilevel block-Toeplitz matrix by the following steps (which are demonstrated in figure 3.2). At the start a submatrix is built by keeping two indices of both interacting dipoles (iy, iz, jy, jz) constant and constructing the resulting matrix elements for all possible values of the remaining index (ix, jx). As demonstrated in fig. 3.1 the resulting submatrix is a Toeplitz matrix for all values of Δz and Δy (for a specific value of Δz and Δy it will be denoted $X_{\Delta y,\Delta z}$). Additionally the resulting submatrix will be the exact same matrix for the same values of Δy, Δz. The submatrices $X_{\Delta y,\Delta z}$ now become the blocks

at the lowest level of the matrix $\bar{\bar{A}}$. One level up the indices iz and jz are held constant and a submatrix with all possible values of the indices iy (and jy) are constructed using the submatrices $X_{\Delta y,\Delta z}$ as its building blocks. This submatrix ($Y_{\Delta z}$) is again a (block-) Toeplitz matrix, because Δy does not change when moving along the diagonals (same reason as $X_{\Delta y,\Delta z}$). The final step is to repeat the process again using the submatrices $Y_{\Delta z}$ as building blocks for the construction of a matrix of all possible values of iz (and jz), giving now the total matrix $\bar{\bar{A}}$. Thus, the matrix $\bar{\bar{A}}$ is a multilevel block-Toeplitz matrix. An explicit example of this construction can be found in the chapter on the implementation of the FFT acceleration (chapter 3.2.3).

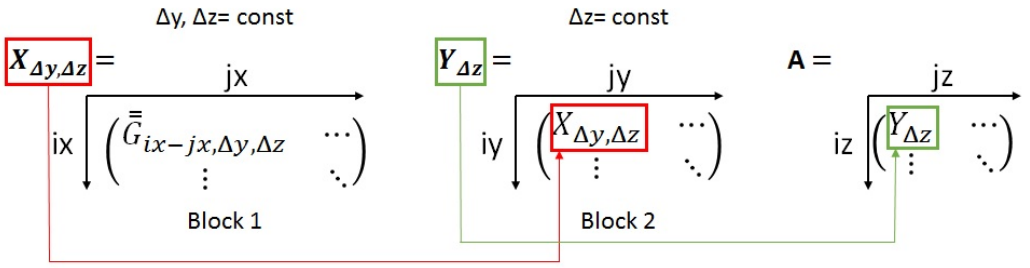

Figure 3.2: Construction of the matrix A as a multilevel block-Toeplitz matrix

For multilevel block-Toeplitz matrices (of size NxN) the matrix-vector multiplication represents a discrete convolution of two vectors of length O(N) [64]. A discrete convolution can be calculated by a simple product in Fourier space, which means that the matrix-vector product of a multilevel block-Toeplitz matrix can be calculated by a Fourier transformation of two vectors (FFT-algorithms have a computational time of Nxlog(N)), a vector product (O(N)) and an inverse Fourier transformation (O(Nxlog(N))). This reduces the overall computational complexity to O(Nxlog(N)). Several algorithms that make use of this trick to efficiently calculate the vector-matrix product for multilevel block-Toeplitz matrices exist [23, 64, 65]. From these an algorithm based on two 1-D FFTs that was specifically designed as a minimal memory method with the DDA as an application in mind [64] was used in the current DDA-script. The details of the implementation and the specific algorithm can be found in chapter 3.2.3 and appendix A.3.5, A.3.12 & A.3.13.
To briefly sum up, by using a rectangular grid and the symmetry of the Green's tensor, the computing time can be reduced to O(Nxlog(N)) and the memory requirements to O(N). The main two conditions are the

arrangement of the dipoles in a way that the distance vectors between them have recurring values and the dependence of the Green's tensor only on the relative distance between dipoles. The latter requirement will be of particular importance in the next section, where the inclusion of the influence of the substrate in the DDA will be discussed.

3.1.4 Dealing with the substrate in the DDA

Everything that has been explain up and till this point can be used to simulate a scatterer in a homogeneous background medium. However, nanostructures are usually placed on a substrate, which means that the dielectric boundary between the surrounding medium (air) and the substrate has to be taken into account as well. Several approaches to deal with this problem have been proposed over the years. The simplest is the discretization of a large enough part of the substrate [66, 67], but obviously this will dramatically increase the number of dipoles required and is unsuitable for the kind of simulations done in this thesis. Another approaches use a very crude approximation and replaces the dielectric boundary medium/substrate with a homogeneous background with an effective refractive index [68, 69]. But this crude approximation is inadequate for the simulations used in the present study. A rigorous approach (using Sommerfeld integrals) exists that modifies the Green's tensor such that he includes the influence of the substrate [70]. However, this approach breaks the symmetry of the Green's tensor in the direction of the substrate and thus limits the advantage of the FFT-acceleration to the two dimensions parallel to the substrate. Additionally, several integrals have to be evaluated numerically for every dipole to construct the Green's tensor, which is a significant computational cost for the large numbers of dipoles used in this work. Because of these restrictions the rigorous approach was not implemented in the program. It is however important to point out that Yurkin et al. [65] have shown since then that there is an opportunity to maintain the full advantage of the 3D FFT-acceleration when using the rigorous approach, which will be discussed at the end of this chapter. Finally, the approach used in this thesis is the so-called image approximation. The image approximation assumes a mirror dipole (with a modified polarization) in the substrate for every dipole in the scatterer [71, 72]. This approximation was shown to be exact in the static case (if the scatterer is small compared to the wavelength) [73] and is thus rather suitable for the simulation of scattering at nanostructures.
When using the image approximation two effects need to be considered. The interaction of the incident electric field with the substrate (transmission/re-

flection) and that of the dipoles with the substrate. The interaction of the incident field with the substrate can easily be calculated using the Fresnel equations and simply added to the incident field, requiring no modification of the DDA algorithm (see appendix A.3.12 for the implementation). The interaction between the substrate and the dipoles is approximated by placing a "mirror" dipole (original dipole coordinate x,y,z => mirror dipole at x,y,-z) into the substrate, as illustrated in fig.3.3.

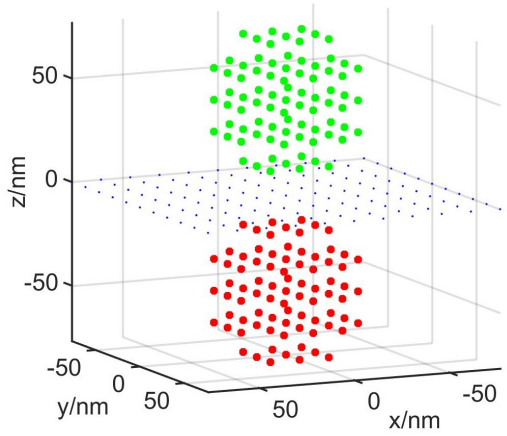

Figure 3.3: Schematic drawing of the mirror dipoles (red) and "scatterer" dipoles (green), the substrate surface is indicated by the blue dots

The polarization of the mirror dipoles depends both on the dielectric constant of the substrate and the polarization of the dipole they are mirroring (see eq. 3.27 [71]).

$$\widetilde{P_{\parallel}} = -\frac{\epsilon_{sub} - 1}{\epsilon_{sub} + 1} \cdot P_{\parallel} \qquad \widetilde{P_{\perp}} = \frac{\epsilon_{sub} - 1}{\epsilon_{sub} + 1} \cdot P_{\perp} \tag{3.27}$$

with $\widetilde{P_{\parallel}}(\widetilde{P_{\perp}})$ the polarization of the mirror dipole, the subscript denoting an orientation parallel (perpendicular) to the substrate, ϵ_{sub} the dielectric constant of the substrate and $P_{\parallel}(P_{\perp})$ the polarization of the "original" dipole, the subscript denoting an orientation parallel (perpendicular) to the substrate.

The mirror dipoles can be included in the simulation while maintaining the full advantage of the 3D FFT-acceleration by extension of the boundary

box below the substrate and inclusion of the mirror dipoles in the simulation. The polarizations of the mirror dipoles are then forced to obey eq. 3.27 during every iterative step of the GMRES-solver. The details of the implementation can be found in chapter 3.2.4 and appendix A.3.12. Using this approach the substrate is included in the simulations at the cost of doubling the number of dipoles and assuming the static case for the dipole-substrate interaction (scatterer is small compared to the wavelength).
As already mentioned above, since the start of this thesis, Yurkin et al. [65] developed a procedure to maintain the full advantage of the 3D FFT-acceleration whilst using the rigorous approach to the substrate-dipole interaction. They accomplished this by splitting the rigorous Green's tensor (with substrate interaction) into a term that is equivalent to the mirror approximation and another term that contains the Sommerfeld integrals. The matrix-vector product in eq. 3.20 can then be split into three contributions: the "original" Green's tensor, the "mirror approximation" Green's tensor and the "Sommerfeld integrals" Green's tensor. They also found a way to rearrange the polarization vector (for every product differently) in eq. 3.20 in such a way that the 3D-FFT acceleration can still be used for the product. This offers two possibilities for further improvement of the algorithm presented here. Firstly, by use of the mirror approximation in combination with the above rearrangement scheme the memory requirements and computational time of the algorithm presented in this thesis can probably be reduced by about a factor of $\sqrt{2}$. Secondly, the static approximation assumption can be removed (by fully implementing the above approach). This however would entail an increase in computing time (comparable to a full integration of the tensor; see chapter 3.1.2 and 3.2.1), as the Sommerfeld integrals have to be evaluated for every tensor element (on the order of 10^8 integrals for the maximum amount of dipoles used in this thesis).

3.2 The main DDA program

In the previous chapter the fundamental aspects of the DDA have been discussed. This chapter will deal with the most important practical issues concerning the software implementation. In particular, the partial integration of the tensor, the numbering and storage convention used, the specific FFT-acceleration algorithm used, the integration of the substrate into the DDA and the generation of the geometry from AFM images are discussed. Additionally, a summary of all the input parameters (and their default values) as well as a summary of all the preprogramed output graphics and files provided in appendix A.1 & A.2. All of the source code can be found in appendix A.3, and subchapters containing relevant code will be referenced where necessary. Additionally, references to the appropriate subchapter in the fundamentals chapter will be made and, for a thorough understanding, it is highly recommended to read the fundamentals chapter (in detail!) first.

3.2.1 Partial tensor integration

The fundamentals of the integrated tensor approach can be found in chapter 3.1.2. As already stated there, the integration of the self-term (and thereby the determination of the polarizability tensor) can easily be done set out in the work of [61]. This part of the integrated tensor approach needs no further discussion and the source code can be found in appendix A.3.8. What is more interesting is the issue concerning the integration of the off diagonal tensor elements of the Green's tensor. As already explained in the fundamentals chapter, the full integration of the Green's tensor is a significant improvement compared to the integration of only the diagonal elements (only determining the polarizabilities by integration) [61]. Unfortunately this requires the evaluation of several integrals per dipole, which causes high computational costs. In this thesis a novel approach is used that integrates the tensor to a certain depth (a certain number of off diagonals). This is possible as the values of the integrated and the simple "constant" tensor elements converge for large distances (note that they also converge for small discretization step sizes).
The implementation of this approach is rather trivial. The number of discretization steps (in all directions) for which the tensor is fully integrated is specified by an input variable. All elements that are not fully integrated are determined using the constant tensor assumption (equation 3.13 and appendix A.3.11). Note that a depth of x discretization steps fully integrated is equivalent to $(2x+1)^3-1$ off-diagonals being integrated, as demonstrated

in figure 3.4.

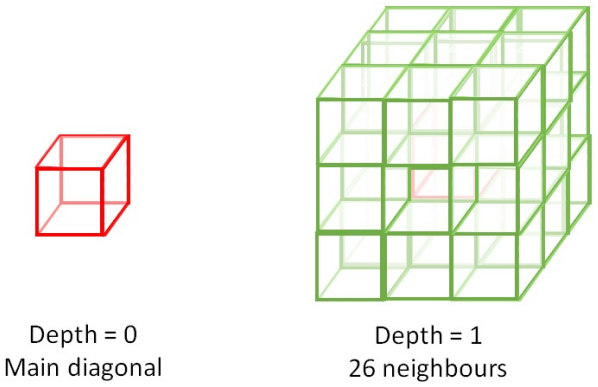

Figure 3.4: Schematic drawing illustrating the term depth of discretization steps. The cubes represent 1 discretization volume

A default value of a depth of 5 discretization steps (1330 off-diagonals) was used for all simulations in this thesis. This is possible, because the Green's tensors elements depend mostly on the discretization step size (and only weakly on the wavelength of the incident field). Therefor it is sufficient to look once at the convergence of the integrated and "constant" tensor elements for the default discretization step size (0.5 nm) and choose an appropriate value for the number of fully discretization steps where full integration of the Green´s tensor will be performed. Figure 3.5 shows the difference (as defined by eq. 3.28) between the integrated and "constant" tensor for a "shell" (outermost dipoles at a certain depth) as a function of discretization step depth (the discretization step size is 0.5 nm). Only the tensor element with the largest error is shown for clarity. It is apparent that the relative difference (between the constant and integrated tensor) rapidly decreases and at a depth of 5 discretization steps it is already insignificant (approximately 10^{-4}).

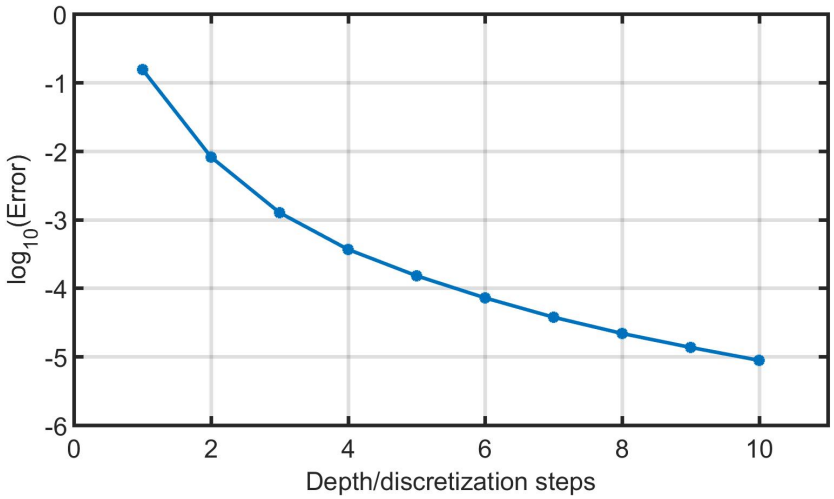

Figure 3.5: Logarithmic plot of the Error (see eq. 3.28) as a function of depth of discretization steps; only the tensor element that produces the largest error is shown

$$Error = \frac{\sum_S \left| \bar{\bar{G}}^{IT} - \bar{\bar{G}}^{const} \right|}{\sum_S \left| \bar{\bar{G}}^{IT} \right|} \tag{3.28}$$

with *Error* the relative difference between the integrated and "constant" tensor elements, S denoting the sum over a "shell" of dipoles of a certain depth, $\bar{\bar{G}}^{IT}$ the integrated Green's tensor and $\bar{\bar{G}}^{const}$ the "constant" Green's tensor (as defined by eq. 3.14 and 3.13).

3.2.2 Numbering and storage convention

Understanding the numbering convention of the dipoles on the rectangular grid and the convention by which the values for the electric fields, polarizations and so on are stored is essential if any analysis beyond the preprogramed analysis is desired. This knowledge is also essential in order to understand the FFT acceleration algorithm. Therefore both conventions are explained in Fig. 3.6 using the example of a 2x2x2 grid of dipoles. The generation of the grid is done by the code in appendix A.3.5, and appendix A.3.9 shows an example for the generation of a vector of fields.

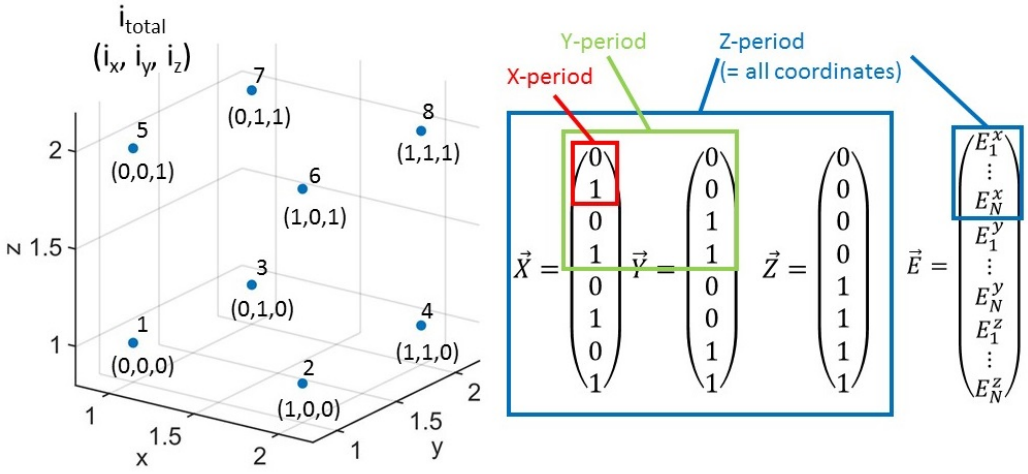

Figure 3.6: Demonstration of the numbering of the dipoles and the storage convention for coordinates and vectors using the example of a 2x2x2 grid

As shown in figure 3.6 all coordinates are stored in 3-vectors (X, Y, Z) of size N (N number of dipoles), with the index of the vectors given by equations 3.29.

$$i_{total} = n_x \cdot n_y \cdot (i_z - i_z^0) + n_x \cdot (i_y - i_y^0) + (i_x - i_x^0) + 1 \tag{3.29}$$

with i_{total} the index of the dipole, $n_x(n_y)$ the number of discretization steps in the x-direction (y-direction), $i_x(i_y; i_z)$ the grid coordinate index of the dipole in x-direction (y-direction; z-direction) and $i_x^0(i_y^0; i_z^0)$ the grid coordinate index of the dipole in the bottom-left-front corner of the grid in x-direction (y-direction; z-direction).
The construction of eq. 3.29 is straightforward. Starting from the bottom-left-front dipole (in this case [0,0,0] though not necessarily) the index first moves all the way along the x-direction, then to the next row in the y-direction (repeat until the end in y is reached) and after that one layer up in the z-direction (repeat until the end in z is reached). This is similar to the construction of the matrix A in chapter 3.1.3 and in fact the resulting symmetries that are crucial for the FFT-acceleration are indicated in figure 3.6 and 3.7. The electric fields and polarizations, which are 3D-vectors for every dipole position, are stored as indicated in fig. 3.6 in vectors of length

3xN, with the first N values being those in the x-direction of the vector in the same order as the dipole numbering, the second N values those in the y-direction and the third N values those in the z-direction. Since the polarizability tensor is always isotropic for cubic discretization volumes [51], only one value per dipole needs to be stored and a vector of length N is sufficient (see appendix A.3.5, A.3.8). If desired, the generalization to non-isotropic polarizabilities is trivial and could be done in the exact same way the Green's tensor is treated in chapter 3.2.3 (appendix A.3.11). The storage of the Green's tensor is discussed together with the FFT acceleration algorithm as both are closely related.

3.2.3 The fast Fourier transformation acceleration algorithm

The FFT acceleration implemented into the DDA script developed in this thesis, is largely based on the algorithm from [64]. As shown in chapter 3.1.3 the matrix A can be constructed as a block-Toeplitz matrix, but the fundamental elements of the matrix structure presented there are still 3x3 tensors that need to be multiplied with a 3x1 vector (with the result of course also a 3x1 vector). While it would be possible to construct the matrix A similarly, from a practical coding point of view it would be much more convenient to work only with single numbers, rather than vectors or tensors. Luckily, we can simply deconstruct the tensor vector product on the lowest level of the matrix A as indicated in eq. 3.30-3.34 and then the total matrix-vector product (with tensors as fundamental elements) can be written as 9 matrix vector products (with only numbers as fundamental elements; see appendix A.3.12). As a side note this has the additional benefit of reducing the storage requirement as of the 9 elements of the Green's tensor only 6 are unique (see eq.3.34).

$$\vec{\tilde{v}} = \bar{\bar{A}} \cdot \vec{\tilde{P}} \tag{3.30}$$

$$with \qquad \vec{\tilde{v}} = \begin{pmatrix} \vec{v}_i \\ \vec{v}_j \\ \vdots \end{pmatrix} \vec{\tilde{P}} = \begin{pmatrix} \vec{P}_i \\ \vec{P}_j \\ \vdots \end{pmatrix} \bar{\bar{A}} = \begin{pmatrix} 0 & \bar{\bar{G}}_{ij} & \cdots \\ \bar{\bar{G}}_{ji} & 0 \cdots & \\ \vdots & \vdots & \ddots \end{pmatrix}$$

$$\vec{v}_i = \sum_j \bar{\bar{G}}_{ij} \cdot \vec{P}_j \tag{3.31}$$

$$\bar{\bar{G}}_{ij} \cdot \vec{P}_j = \begin{pmatrix} G_{ij}^{xx} & G_{ij}^{xy} & G_{ij}^{xz} \\ G_{ij}^{yx} & G_{ij}^{yy} & G_{ij}^{yz} \\ G_{ij}^{zx} & G_{ij}^{zy} & G_{ij}^{zz} \end{pmatrix} \cdot \begin{pmatrix} P_j^x \\ P_j^y \\ P_j^z \end{pmatrix} = \begin{matrix} G_{ij}^{xx} \cdot P_j^x + G_{ij}^{xy} \cdot P_j^y + G_{ij}^{xz} \cdot P_j^z \\ G_{ij}^{yx} \cdot P_j^x + G_{ij}^{yy} \cdot P_j^y + G_{ij}^{yz} \cdot P_j^z \\ G_{ij}^{zx} \cdot P_j^x + G_{ij}^{zy} \cdot P_j^y + G_{ij}^{zz} \cdot P_j^z \end{matrix} \tag{3.32}$$

$$\vec{P}^x := \begin{pmatrix} P_i^x \\ P_j^x \\ \vdots \end{pmatrix} \wedge \bar{\bar{G}}^{xx} := \begin{pmatrix} 0 & G_{ij}^{xx} & \cdots \\ G_{ji}^{xx} & 0 & \cdots \\ \vdots & \vdots & \ddots \end{pmatrix} \wedge \begin{matrix} G_{ij}^{yx} = G_{ij}^{xy} \\ G_{ij}^{zx} = G_{ij}^{xz} \\ G_{ij}^{zy} = G_{ij}^{yz} \end{matrix} \tag{3.33}$$

$$\begin{aligned} \vec{v}^x &= \bar{\bar{G}}^{xx} \cdot \vec{P}^x + \bar{\bar{G}}^{xy} \cdot \vec{P}^y + \bar{\bar{G}}^{xz} \cdot \vec{P}^z \\ \vec{v}^y &= \bar{\bar{G}}^{xy} \cdot \vec{P}^x + \bar{\bar{G}}^{yy} \cdot \vec{P}^y + \bar{\bar{G}}^{yz} \cdot \vec{P}^z \\ \vec{v}^z &= \bar{\bar{G}}^{xz} \cdot \vec{P}^x + \bar{\bar{G}}^{yz} \cdot \vec{P}^y + \bar{\bar{G}}^{zz} \cdot \vec{P}^z \end{aligned} \tag{3.34}$$

with 6 *matrices to be stored* : $\bar{\bar{G}}^{xx}, \bar{\bar{G}}^{yy}, \bar{\bar{G}}^{zz}, \bar{\bar{G}}^{xy}, \bar{\bar{G}}^{xz}, \bar{\bar{G}}^{yz}$

The next step is the calculation of the 9 matrix-vector products with the fundamental elements being only numbers. This will be discussed using the example of $\bar{\bar{G}}^{xx}$ and $\vec{P}^x$ and the exemplary 2x2x2 grid from figure 3.6. The full matrix construction of $\bar{\bar{G}}^{xx}$ is shown in figure 3.7, with the 3 indices for the dipoles written explicitly as ix, iy, iz (rather than as one index as suggested in eq. x) to demonstrate the symmetries. The symmetries (blocks) are also indicated with the same colours as in figure 3.6.

$$\bar{\bar{G}}^{xx} = \begin{pmatrix} 0 & G^{xx}_{-1,0,0} & G^{xx}_{0,-1,0} & G^{xx}_{-1,-1,0} & G^{xx}_{0,0,-1} & G^{xx}_{-1,0,-1} & G^{xx}_{0,-1,-1} & G^{xx}_{-1,-1,-1} \\ G^{xx}_{1,0,0} & 0 & G^{xx}_{1,-1,0} & G^{xx}_{0,-1,0} & G^{xx}_{1,0,-1} & G^{xx}_{0,0,-1} & G^{xx}_{1,-1,-1} & G^{xx}_{0,-1,-1} \\ G^{xx}_{0,1,0} & G^{xx}_{-1,1,0} & 0 & G^{xx}_{-1,0,0} & G^{xx}_{0,1,-1} & G^{xx}_{-1,1,-1} & G^{xx}_{0,0,-1} & G^{xx}_{-1,0,-1} \\ G^{xx}_{1,1,0} & G^{xx}_{0,1,0} & G^{xx}_{1,0,0} & 0 & G^{xx}_{1,1,-1} & G^{xx}_{0,1,-1} & G^{xx}_{1,0,-1} & G^{xx}_{0,0,-1} \\ G^{xx}_{0,0,1} & G^{xx}_{-1,0,1} & G^{xx}_{0,-1,1} & G^{xx}_{-1,-1,1} & 0 & G^{xx}_{-1,0,0} & G^{xx}_{0,-1,0} & G^{xx}_{-1,-1,0} \\ G^{xx}_{1,0,1} & G^{xx}_{0,0,1} & G^{xx}_{1,-1,1} & G^{xx}_{0,-1,1} & G^{xx}_{1,0,0} & 0 & G^{xx}_{1,-1,0} & G^{xx}_{0,-1,0} \\ G^{xx}_{0,1,1} & G^{xx}_{-1,1,1} & G^{xx}_{0,0,1} & G^{xx}_{-1,0,1} & G^{xx}_{0,1,0} & G^{xx}_{-1,1,0} & 0 & G^{xx}_{-1,0,0} \\ G^{xx}_{1,1,1} & G^{xx}_{0,1,1} & G^{xx}_{1,0,1} & G^{xx}_{0,0,1} & G^{xx}_{1,1,0} & G^{xx}_{0,1,0} & G^{xx}_{1,0,0} & 0 \end{pmatrix} \cdot \vec{P}^{x} = \begin{pmatrix} P^{x}_{0,0,0} \\ P^{x}_{1,0,0} \\ P^{x}_{0,1,0} \\ P^{x}_{1,1,0} \\ P^{x}_{0,0,1} \\ P^{x}_{1,0,1} \\ P^{x}_{0,1,1} \\ P^{x}_{1,1,1} \end{pmatrix}$$

Figure 3.7: $\bar{\bar{G}}^{xx} \cdot \vec{P}^{x}$ explicitly written for the 2x2x2 grid from figure x. The block-Toeplitz symmetries due to the recurring distances in x (red), y (green) and z (blue) are indicated in the same way as in figure 3.6

The unique elements of the tensor can be written as a vector ($\vec{A}$) as shown in figure 3.8 and the vector $\vec{P}^{x}$ can be (periodically) extended by inserting zeros at appropriate positions (see the variable var.Ih(:,2) in appendix A.3.11 and A.3.13) such that the vector-matrix product (from figure 3.7) becomes a discrete convolution [64]. A discrete convolution can be imagined as (periodically) sliding the extended vector $\vec{P}^{x}$ up and down the vector $\vec{A}$ in figure 3.8. As is shown in figure 3.8 for the appropriate position in the convolution the product of $\vec{A}$ with the extended vector $\vec{P}^{x}$ produces exactly the same product as any given line in the matrix vector multiplication in figure 3.7 (in the example the first line of the matrix-vector product would be produced).

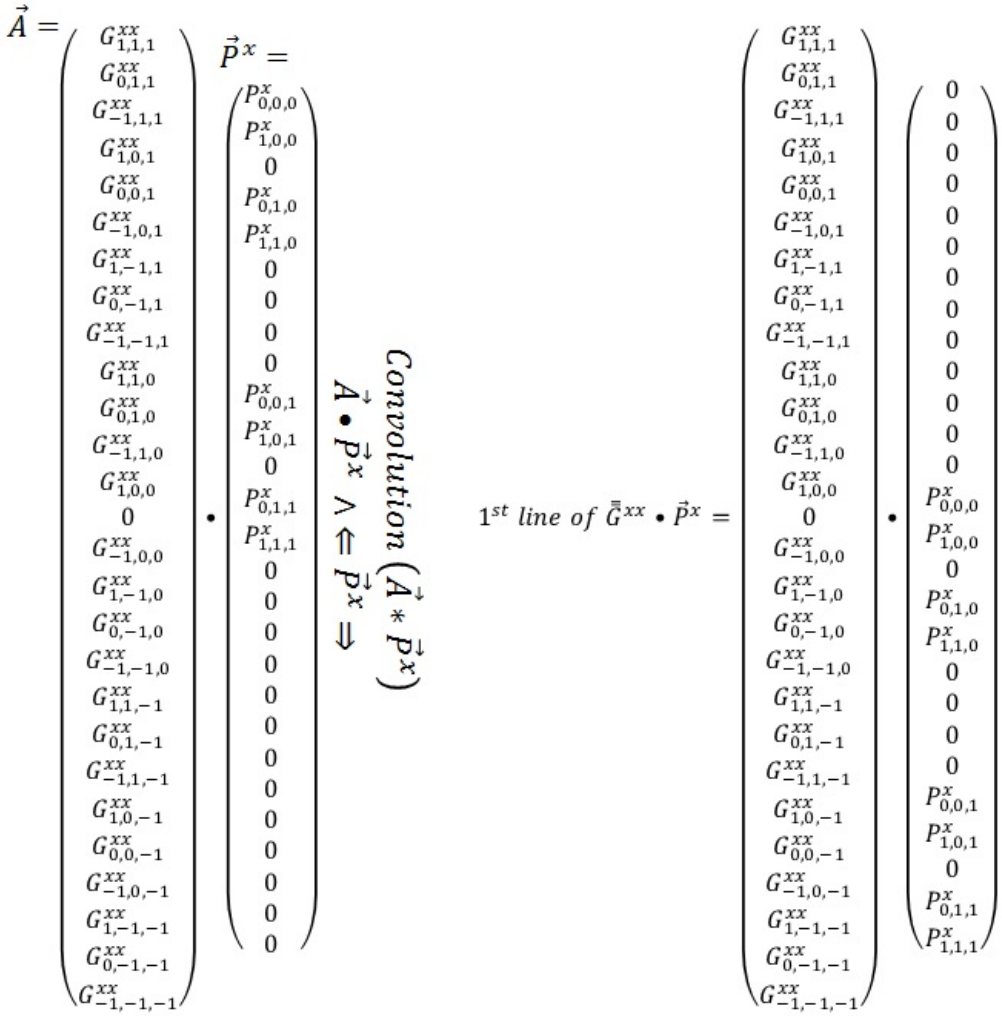

Figure 3.8: Demonstration of how the tensors are written as vectors and how the convolution of the "tensor" vectors with the extended polarization vectors can produce the vector-matrix product in figure 3.7

Since a discrete convolution can easily be calculated by a simple product in Fourier space [64], a vector (see vector Yh in appendix A.3.13) containing all possible "sliding"-positions can be calculated using two Fourier transformations ($\mathcal{F}(\vec{P}^x); \mathcal{F}^{-1}(...)$), as shown in eq 3.35. Note that the vector ($\vec{A}$) containing the matrix elements of $\bar{\bar{G}}^{xx}$ is only ever required in Fourier space which is why it is immediately Fourier transformed after it is created by the function in appendix A.3.11 and only its representation in Fourier space is stored (variable var.A in the function doing the product in Fourier space; see appendix A.3.13).

$$Yh = \left(\vec{A} * \vec{P}^x\right) = \mathcal{F}^{-1}\left(\mathcal{F}(\vec{A}) \cdot \mathcal{F}(\vec{P}^x)\right) \tag{3.35}$$

As already shown in figure 3.8, any line of the matrix-vector product (see figure 3.7) is produced by an appropriate position in the convolution. All that remains to be done to get the vector (Y) resulting from the matrix-vector product is to select those positions from the vector Yh containing all possible sliding positions. This is done by the variable var.Ih(:,1) in the code in appendix A.3.11 and appendix A.3.13.

3.2.4 Implementation of the image approximation

As already explained in chapter 3.1.4 the substrate is integrated into the simulation using the image approximation. For the most part the implementation of the image approximation is rather trivial. The bounding box must be appropriately extended below the substrate, which is done by defining z=0 as the substrate position and using a bounding box from $-z_{max}$ to z_{max}, rather than 0 to z_{max} in the non-substrate case (see chapter 3.2.5 and appendix A.3.5). Additionally, the reflection/transmission of the incident field must be calculated using Fresnel's equations and added to the incident field vector (see appendix A.3.9). Apart from that that the DDA algorithm is the same as in the non-substrate case (as no changes to the tensor A and the polarizabilities are required; see eq. 3.20) except for one important detail: The polarizations of the image dipoles must obey the eq. 3.27, which is a bit tricky as the iterative solver updates the polarization vector (see eq. 3.20) at every iterative step and thereupon does not necessarily obey eq. 3.27. This issue has been solved by a change of the function evaluating the vector-matrix product (see appendix A.3.12), as demonstrated in the lines of the code below.

```
1
2       if par.substrat_quasi(1)==1
3       %Some parameters are generated
4           nz=ceil(result_dda.n(3)./2);
5           eps_sub=par.substrat_quasi(2);
6           nm=par.m_media;
7           Ref=(eps_sub-nm)./(eps_sub+nm);
```

```
8
9       %The polarization vector is flip and rearranges to ...
           reflect the quasi-static substrate
10      Px=P(1:N);
11      Px=reshape(Px,[],nz.*2+1);
12      Px(:,1:nz)=-1.*Ref.*fliplr(Px(:,nz+2:end));
13      P(1:N)=Px(:);
14
15
16      Py=P((N+1):2*N);
17      Py=reshape(Py,[],nz.*2+1);
18      Py(:,1:nz)=-1.*Ref.*fliplr(Py(:,nz+2:end));
19      P((N+1):2*N)=Py(:);
20
21
22      Pz=P((2*N+1):3*N);
23      Pz=reshape(Pz,[],nz.*2+1);
24      Pz(:,1:nz)=Ref.*fliplr(Pz(:,nz+2:end));
25      P((2*N+1):3*N)=Pz(:);
26    end
```

If the substrate flag is set these lines of code are executed in the function that calculates the vector-matrix product immediately before the product itself is calculated. The lines get the polarization vector of all dipoles with a positive z value (real dipoles), flip that vector as the order of the mirror dipoles in the z direction is reversed (one might even call it mirrored) and then replaces the values of all dipoles with a negative z value in the polarization vector according to eq.3.27. Since this is done every time the vector-matrix product is evaluated (and all relevant calculations require that product), the mirror dipoles are effectively forced to obey eq. 3.27 by this simple change to the vector-matrix product function.
An additional important point concerning the substrate is related to the default dielectric constant used for all substrate simulations in this thesis. It is that of SiO_2 (taken from [74]), despite the fact that the substrates used in the experiments are Si wafers. The dielectric constant of SiO_2 was chosen because SEM images of the cross-sections of the Si wafers revealed a surprisingly thick SiO_2 layer with an approximate thickness of 2.5 µm (see fig. 3.9). Therefor the substrate was treated as a pure SiO_2 substrate in the simulations and the influence of the (in nanostructure terms) relatively far below Si was ignored.

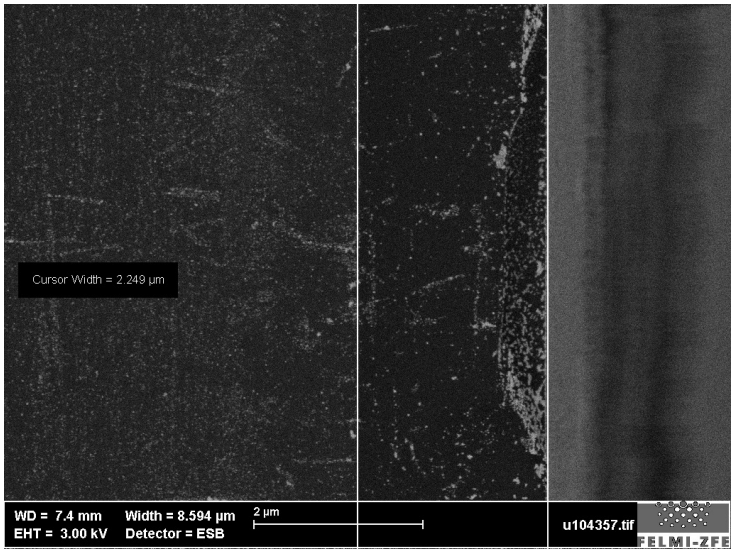

Figure 3.9: SEM image of the cross section of one of the Si wafers. The SiO_2 layer is marked by the cursors and was confirmed by EDX

3.2.5 Generation of the 3D-discretization form an AFM image

An important novelty of this thesis is, that the geometry of the nanostructures is not approximated by simple geometric shapes, but the discretization is done from an AFM image with a resolution comparable to the pixel resolution of an AFM. Thereby the simulated geometry is the closest representation of the actual geometry that can be measured (with an AFM). Since this is one of the key improvements of this thesis compared to other nearfield simulations, the necessary steps leading from an AFM image (as measured) to the final geometry that is used in the simulations will now be discussed in detail. This includes both preprocessing steps of the measured data (in the case of this thesis done with Gwyddion) and the implementation of the AFM image by the DDA program. For a clearer understanding a specific example will be used for the discussion.
The discussion starts with an AFM image (see fig.3.10) of a substrate that has been measured as outlined in chapter 2.2.

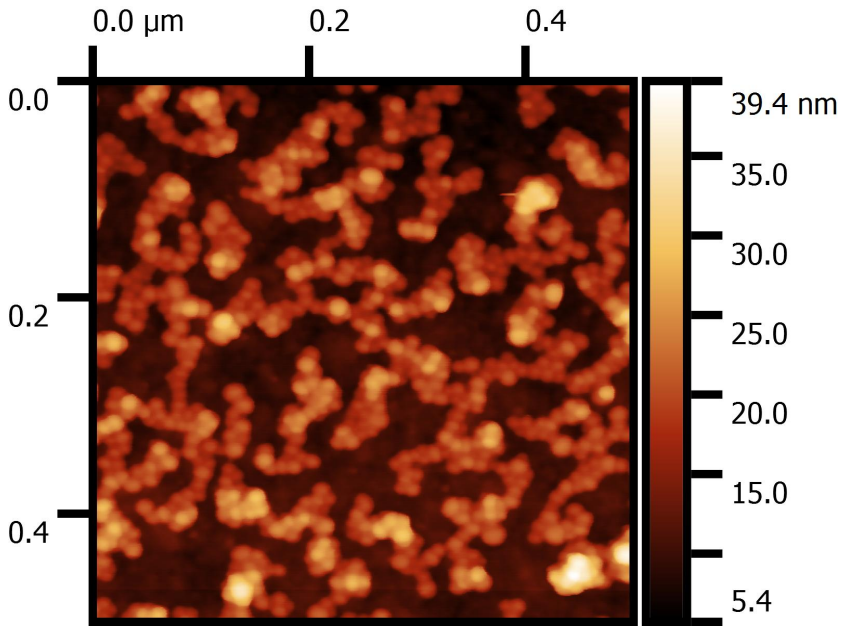

Figure 3.10: AFM image as measured (see chapter 2.2)

The simulation algorithm will assume a perfectly flat substrate at the position z=0 nm. An important side note, the restriction of a perfectly flat substrate (an infinitely large plane dielectric boundary) is inherent in the mirror approximation (it is also inherent in the analytical Sommerfeld integral approach). To accomplish this the substrate needs to be flattened, as the substrate is often slightly tilted during the AFM measurements, and of course the substrate has a certain roughness. First a standard flattening procedure is applied to remove any tilt from the image, additionally scar removal filters are applied. These first steps involve the *Level data by mean plane subtraction* (potentially in severe cases also Correct lines by matching height median) and *Correct horizontal scar (strokes)* functions of Gwyddion and the respective results are shown in figures 3.11 and 3.12.

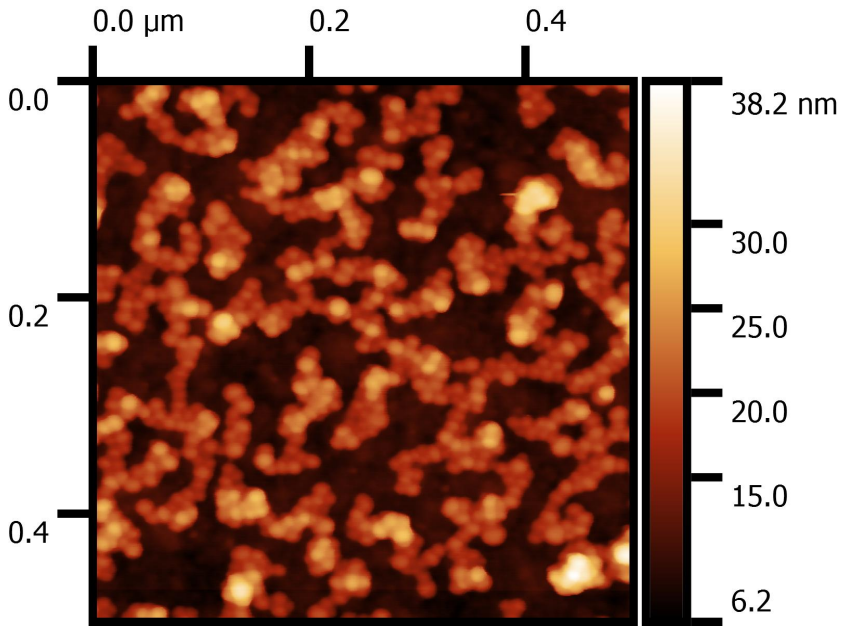

Figure 3.11: AFM image after the tilt has been removed

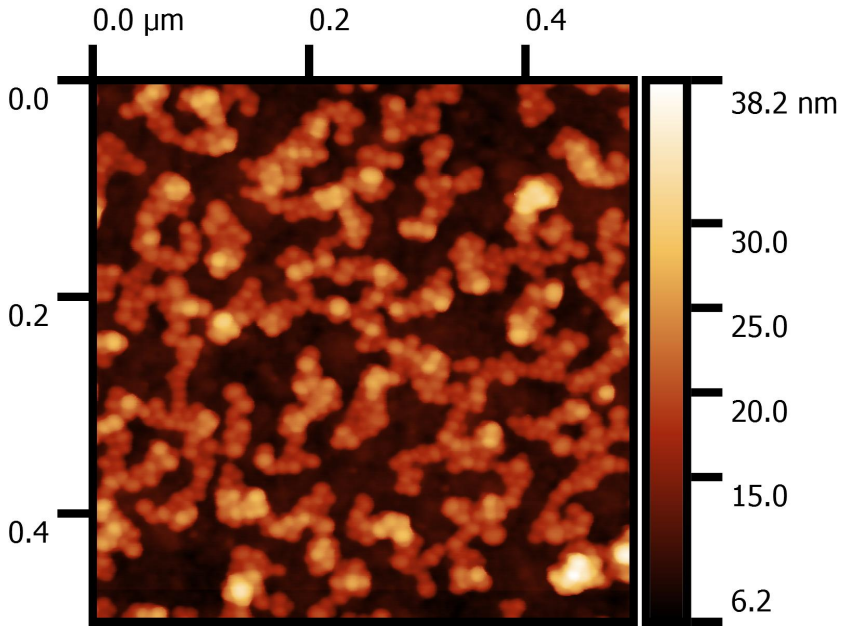

Figure 3.12: AFM image after the scars have been removed

In the next step the roughness of the substrate has to be removed. This is done by carefully marking the substrate positions in the image with a threshold mask applied to the height and phase images. At this step great

care has to be taken that the mask accurately marks the substrate positions, sometimes even manual corrections to the mask might be necessary. If appropriate, the *Interpolate data under the mask by solution of Laplace equation* function can be used to "pre-flatten" some marked regions, which can make it easier to accurately mask the substrate. Figure 3.13 shows an example of an appropriate mask.

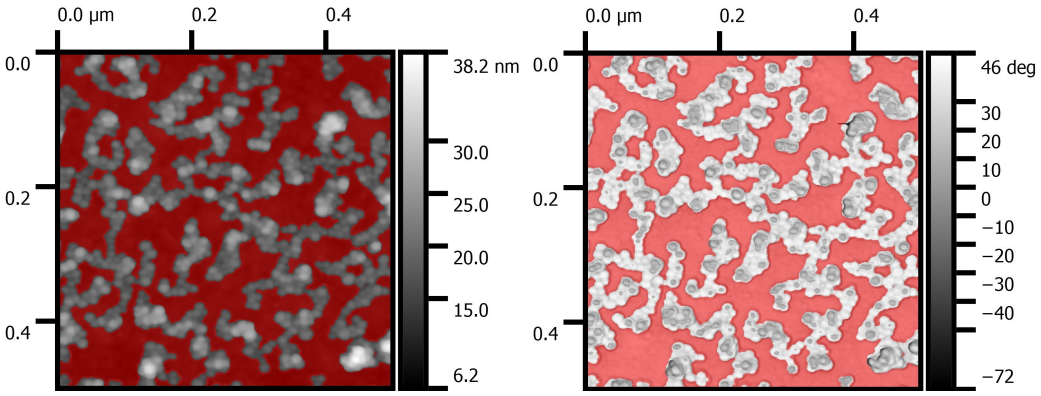

Figure 3.13: AFM image (height left and phase right) with the substrate-mask (red) set. Both images are plotted with a grey colorbar in order to make the mask clearly visible

The next step is the removal of the roughness of the substrate using first *the Interpolate data under the mask by solution of Laplace equation* function to the masked region to avoid artificial sharp edges and then the replacement of the masked region with a perfectly flat surface (*Limit range* function). Finally, the position of the substrate is set to z=0 using the *Shift minimum data value to zero* function (see fig.3.14). In the final preprocessing step a median filter is applied in order to avoid sub-nanometer kinks due to noise (see fig.3.15).

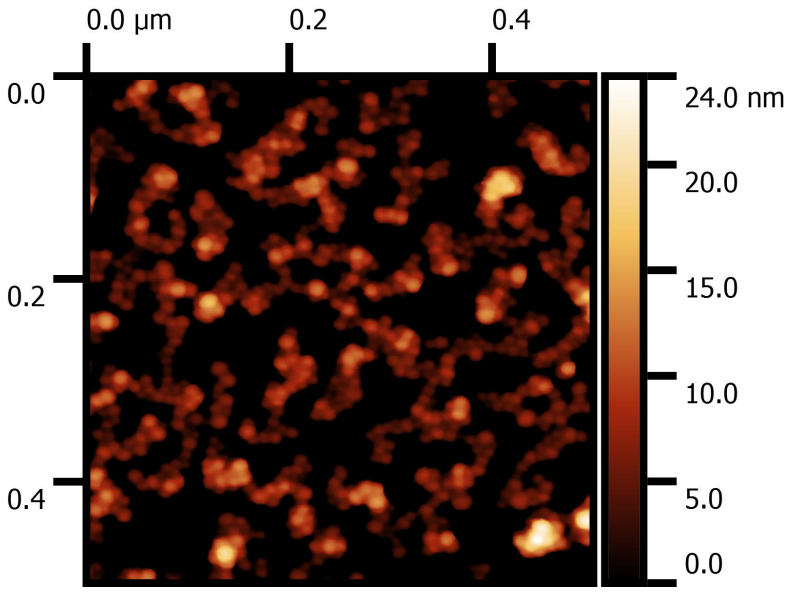

Figure 3.14: AFM image after the substrate surface as measured was replace by a perfectly flat surface and the respective heights were shifted to zero

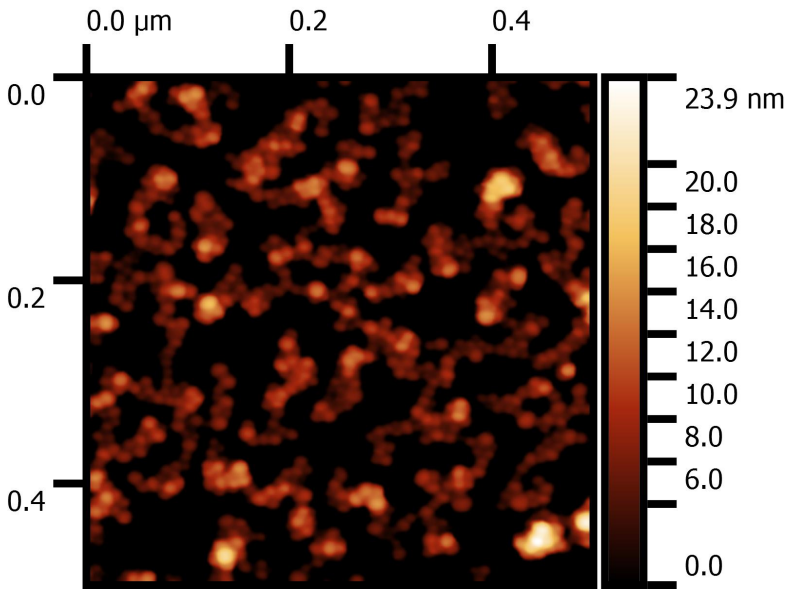

Figure 3.15: AFM image after the median filter has been applied. This is the image that is implemented by the DDA program

The AFM image as shown in Fig. 3.15 is suitable as an input for the simulations. It is therefore exported as an ASCII file. The file contains

the height information, additionally the size of the measured area (length of x- and y- axis) is required to generate the geometry for the simulation. Usually, the AFM image will be bigger than the area that will eventually be used in the simulations (maximum simulation size approx. 200x200 nm for 0.5 nm discretization step size), but for practical purposes (for instance automatically simulating several regions of interest consecutively) the entire AFM image is always given to the DDA program and the region of interested is selected later.
The AFM image at this point is essentially a pointwise (pixel!) representation of the surface of the nanostructures. The first step in the DDA program is to interpolate this pointwise information using the TriScatteredInterp function of Matlab. This generates a function called AFM that will give the height (z value) of the surface of the nanostructure for any position (x, y value) within the limits of the AFM image. The region of interest is also inherently selected by the function AFM, as the coordinates of this function (in x and y) are simply shifted such that the central point of the region of interest is [0,0] in the coordinates of the function AFM. The respective code can be found in appendix A.3.2. Figure 3.16 shows the resulting function evaluated with twice the resolution of that of the AFM image in figure 3.15.

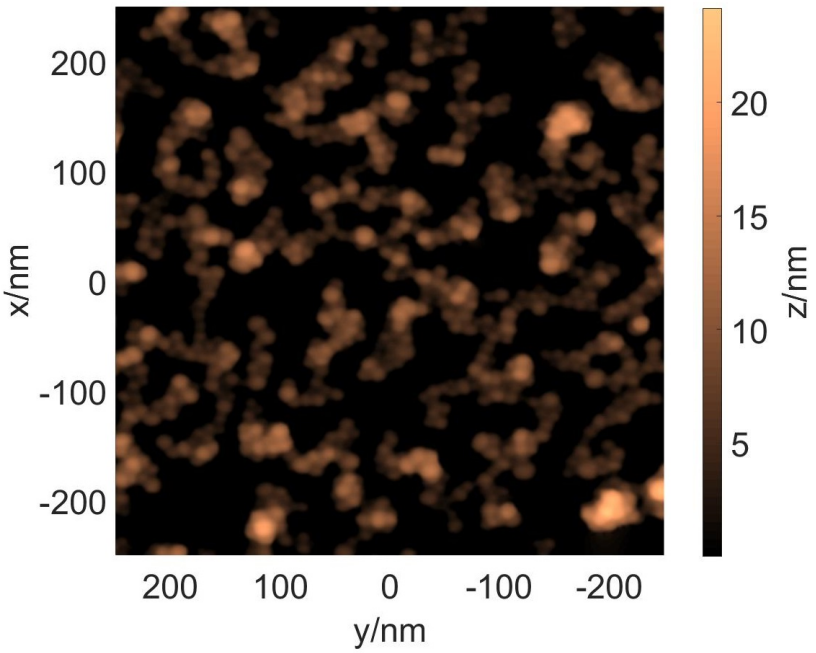

Figure 3.16: The function AFM that corresponds to the AFM image in figure 3.15 evaluated at twice the resolution of that of the AFM image

The next step is to generate the discretization grid for the simulation. At this point it is important to point out that only the number of discretization steps (in x, y and z separately) is specified by the input parameters of the simulation program. The size of the discretization steps is determined automatically by the function dtight.m such (see appendix A.3.6) that the grid tightly fits the geometry. This is accomplished by the determination of the minimal discretization step size required to encompass the entire structure for every coordinate axis separately, and then choosing the largest of the three resulting values. For the x- and y- axis this is done by dividing the parameter giving the desired size of the area used in the simulation (par.xlimit and par.ylimit) by the number of discretization steps in x and y respectively. The discretization step size for the z-axis is given by the highest point in the AFM image divided by the number of discretization steps in z. Note that the number of discretization steps in z is automatically doubled by the program after the determination of the discretization step size, if the substrate flag is set. Finally, with the discretization step size, the number of discretization steps and the zero position of the grid relative to the AFM image defined, the geometry can be generated by checking for every dipole if it is positioned in-between the substrate (z=0) and the surface of the nanostructure (z=AFM(x,y); see appendix y). Figure 3.17 shows an example referring to this (with a low resolution discretization for clarity; center of the region of interest at [-100 nm,-100 nm]) and figure 3.18 shows a geometry generated from the example image in fig. z with a discretization of 0.5 nm.

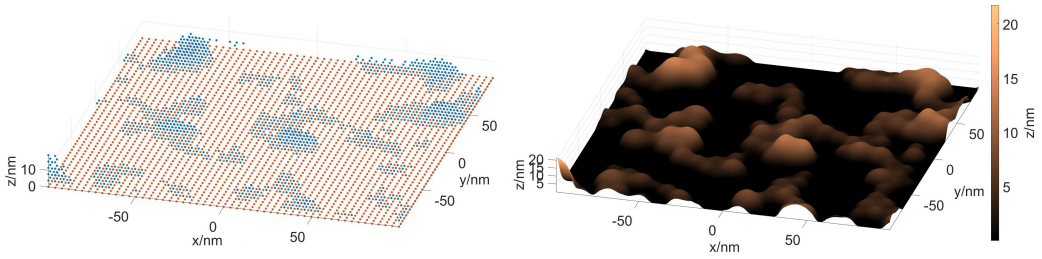

Figure 3.17: Example of the discretization of a region of interest, a low resolution discretization was used in order to clearly show the positions of the dipoles

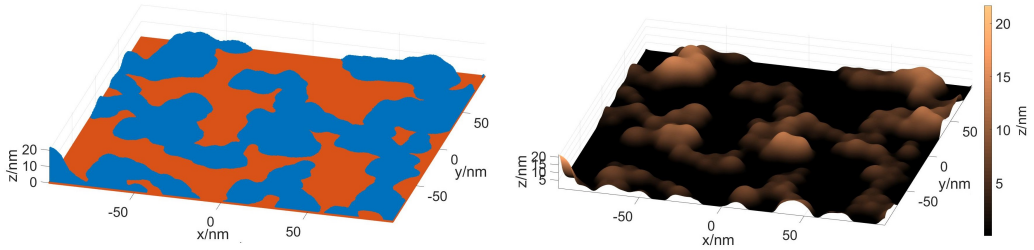

Figure 3.18: Example of the discretization of a region of interest with the default discretization step size of 0.5 nm

Using the geometry from figure 3.18 the simulation can be run and the electric near fields can be calculated. However, in order to avoid edge effects one final step is required, namely the reduction of the simulated area by 10% (on each side) after the simulation is finished (see fig. 3.19).

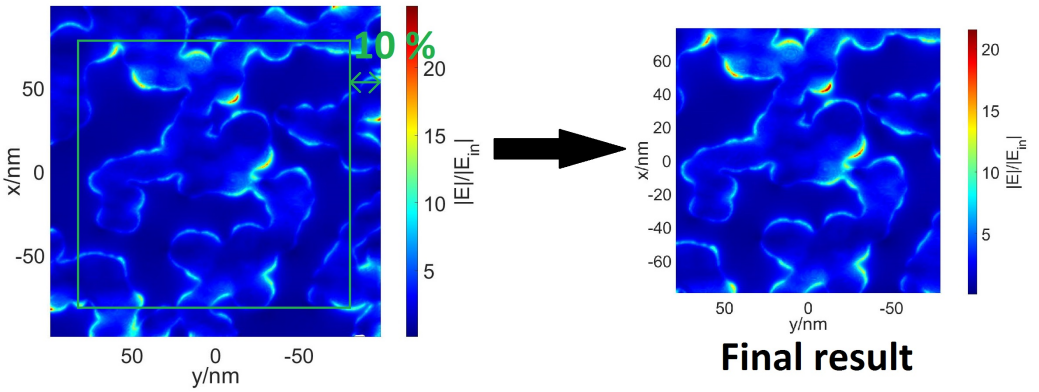

Figure 3.19: Calculation of the electric fields using the DDA. To avoid edge effects, the simulated area is cropped by 10% at each side

3.3 Algorithm and parameter test

Thus far, the basic principles of the DDA and a detailed account of the implementation were provided. However, the accuracy of the simulations also needs to be addressed.
At the start it has to be proven that the DDA program calculates everything correctly, because with any computer program of this complexity coding mistakes are going to happen (and need to be corrected). While the functionality of the generation of the surface geometry can simply be checked by looking at the dipole and surface plots (see chapter 3.2.5), the functionality of the core program (calculating the polarizations and electric fields) is verified by the comparison of several results for Au-spheres both in vacuum [75] and on a substrate [76, 77] with those found in literature.
After that the influence of the parameters, which represent key simplifications of the scattering problem, needs to be thoroughly examined. In the case of the DDA those parameters are the discretization step sizes (representing the assumption of constant fields) and the relative residuum of the GMRES solver (representing the error made because the system of linear equations is not solved exactly). For both parameters there is an ideal choice (0) representing no simplification of the problem, and a trade-off needs to be made in the interest of solving the problem with finite computational power. This trade-off is presented in this chapter and justified using test calculations of spheres (both with/without substrate) and real geometries provided by AFM images.

3.3.1 Verification of the DDA program

The DDA program was verified in two steps. In the first step results from the literature [75], where the accuracies of the DDA, finite elements time domain (FDTD) and the finite elements method (FEM) are compared to Mie Theory, were reproduced. In respective publication excellent agreement was found between Mie Theory and the DDA for the scattering cross section of a 80 nm Au sphere in vacuum. Reproduction of those results verifies that the core DDA program (without the substrate) works properly. Figure 3.20 shows the scattering cross section of an 80 nm (diameter) Au sphere calculated using the present DDA program compared to the results from Mie Theory (calculated using the freely available Matlab script from [78]). There is excellent agreement and thus the core of the DDA program (without substrate) works properly.

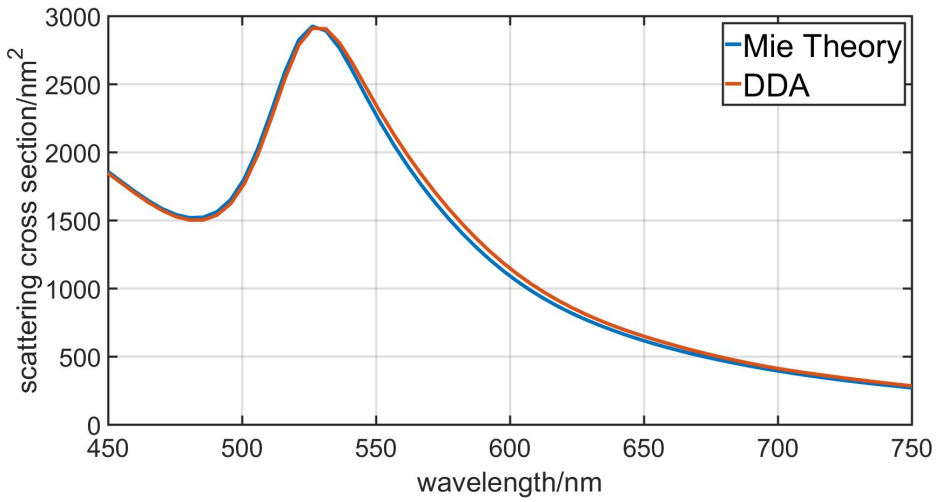

Figure 3.20: Comparison of the result of the DDA program with that from Mie Theory for the scattering cross section of an 80 nm (diameter) Au sphere in vacuum

The second step is the verification of the proper implementation of the substrate. This is particularly important because not only the check of the proper implementation is necessary, but also the investigation if the mirror approximation has a significant influence on the results, which theoretically it should not have for the geometries used in this thesis [73]. The verification is again done by the reproduction of suitable results found in the literature [76, 77]. In this case results from two publications are used, where the accuracies of the DDA-SI toolbox, which uses the analytical approach to the substrate implementation [79], is compared to FDTD [76] and the boundary element method (BEM) [77], respectively. Both publications found good agreement between all methods for the absorption cross section of an Au sphere (diameter 50 nm and discretization step size 1.25 nm) on a glass substrate. Using the DDA-SI toolbox and the MNPBEM toolbox [80], the results have been reproduced and compared to the DDA program form this thesis, using the mirror approximation. Figure 3.21 shows the results, proving good agreement between all methods. The largest difference between the DDA program from this thesis to any reference method is 11 % (at 546.2 nm to the DDA-SI toolbox) and the largest difference between the reference methods themselves is also 11% (at 569.2 nm). Additionally it is important to point out that the mirror approximation is best suited for small scatterers (especially in height) and the 50 nm Au is larger (in height) than any real nanostructure simulated in this thesis.

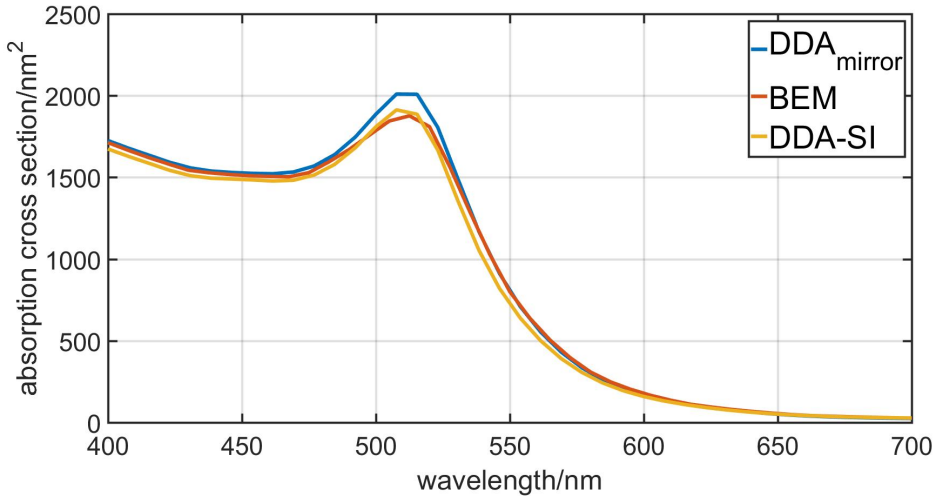

Figure 3.21: Comparison of the gained with the DDA program with those from the MNPBEM toolbox and the DDA-SI toolbox for the adsorption cross section of a 50 nm (diameter) Au sphere in vacuum

3.3.2 Choice of the discretization step size

The choice of the discretization step size is an interesting trade-off between the size of the volume that can be simulated and the accuracy of the simulation. The total number of dipoles is limited by the memory available for the simulation, therefore enlarging the volume in the simulation requires an increase in step size, e.g. doubling the discretization step size will increase the volume by a factor of 8. Therefore the error resulting from simulating only a small part of the substrate has to be carefully balanced with the error resulting from a crude discretization. An additional restriction to the choice of the discretization step size results from the size of the molecule used for the Raman measurements, because the discretization step size has to be at least as small as the thickness of the monolayer formed by the molecules. Combining all of these restrictions the possible range of suitable choices for the discretization step size becomes already very narrow. The monolayer can be represented by 1 dipole layer (discretization step size $\approx$ 0.5 nm; maximum substrate area $\approx$ 200x200 nm), which is the upper limit of the range. Alternatively, the monolayer can be represented by 2 sublayers, with each of them a 1 dipole layer (discretization step size $\approx$ 0.25 nm; maximum substrate area $\approx$ 80x80 nm). The latter is the lower limit of the range as

any area significantly smaller will no longer reliably represents the features found in the AFM images (see chapter 2.2).
A comparison of the results from simulations with step sizes of both 0.25 nm and 0.5 nm and using spheres (both with and without substrate) and a real geometry indicate that it would be highly desirable to use a step size of 0.25 nm, because the error in the calculation of the electric field due to the layer discretization can be at the order of 20 % on real substrate geometries. However, the error resulting from the limited size of the simulation (for 0.5 nm) is also significant (see chapter 4.3). It is at least comparable to that resulting from evaluating the electric field in the first discretization layer even for the 0.5 nm discretization step size. Therefore 0.5 nm is the better choice, because 0.25 nm, whilst a desirable improvement in terms of discretization error, will lead to an overwhelming increase of the error due to the limited substrate area of the simulation, given the computational resources available for this thesis.
The preferred geometry for testing the influence of the discretization step size is a sphere in vacuum, because it has the benefit that an exact solution to the electromagnetic scattering problem is available (Mie Theory; calculated with the Matlab script from [78]). An Au sphere (diameter of 20 nm) was simulated using a discretization step size of 0.25 nm and 0.5 nm respectively. The results for the E^4 approximation of the SERS intensity as a function of distance from the surface are shown in figure 3.22 and compared to the results from Mie Theroy. In the case of a sphere in vacuum the results indicated no significant improvement from the 0.25 nm discretization, as the deviations of all results from the DDA calculations from those calculated by the Mie theory are smaller 5 %.

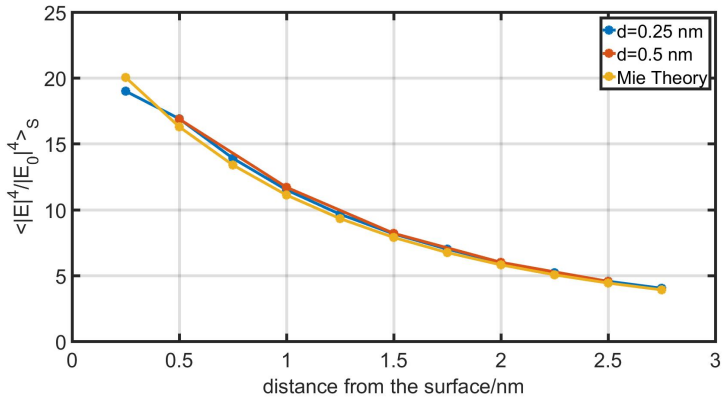

Figure 3.22: Comparison of the E^4 approximation of the SERS intensity from DDA (discretization step size= 0.5 nm; 0.25nm) and Mie Theory as a function of distance from the surface for a 20 nm diameter Au sphere in vacuum

The next step is the inclusion of the substrate in the simulations, and therefore the second geometry for testing the influence of the discretization step size on the accuracy of the results is an Au sphere (20 nm) on a glass substrate. The results for the E^4 approximation of the SERS intensity as a function of distance from the surface are shown in figure 3.23. Again the maximum difference in the results using both a 0.5 nm and a 0.25 nm discretization step size is only about 5 %.

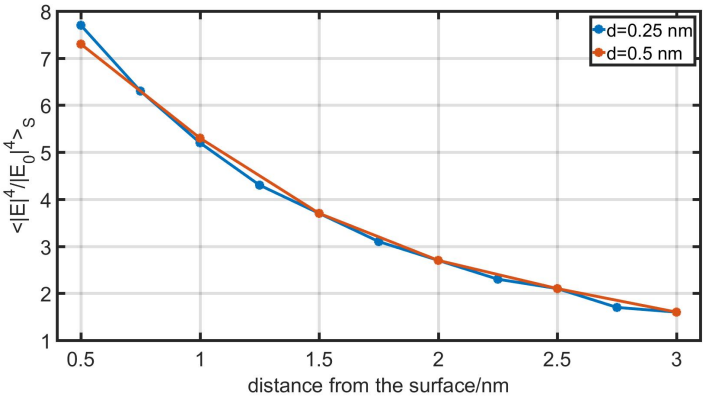

Figure 3.23: Comparison of the E^4 approximation of the SERS intensity (discretization step size= 0.5 nm; 0.25nm) as a function of distance from the surface for a 20 nm diameter sphere on a glass substrate

In the final comparison a real geometry from the AFM images in chapter 2.2 was used. Figure 3.24 shows its real 80x80 nm geometry, both the respective AFM plot and the dipole representation (d=0.5 nm) are shown.

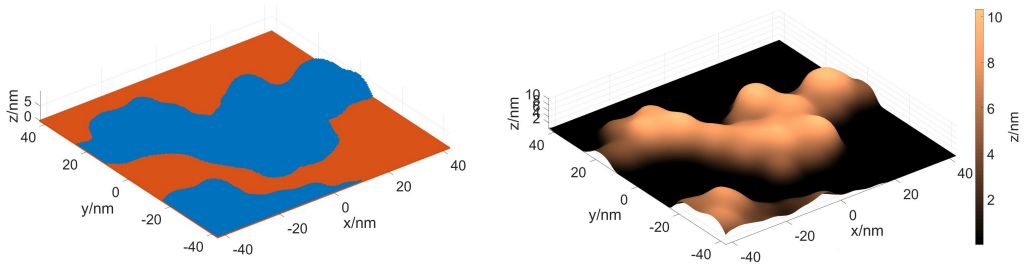

Figure 3.24: Dipole representation (left) and AFM plot (right) of the real geometry used for the test of the discretization step size

The results for the E^4 approximation of the SERS intensity as a function of distance from the surface are shown in figure 3.25. In this case the difference between the results got with a 0.25 nm and the 0.5 nm discretization step size is larger than in the previous cases. The maximum difference is about 20 % at a distance of 0.5 nm from the surface, which is also the critical distance for the molecule used in this thesis. The very large difference at a distance of 0.75 nm from the surface can be attributed to the combination of the rapid decline of the E^4 approximation with distance and the higher sampling rate of the 0.25 nm discretization. A legitimate comparison of the two simulations is only possible at distances were the electric field was calculated in both of them (0.5 nm, 1 nm and 1.5 nm). The error determined from the standard deviation in chapter 4.3 is on the same order of magnitude (discretization step size 0.5 nm; error = 10-20 %), and represents to a first approximation an error in the counting of hot spots in the simulated area. Therefore, 0.5 nm is preferable, because cutting the discretization step size in half reduces the area by a factor of 8 (because the height of the volume is fixed by the height of the nanostructure), and thus can cause a strong increase in the error due to the limited size of the area used in the simulations.

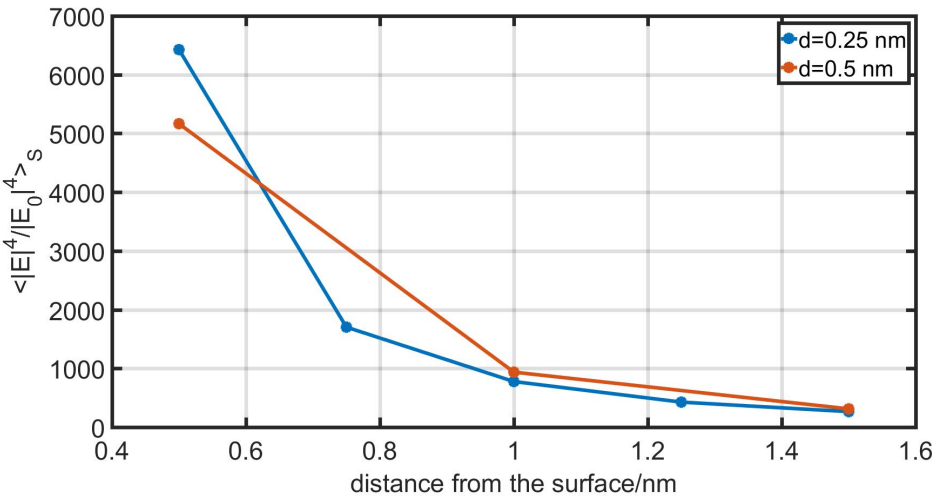

Figure 3.25: Comparison of the E^4 approximation of the SERS intensity (discretization step size= 0.5 nm; 0.25nm) as a function of distance from the surface for the geometry shown in figure 3.24

3.3.3 Choice of the minimal relative residuum

The choice of the minimal relative residuum is much simpler than that of the discretization step size, because it is a simple trade-off between computation time and accuracy of the result calculated by the iterative solver. This means that by simulating a couple of different geometries with a very high degree of accuracy (until the residual is very small) a good estimation of the error as a function of the relative residual can be got. With this estimation a threshold value (10^{-2}) that provides sufficient accuracy (especially compared to accuracies gained from the preceding tests) could be determined. Luckily this threshold value was achievable even for the largest possible geometries (limited by memory) in a reasonable amount of computation time (maximum 1-2 days).
The error as a function of the relative residuum was calculated for 3 geometries: a 50 nm Au sphere in vacuum, a 50 nm Au sphere on a glass substrate and a 100x100 nm area of a real substrate geometry. In all cases the same simulation was performed, starting with a relative residuum of 0.1 and going down (in steps of 10^{-n}) to a relative residuum of 10^{-7} (which was considered as a perfectly converge solution). For the spheres the scattering cross section and the average of the E^4 approximation for the SERS intensity as a function of distance from the surface was analyzed. For the 100x100nm area of a real geometry a full evaluation of eq. 3.41 for the SERS intensity

and eq. 3.39 for the depolarization ratio (see chapter 3.4) is done. In all cases a relative residuum of 10^{-2} was found to be sufficient.
The 50 nm Au sphere in vacuum was simulated with a discretization step size of 1.2 nm and a wavelength of 633 nm for the incident electric field. Figure 3.26 shows the scattering cross section and the E^4 approximation for the SERS intensity (evaluated 1 discretization step above the surface) as a function of the relative residuum. Both plots were normalized to the value got for a relative residuum of 10^{-7}. In both cases the GMRES solver is clearly sufficiently converged at a relative residuum of 10^{-2}.

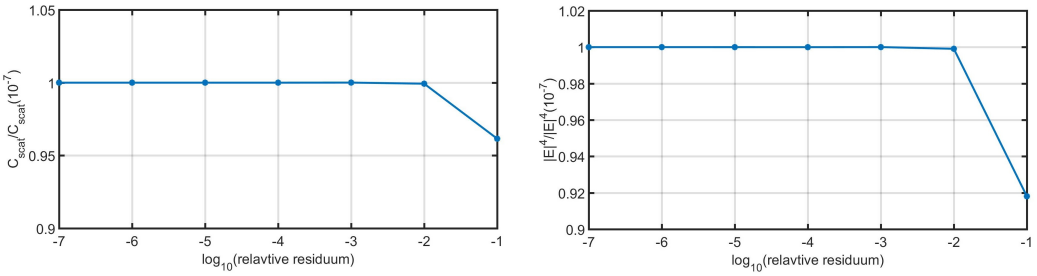

Figure 3.26: Scattering cross section and the E^4 approximation for the SERS intensity as a function of the relative residuum for a 50 nm Au sphere in vacuum

The 50 nm Au sphere on a glass substrate was also simulated with a discretization step size of 1.2 nm and a wavelength of 633 nm for the incident electric field. Figure 3.27 shows the scattering cross section and the E^4 approximation for the SERS intensity (evaluated 1 discretization step above the surface) as a function of the relative residuum, with both plots normalized to the value got for a relative residuum of 10^{-7} and the GMRES solver is clearly sufficiently converged at a relative residuum of 10^{-2}.

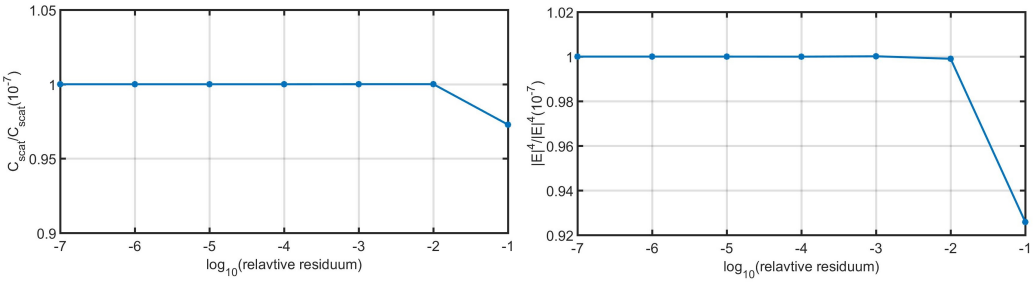

Figure 3.27: Scattering cross section and the E^4 approximation for the SERS intensity as a function of the relative residuum for a 50 nm Au sphere on a glass substrate

Both the dipole representation and the AFM plot for the real 100x100 nm geometry that was used for the residuum test are shown in figure 3.28.

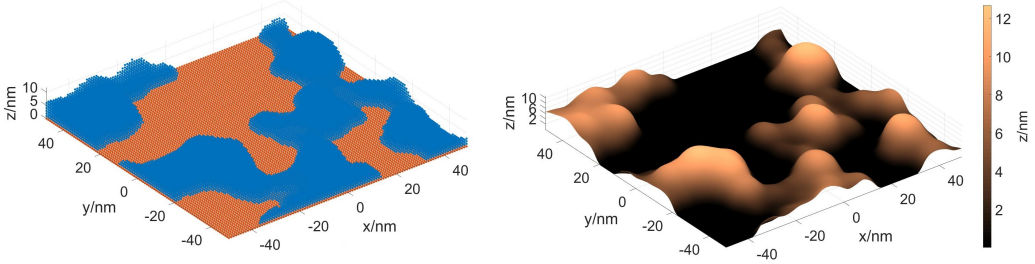

Figure 3.28: Dipole representation (left) and AFM plot (right) of the real geometry used for the relative residuum test

The simulation was carried out with a discretization step size of 1 nm, a wavelength of 633 nm for the incident electric field and a wavelength of 666 nm (equivalent to the 797.1 cm^{-1} band see chapter 3.4) for the Raman band. The total SERS intensity (I_{SERS}) was calculated according to equation 4.1 and the depolarization ratio (ρ_{SERS}) according to equation 3.39 (see chapter 3.4). Apart from the smaller area and lower resolution (chosen to get to very small residuum in a reasonable amount of time) this is completely the same procedure as that used for the calculations for the comparison between experiment and simulation in chapter 4.3. The results are shown in figure 3.29. Again the results were normalized to the values got at a relative residuum of 10^{-7} and the GMRES solver is sufficiently converged at a relative residuum of 10^{-2}.

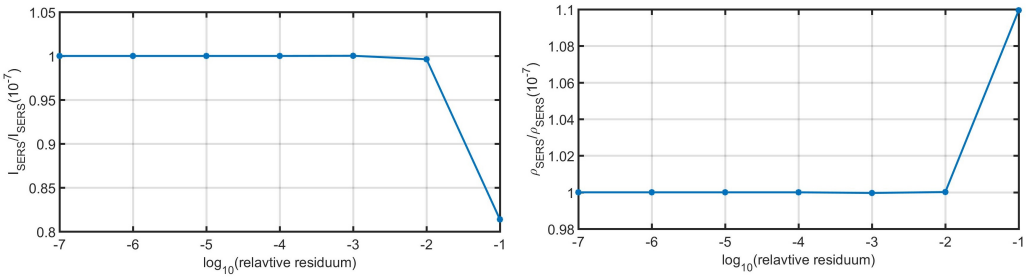

Figure 3.29: Total SERS intensity (left) and depolarization ratio (right) for the geometry in figure 3.28 as a function of the relative residuum.

3.4 Relating electric near-fields to enhancement factors

So far the focus of this chapter has been on the calculation of the electric near-fields, but the ultimate goal is not the calculation of the electric near-fields but that of the enhancement factors (EF) and depolarization ratios (ρ_{SERS}). Additionally, the calculation will be compared to the measurements in chapter 4.3. It is therefore necessary to discuss the correlation between the calculated fields and the measured EFs and ρ_{SERS}. Of particular importance is the elucidation of the main assumptions and restrictions inherent in this comparison. The detailed and rigorous derivation of the basic equation connecting the near-fields to the EF and ρ_{SERS} is not repeated here, as it can be found in the literature [13–15, 32]. The discussion therefore starts with the equation (eq. 3.36 and 3.37) from Le Ru et al. [32], which also includes chemical enhancement and orientation effects of the molecule (in the term α_{SERS}). The explanation of the terms and notation is given in table 3.1.

$$EF_{total} = \frac{\left\langle \left| \vec{E}_{\parallel,\omega_R} \cdot \overline{\overline{\alpha_{SERS}}}(\vec{d}) \cdot \vec{E}_{\omega_L} \right|^2 \right\rangle_S + \left\langle \left| \vec{E}_{\perp,\omega_R} \cdot \overline{\overline{\alpha_{SERS}}}(\vec{d}) \cdot \vec{E}_{\omega_L} \right|^2 \right\rangle_S}{\left| \vec{E}_0 \right|^4 \cdot \left(\left\langle \vec{e}_L \cdot \overline{\overline{\alpha_{Sol}}} \cdot \vec{e}_L \right\rangle_O + \left\langle \vec{e}_\perp \cdot \overline{\overline{\alpha_{Sol}}} \cdot \vec{e}_L \right\rangle_O \right)} \tag{3.36}$$

$$\rho_{SERS} = \frac{\left\langle \left| \vec{E}_{\perp,\omega_R} \cdot \overline{\overline{\alpha_{SERS}}}(\vec{d}) \cdot \vec{E}_{\omega_L} \right|^2 \right\rangle_S}{\left\langle \left| \vec{E}_{\parallel,\omega_R} \cdot \overline{\overline{\alpha_{SERS}}}(\vec{d}) \cdot \vec{E}_{\omega_L} \right|^2 \right\rangle_S} \tag{3.37}$$

Since both the Raman tensor when molecules are adsorbed on the substrate and the orientation of every molecule on the surface are unknown, it is immediately obvious that the term $\alpha_{SERS}(\vec{d})$ is rather unsuitable for the evaluation of eq. 3.36. and eq. 3.37. One possibility to deal with it would be to make assumptions, perhaps backed up by DFT calculations, about the symmetry and magnitude of the Raman tensor as well as the orientation of the molecule. However, this would introduce great uncertainty into the calculation, which is unnecessary in the present case, as the purpose is the determination of the accuracy of the approach presented in chapter 3.1 & 3.2, for the calculation of the electromagnetic EFs. With this in

Table 3.1: Explanation of the Terms and Notations in Equations x and y

EF_{total}	average EF as measured
ρ_{SERS}	depolarization ratio as measured
$\vec{E}_{\omega_L}$	electric field at a position on the substrate with an incident electric field at the laser wavelength (ω_L)
$\vec{E}_{\parallel,\omega_R}$ ($\vec{E}_{\perp,\omega_R}$)	electric field at a position on the substrate with an incident electric field at the wavelength of the Raman band (ω_R) and with polarization parallel (perpendicular) to the polarization of the laser
$\vec{E}_0$	electric field of the laser in the reference solution
$\vec{e}_L$	unit vector of $\vec{E}_0$
$\vec{e}_\perp$	unit vector perpendicular to $\vec{e}_L$
$\overline{\overline{\alpha_{Sol}}}$	Raman tensor in the reference solution
$\overline{\overline{\alpha_{SERS}}}(\vec{d})$	Raman tensor when adsorbed on the substrate (with orientation $\vec{d}$)
$\langle ... \rangle_S$	average over a significant surface area of the substrate and all possible orientations $\vec{d}$ of the adsorbed molecule
$\langle ... \rangle_O$	average over all orientations of the molecule

mind a good way to deal with $\alpha_{SERS}(\vec{d})$ is to restrict the comparison of the simulation and measurement to isotropic Raman bands. This assumption can be checked by a simple measurement, because the Raman tensor of an isotropic band has a depolarization ratio of 0 in solution [32]. There are 3 bands of 4-MBT that have an isotropic tensor (797.1, 1078.2 and 1210.0 cm^{-1}; see chapter 4.1). With the assumption of an isotropic tensor the eqs. 3.36 and 3.37 simplify significantly (see eqs. 3.38-3.40). As an additional benefit in case of an isotropic tensor an evaluable equation for the relative intensities between substrates can be derived (see eq.3.40).

$$EF_{total} = \frac{\alpha_{SERS}}{\alpha_{Sol}} \cdot \frac{\left\langle \left| \vec{E}_{\parallel,\omega_R} \cdot \vec{E}_{\omega_L} \right|^2 \right\rangle_S + \left\langle \left| \vec{E}_{\perp,\omega_R} \cdot \vec{E}_{\omega_L} \right|^2 \right\rangle_S}{\left| \vec{E}_0 \right|^4} \tag{3.38}$$

$$\rho_{SERS} = \frac{\left\langle \left| \vec{E}_{\perp,\omega_R} \cdot \vec{E}_{\omega_L} \right|^2 \right\rangle_S}{\left\langle \left| \vec{E}_{\parallel,\omega_R} \cdot \vec{E}_{\omega_L} \right|^2 \right\rangle_S} \tag{3.39}$$

$$\frac{I_{S1}}{I_{S2}} = \frac{\left\langle \left| \vec{E}_{\parallel,\omega_R} \cdot \vec{E}_{\omega_L} \right|^2 \right\rangle_{S1} + \left\langle \left| \vec{E}_{\perp,\omega_R} \cdot \vec{E}_{\omega_L} \right|^2 \right\rangle_{S1}}{\left\langle \left| \vec{E}_{\parallel,\omega_R} \cdot \vec{E}_{\omega_L} \right|^2 \right\rangle_{S2} + \left\langle \left| \vec{E}_{\perp,\omega_R} \cdot \vec{E}_{\omega_L} \right|^2 \right\rangle_{S2}} \tag{3.40}$$

The depolarization ratios and relative intensities between different substrates can already be calculated using eq.3.39 and 3.40, but in order to calculate the total EFs the ratio $\alpha_{SERS}/\alpha_{Sol}$, often referred to as chemical enhancement in the literature [32], still needs to be addressed. Therefore either a value for the chemical enhancement must be assumed (again perhaps back by DFT simulations), or more to the point of this thesis the comparison for the total EFs must be restricted to Raman bands without chemical enhancement. This is equivalent to the assumption that the magnitude of the Raman tensor does not change, if the molecule binds to the metal ($\alpha_{SERS} \approx \alpha_{Sol}$). A check of this assumption is provided by the Raman shift in spectra measured both on the SERS substrate and in solution, as a difference in the Raman shift implies changes in the vibrational mode and thus the Raman tensor. Therefore, in addition to $\rho_{sol} \approx 0$ also $\Delta\nu \approx 0$ is required for a reasonable comparison of the measured and simulated total EFs. The only band that fulfills both conditions is the 797.1 cm^{-1} band (see chapter 4.1). With this additional assumption eq. 3.38 simplifies to eq. 3.41.

$$EF_{total} = \frac{\left\langle \left| \vec{E}_{\parallel,\omega_R} \cdot \vec{E}_{\omega_L} \right|^2 \right\rangle_{S} + \left\langle \left| \vec{E}_{\perp,\omega_R} \cdot \vec{E}_{\omega_L} \right|^2 \right\rangle_{S}}{\left| \vec{E}_0 \right|^4} \tag{3.41}$$

Although further simplifications are common in the literature [81–83], eq.3.41 is used in this work, because it is the equation that descripts the total EF purely in terms of electric fields relying on the least number of assumptions. The additional assumption that is often made is the insignificance of the perpendicular polarization ($\left\langle \left| \vec{E}_{\parallel,\omega_R} \cdot \vec{E}_{\omega_L} \right|^2 \right\rangle_S >> \left\langle \left| \vec{E}_{\perp,\omega_R} \cdot \vec{E}_{\omega_L} \right|^2 \right\rangle_S$). Note that this implies $\rho_{SERS} \approx 0$, which is clearly not the case for the substrates used in this thesis (see chapter 4.1). Also the dependence of the electric near-field on the wavelength of the Raman band is often assumed to be small ($\vec{E}_{\parallel,\omega_R} \approx \vec{E}_{\omega_L}$). Note that applying these two assumptions to eq.3.41 leads to the most commonly used expression for the SERS EFs, the

E^4 approximation (see eq. 3.42).

$$EF_{total} = \frac{\left\langle \left| \vec{E}_{\omega_L} \right|^4 \right\rangle_S}{\left| \vec{E}_0 \right|^4} \tag{3.42}$$

With the equations for the calculation of ρ_{SERS} and the EFs derived, another important point needs to be addressed. From eq. 3.39-3.41 it is apparent that at least 3 simulations are necessary to evaluate those equations on a given position on the substrate. This is the case because the enhancements of both the incident field and for both polarizations of the outgoing field needs to be considered. However, doing 3 simulations enables only the evaluation of the equations for a given polarization of the incident field. Since the polarization of the laser relative to the nanostructures is not known during the measurement, 4 simulations per substrate position are used in this thesis for the simulation of a random laser polarization. This is accomplished as illustrated in figure 3.30.

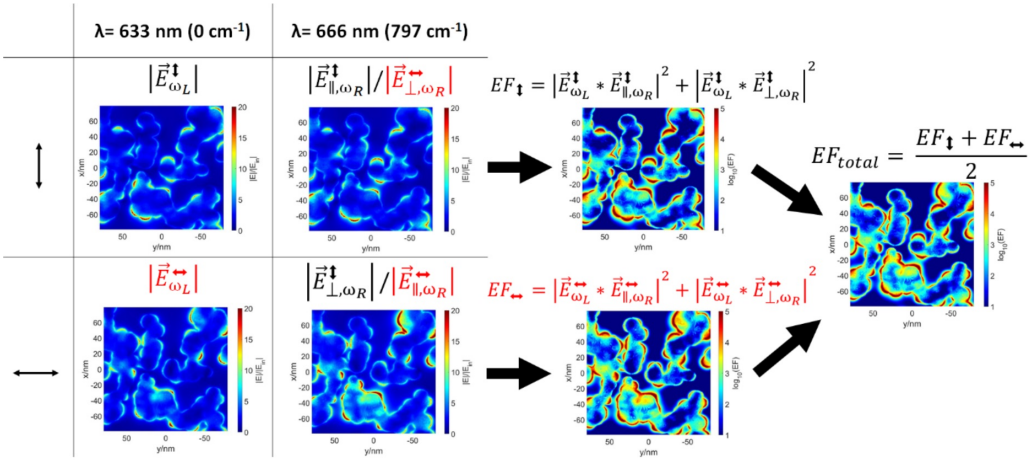

Figure 3.30: Illustration of the use of 4 simulations for the evaluation of eq. 3.39-3.41 in case of a random polarization of the incident field

3.5 Summary

At this point the entire procedure of calculating the enhancement factors and depolarization ratios presented in chapter 4.2 & 4.3 has been discussed. The starting point is the basic input from the measurements, most importantly the AFM measurements from chapter 2.2, and the fundamental integral equation for the electric fields for the electromagnetic scattering problem.
From there it is necessary to discretizes the electric field in order to turn the fundamental integral equations into a solvable system of linear equations. This results in two key parameters that describe these key simplifications within the framework of the DDA, the discretization step size and the relative residuum. Both of these parameters would ideally be zero, but in order to solve the problem with finite computational resources need to be chosen very carefully. Using several test simulations it is shown that a relative residuum of 10^{-2} is sufficient and can reasonably be accomplished with the available computational power. For the discretization step size a compromise between the error due to a crude discretization versus the error due to the limited volume simulated is necessary. The best compromise (together with the restrictions due to the size of the molecule) is found to be a discretization step size of 0.5 nm.
In addition to the discretization of the electric field, it is necessary to determine the polarizability from the dielectric constant and include the substrate in the simulation. The polarizabilities have been determined using the IT approach, which includes no additional simplifications of the problem. This approach has also been extended to a sufficiently large number of off-diagonal elements of the Green's tensor in order to maintain the full benefit of the IT approach at little computational cost. The substrate has been include in the simulation using the image approximation, which only works for small scatterer. However, it has been shown that the image approximation is sufficient for the geometries studied in this work by comparison to other methods, which use the analytical "Sommerfeld integrals" approach.
Another issue that has been addressed is how the simulated geometry is generated from the AFM images. This is done by first applying several filters to the AFM image (flatting filters; scar removal and median filters), in order to create an AFM image where the substrate is perfectly flat and at a z=0 nm. The height information of the AFM image can then be used to generate the simulated geometry by creating a test grid that encompasses the entire AFM image and putting at dipole at every position on the grid that is above z=0 nm and below the height of the features in the AFM image.

Finally, the connection between the simulated electric fields and the SERS enhancement has been addressed. Here the most important points are that the predictions need to be restricted to isotropic Raman bands in order to avoid additional assumptions about the orientation of the molecule and the symmetries of the Raman tensor. Also if absolute enhancement factors rather than relative enhancement factors or depolarization ratios are to be calculated, the calculation has to be restricted to bands with no chemical enhancement ($\Delta\nu \approx 0$). Additionally, for every Raman band four simulations (two wavelengths x two polarizations) are necessary to appropriately calculated the enhancement factors and depolarization ratios.

Chapter 4

Results and Discussion

With the discussion of both the experimental (chapter 2) and the theoretical work/simulations (chapter 3) finished this chapter now focuses on the results achieved. The main experimental results are summarized in chapter 4.1, whereas those from the simulations can be found in chapter 4.2.1. In addition, more detailed results of the simulations including outlines of possible further applications of the proposed simulation approach are summarized in chapter 4.2.2. Finally, a comparison between the results from both the experiments and simulations is drawn in chapter 4.3, which is also used to indicate possible future improvements as well as fundamental limits of the simulations. At this point it is important to note that most of the results presented in this chapter have already been published in the article "Accurate Near-Field Simulations of the Real Substrate Geometry – A Powerful Tool for Understanding Surface-Enhanced Raman Spectroscopy" in the Journal of Physical Chemistry C [84]. Chapters and subchapters that mostly present already published data will therefore be marked with a quotation in the title.

4.1 Measured enhancement factors and depolarization ratios [84]

The manufacturing process described in chapter 2.1 allows easily the fabrication of batches with a large number of samples. The variation of the SERS-signal measured on various samples of the same batch has been shown to be around 20 %, which is comparable to the variation of the SERS-signal across a single substrate. Since the variation between different batches was greater due to variations in the mean thickness and roughness of the Au film, two batches of 8 samples each were manufactured for the comparison between measurements and simulations. From these batches the necessary spectra and corresponding references were measured as detailed in chapter 2.3, and the average spectrum per batch was used to determine the enhancement factor per batch. Figure 4.1 shows the averaged spectrum of batch 1, batch 2 and the reference measurement of a 0.5 M solution of 4-MBT in ethanol (see chapter 2.3).

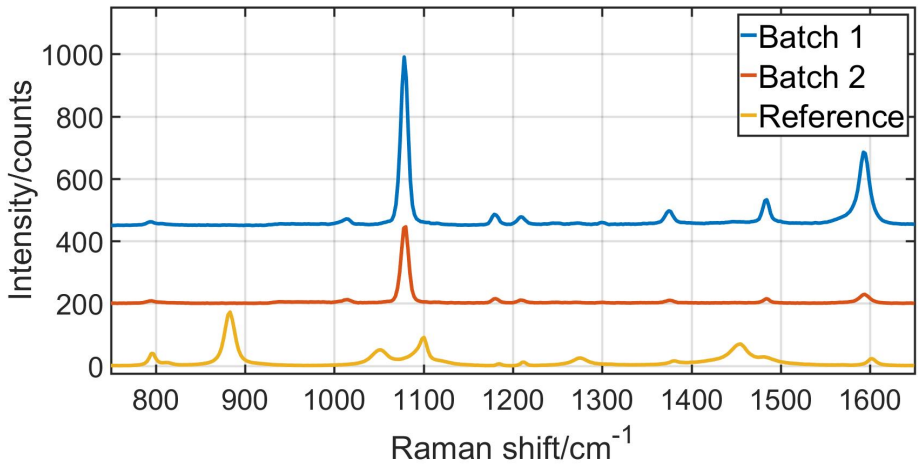

Figure 4.1: Averaged spectrum of batch 1, batch 2 and the reference measurement (0.5 M solution of 4-MBT in ethanol)

In addition to the enhancement factors several other parameters that are relevant to the comparison of measurement and simulation have been determined. These parameters will now be briefly discussed in order to prove their relevance (a detailed discussion of the measurements and relevance can be found in chapters 2.3 and 3.4). The final results are summarized in table 4.1.

The Raman shift on the SERS substrate (ν_{SERS}) is relevant mostly in correlation with the Raman shift in solution (ν_{Sol}). On the one hand it is obviously a central parameter in Raman spectroscopy in general used to assign vibrational modes and simply identify bands (as in the 1080 cm^{-1} band). On the other hand in this work in particular the knowledge of the difference between the Raman shift in solution and the Raman shift on the SERS substrate ($\Delta\nu$) is important, because the difference in shift has to be close to zero to justify the assumption that the vibrational mode is not effected by the adsorption on the substrate and thus chemical enhancement is negligible. The depolarization ratio in solution (ρ_{Sol}) is relevant, because an isotropic tensor is assumed for the comparison of simulation and experiment, which requires that the depolarization ratio in solution is close to zero. Finally, the depolarization ratio on the SERS substrate (ρ_{SERS}) is central to the comparison of simulation and experiment, as it has been shown to be both an easily to determine and more robust parameter both from an experimental (see chapter 2.3.4) and theoretical (see chapter 3.4) point of view. The band assignments are taken over from literature [30, 43, 44]. Additionally, it is important to take notice that the band at 1483.1 cm^{-1} is not included in the table, as it is not measurable in any reference solution or on the solid reference of 4-MBT and thus seems to be specific to the molecule adsorbed on the SERS substrate. It is also interesting to note that, independent of the vibrational mode, all depolarization ratios on the SERS substrate have a value around 0.56. This points perhaps to a depolarization ratio that is driven mainly by the symmetry of the substrate (see chapter 4.2.2).

Table 4.1: Depolarization Ratios and Enhancement Factors (EF) of 4-MBT on Batch 1 and Batch 2.

ν_{SERS}/cm^{-1}	ν_{Sol}/cm^{-1}	$\Delta\nu/cm^{-1}$	ρ_{Sol}	$EF(x10^3)$		ρ_{SERS}		Assign
				Batch 1	Batch 2	Batch 1	Batch 2	
797.1	796.9	0.2	0.04	6.9	5.5	0.58	0.57	$\beta(CCC) + \nu(aryl - CH_3)$
1078.2	1100.9	-22.7	0.07	250	140	0.57	0.56	$\beta(CCC) + \nu(CS)$
1180.4	1184.6	-4.2	0.17	180	94	0.57	0.56	$\beta(CH)$
1210.0	1212.2	-2.2	0.06	61	26	0.55	0.54	$\nu(aryl-C)$
1374.8	1381.1	-6.3	0.45	89	22	0.58	0.53	$\beta(CH)$
1591.8	1602.5	-10.7	0.75	260	39	0.55	0.53	$\nu(CC)$

4.2 Simulation results

The presentation of the results gained from the simulations is segmented into two chapters. The first chapter (chapter 4.2.1) deals with the overall results of the simulations of the enhancement factors which were already published in [84]. The second chapter (chapter 4.2.2) is using the same core simulation procedure with regard to the underlying electric fields, but with different evaluations of these fields (see chapter 3.4) with regard to the calculation of polarization dependent fields and the origin of the depolarization ratios.

4.2.1 Main results [84]

All of the simulations were performed using the AFM images shown in figure 2.14 for batch 1 and figure 2.15 for batch 2 (see chapter 2.2). In addition, 4 simulations per position on the AFM image were necessary (as describe), and 4 positions per AFM image were simulated, as is clearly visible in figure 4.2. For each position the original dimensions (before the cropping of the boundaries; see chapter 3.2.5) were 200x200 nm with a discretization step size of 0.5 nm. The basic minimal requirements and parameter choices outlined in chapter 3.3.2 and 3.3.3 were used. As brief summary , the dielectric constant of Au from [85] was used for the dipoles, the dielectric constant of SiO_2 from [74] was used for the substrate (because of the thick oxide layer on the Si-wafer, see chapter 3.2.4), and the incident field was approximated by a plane wave. All calculations have been done using the values of the electric fields at 1 discretization step above the surface. The local enhancement factors shown in figure 4.2 and 4.3 were calculated as outlined in figure 3.30 (chapter 3.4). It is important to note that with the computing power available (see appendix A.4.5) the calculation of one band took about 1-2 days (depending on the convergence of the simulations). This implies that the calculation per AFM image and Raman band (16 simulations) took approximately 3 weeks for the first Raman band and 1.5 weeks for any other Raman band (the 8 simulations at the incident wavelength can be reused). Therefore, two Raman bands were chosen for the simulations. Firstly the 797.1 cm^{-1} band, because it fulfills the two requirements ($\rho_{Sol} \approx 0$ and $\Delta\nu \approx 0$), thus it can be expected to perform well in both the comparison of the enhancement factors and the depolarization ratios with the experimental findings. The other band chosen was the band at 1078.2 cm^{-1}, because it is the strongest band that fulfills the central requirement $\rho_{Sol} \approx 0$, thus it could be expected to perform well with regard to the calculation of the depolarization ratios. However, the strongly shifted position of the band in the SERS spectra ($\Delta\nu = -22.7cm^{-1}$)

can entail a great influence of chemical enhancement on the strength of the enhancement factor. The results for the local enhancement factors of batch 1 and batch 2 are shown in figure 4.2 (797.1 cm^{-1} band) and figure 4.3 (1078.2 cm^{-1} band).

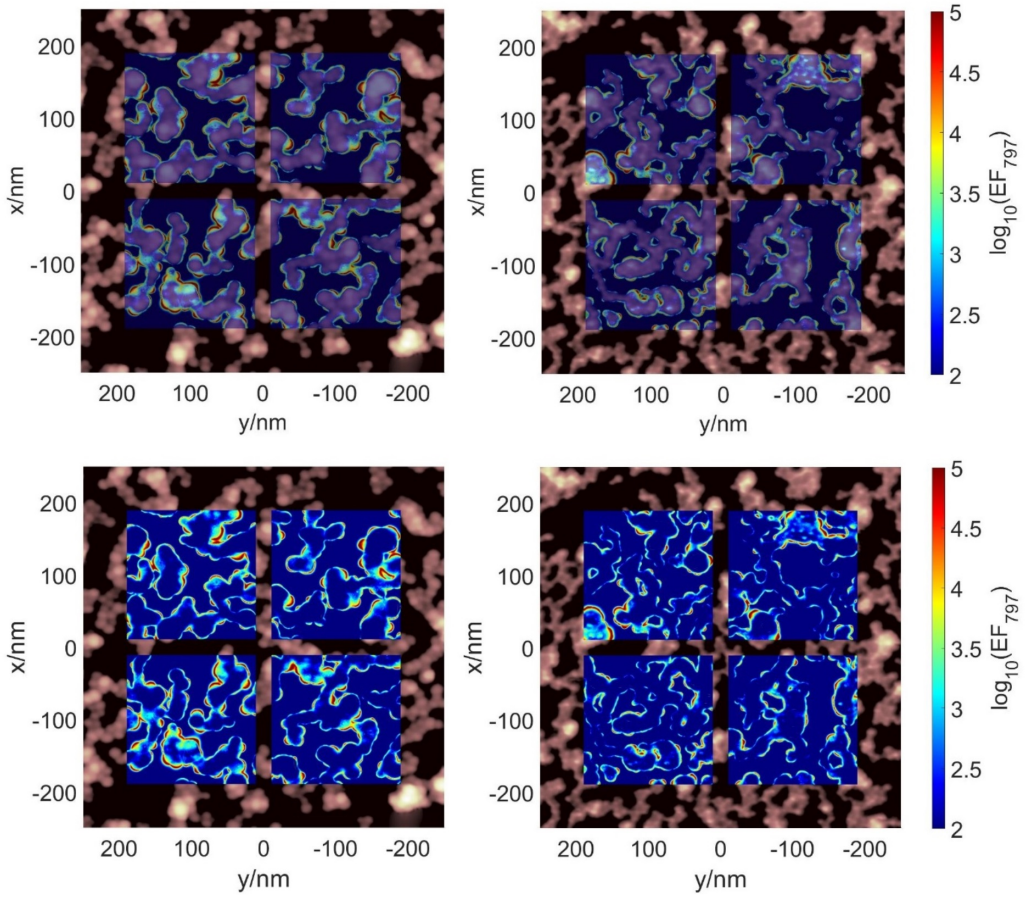

Figure 4.2: Calculated local enhancement factor for the 797.1 cm^{-1} band for batch 1 (left) and batch 2 (right). The simulation results are shown both transparent to show the correlation with the AFM image (top) and opaque for better visualization of the hot spots (bottom)

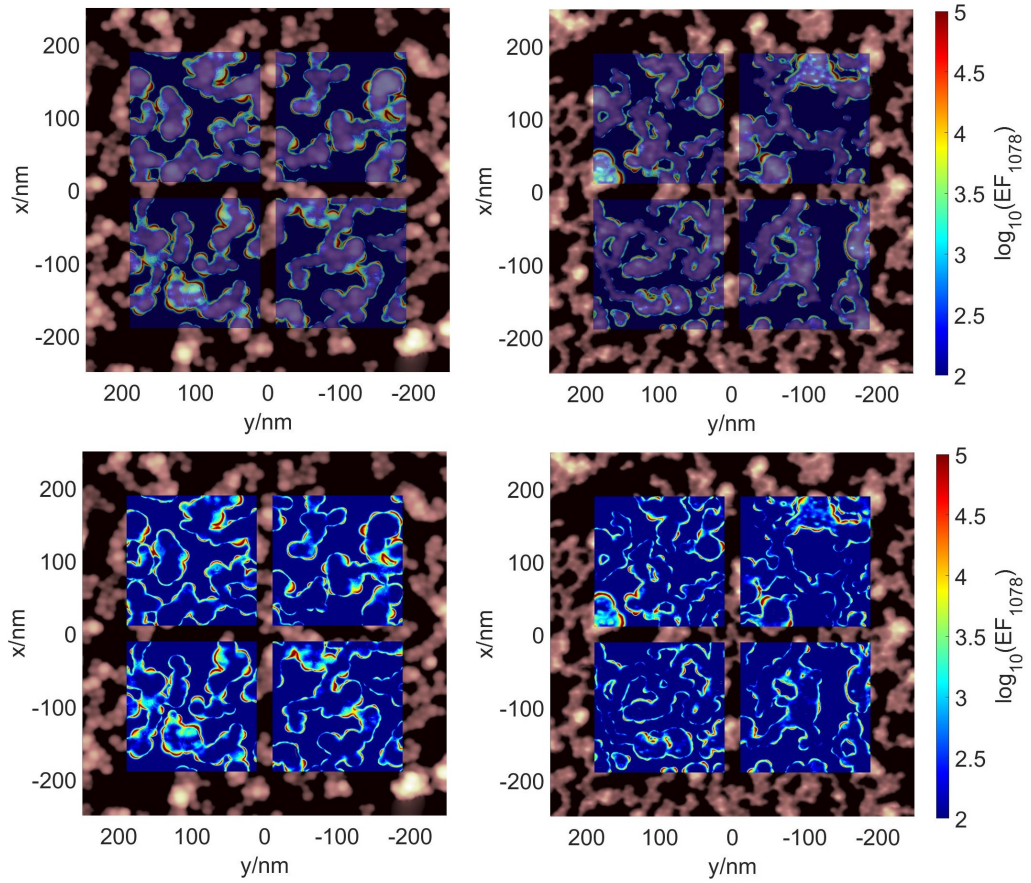

Figure 4.3: Calculated local enhancement factor for the 1078.2 cm^{-1} band for batch 1 (left) and batch 2 (right). The simulation results are shown both transparent to show the correlation with the AFM image (top) and opaque for better visualization of the hot spots (bottom)

First and foremost, it is important to notice that the simulation results for both bands are very similar (they seem almost identical), and that also the enhancement factors match very well (see table 4.2, chapter 4.3). This is not surprising, as the difference in the wavelength between the 797.1 cm^{-1} band (666 nm) and the 1078.2 cm^{-1} (679 nm) is rather small. Since the only difference between the simulations of different bands is the wavelength used in two of the four simulations done per area (see chapter 3.4), the nearly identical wavelengths of the two bands lead to similar simulations results. But the results would differ if the substrate had some strong and sharp plasmonic resonant peak near one of the wavelengths, which is not expected on irregular, sputtered substrates.

Additionally, interestingly the largest local enhancement factors predicted by the simulations are on the order of magnitude of 10^7, which is several orders of magnitude higher than the predicted average enhancement of the order of 10^3-10^4. Also the bulk of the enhancement (approximately 90 %) is concentrated on hot spots with local enhancement factors of 10^5 or higher. These are the red regions in the figures 4.2 and 4.3, and it is in line with the theory that for most SERS substrates a small number of molecules at hot spots are responsible for the bigger part of the signal.
While the results from figures 4.2 and 4.3 were used for the calculation of the average enhancement factors in table 4.2 (chapter 4.3), the calculation and origin of the depolarization ratios is discussed in detail in chapter 4.2.2.

4.2.2 Detailed results (depolarization ratios)

The discussion of the depolarization ratios will be limited to the results gained from the 797.1 cm^{-1} band, as the results for the 1078.2 cm^{-1} band are virtually identical. Furthermore, the detailed discussion will focus on batch 1, as the results are qualitatively the same for both batches. For the sake of completeness the results of batch 2 are shown in the figures 4.6 and 4.7 at the end of this chapter.
Since the denominator (enumerator) in the depolarization ratio is the result of the products of fields with parallel (perpendicular) polarizations, looking at the field strength as a function of the polarization is a good starting point. Figure 4.4 shows the field strength in the nearfield (batch 1) at both the laser-wavelength (top) and the band-wavelength (bottom) for the two perpendicular polarizations. Please note that the results of two perpendicular polarizations are sufficient to calculate every possible polarization with the same wave vector.

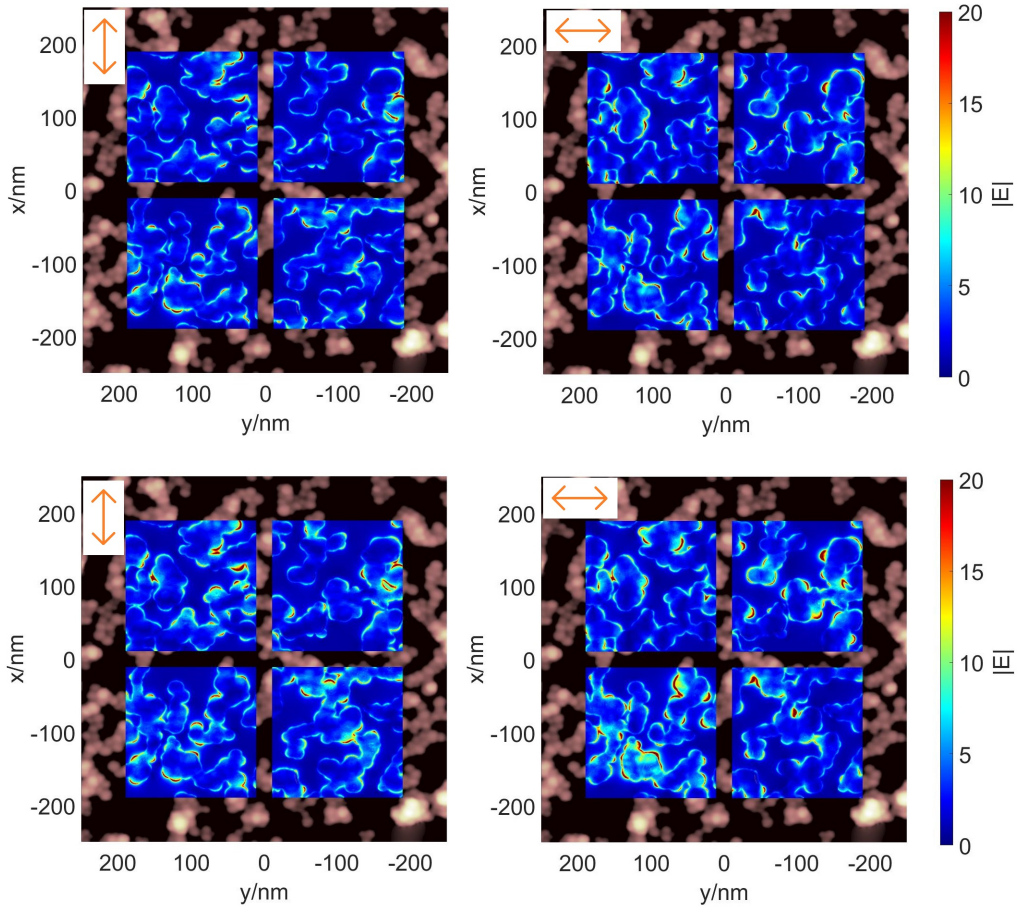

Figure 4.4: Strength of the nearfield at the laser-wavelength (top) and the band-wavelength (bottom) for batch 1. The polarization of the incident field is as indicated in the top left corner

As one would expect, the hot spot positions are mostly dependent on the polarization and are usually located at edges that are oriented perpendicular to the polarization. Interestingly, there is virtually no dependence of the hot spot positions on the wavelength. The intensity of the hot spots increases from the laser-wavelength to the band-wavelength, but their positions are practically identical. At this point it is important to note that in this cases the depolarization ratio can essentially be regarded as the difference in overlap between different polarizations. It is perhaps best to explicitly state the equations (see chapter 3.4) for the enhancement of the parallel and perpendicular components (with regards to the laser polarization) of the SERS signal:

$$EF_{\parallel} = \left|\vec{E}_{\leftrightarrow,0} \cdot \vec{E}_{\leftrightarrow,797}\right|^2 + \left|\vec{E}_{\updownarrow,0} \cdot \vec{E}_{\updownarrow,797}\right|^2 \tag{4.1}$$

$$EF_{\perp} = \left|\vec{E}_{\updownarrow,0} \cdot \vec{E}_{\leftrightarrow,797}\right|^2 + \left|\vec{E}_{\leftrightarrow,0} \cdot \vec{E}_{\updownarrow,797}\right|^2 \tag{4.2}$$

$$\rho_{SERS} = \frac{EF_{\perp}}{EF_{\parallel}} \tag{4.3}$$

with $EF_{\parallel}$ the enhancement of the parallel component, $EF_{\perp}$ the enhancement of the perpendicular component, $E_{x,y}$ the electric field with the specified polarization and at the corresponding wavelength (laser or band) and ρ_{SERS} the depolarization ratio.
It is immediately obvious that the difference between the products in equations 4.1 and 4.2 has to be due to the overlap of hot spots with different polarizations, as exactly the same fields are multiplied and added up in both equations, just their arrangement is different. Since the hot spot positions are mostly dependent on the polarization (not the wavelength), the products in the term for the parallel component will always have a near perfect overlap. However, this is not true for the terms for the perpendicular component, where the hot spot positions will in general be different due to the different polarizations of the fields in the product. This further implies that the hot spots for the parallel component will be the same as those seen in the field strengths in figure 4.4 or the total enhancement in figure 4.2, whereas the same is not necessarily true for the perpendicular component. Two extreme cases can be imagined for the local origins of the perpendicular component: a “diffuse” situation where the distribution resembles that of the parallel component, but is weaker due to the mismatch of the hot spots from different polarizations; or a “localized” situation, where the perpendicular component largely originates from a couple of hot spots with a very good overlap in both polarizations and thus the hot spots are highly localized. Figure 4.5 shows the local origins of the parallel and perpendicular component (on batch 1), both calculated according to the equations 4.1 and 4.2.

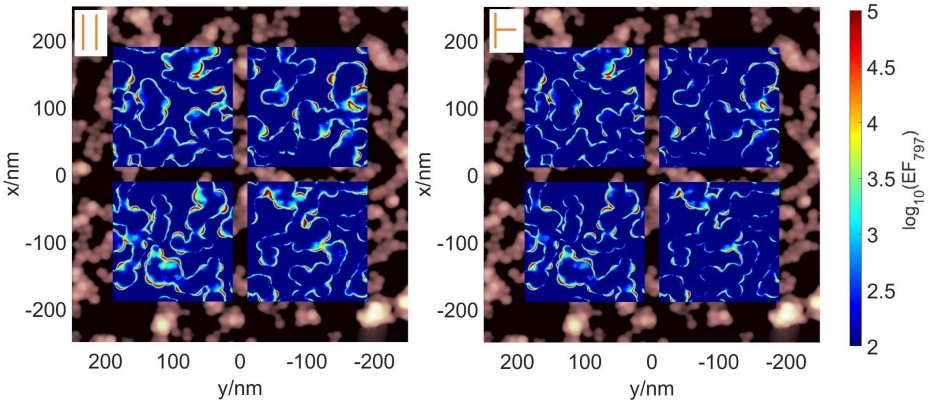

Figure 4.5: Local enhancement for the parallel (left) and perpendicular (right) component of the SERS signal on batch 1

Despite the fact that a handful of particularly strong hot spots can be recognized in the distribution of the perpendicular component, for the most part the local enhancement resembles (only weaker) the parallel component. Therefore, the substrates (of batch 1) are rather close to the "diffuse" situation described above. From intuition, one would also guess that a highly random substrate would create a "diffuse" situation rather than a highly regular one. The situation for batch 2 is similar and summarized in the figures 4.5 and 4.6. Note, that the average values of the depolarization ratios in table 4.2 (chapter 4.3) are calculated from the results in the figures 4.5 and 4.7 respectively.

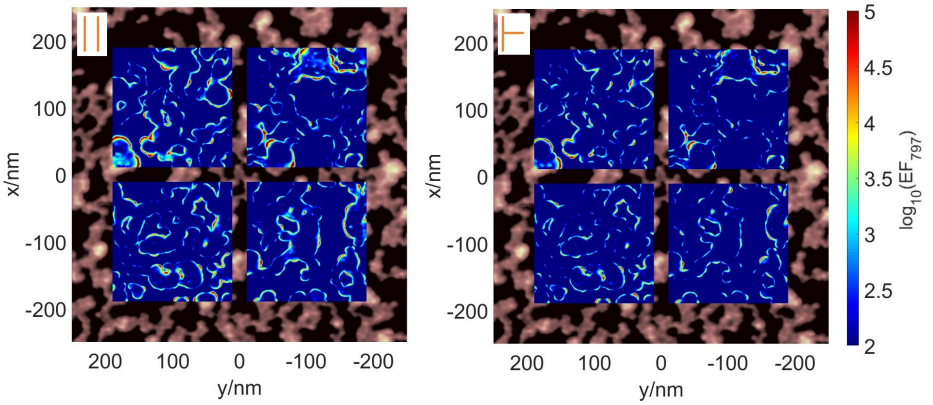

Figure 4.6: Local enhancement for the parallel (left) and perpendicular (right) component of the SERS signal on batch 2

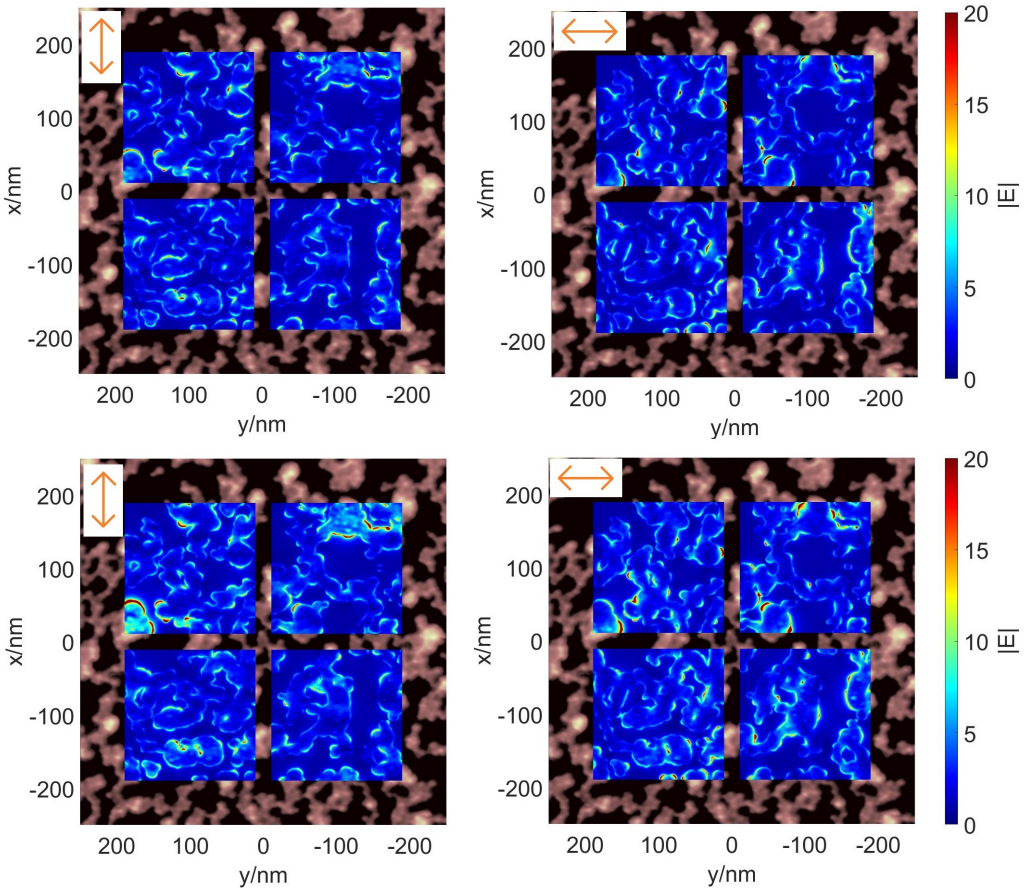

Figure 4.7: Strength of the nearfield at the laser-wavelength (top) and the band-wavelength (bottom) for batch 2. The polarization of the incident field is as indicated in the top left corner

4.3 Simulations vs Measurement [84]

This chapter deals with the comparison of the simulated and measured results. This should also provide some clue how well the mapping of the substrate structure by AFM and the implementation of this structure in the simulation procedure worked. The results of both the measurements and simulations are summarized in table 4.2. In addition to the depolarization ratios and the enhancement factors the ratio of the intensity between the two batches is also given, as it represents an intermediate stage both in theoretical and experimental difficulty compared to the other two quantities (see chapter 3.4).

Table 4.2: Depolarization Ratios and Enhancement Factors (EF) of 4-MBT on Batch 1 and Batch 2.

		$797.1cm^{-1}$		$1078.2cm^{-1}$	
		ρ_{SERS}	$EF(x10^3)$	ρ_{SERS}	$EF(x10^3)$
Batch 1	calc	0.49 ± 0.13	11.8 ± 1.2	0.52 ± 0.14	10.5 ± 0.9
	meas	0.58 ± 0.04	6.9 ± 1.1	0.57 ± 0.01	250 ± 50
Batch 2	calc	0.49 ± 0.16	6.3 ± 1	0.55 ± 0.19	6.3 ± 1
	meas	0.57 ± 0.03	5.5 ± 0.7	0.56 ± 0.01	140 ± 20
$\frac{Batch1}{Batch2}$	calc	1.9 ± 0.5		1.7 ± 0.4	
	meas	1.3 ± 0.4		1.8 ± 0.6	

Concerning the measurements, the error estimates provided in the table represent merely the standard deviation of the respective quantity between substrates of the same batch (see chapter 2.3.3 for more details), whereas with regard to the simulations the standard deviation between the 4 simulated areas per batch are given. Additional systemic sources of error have been discussed throughout this work, and they will be briefly summed up here for the convenience of the reader.
With regard to the experiments, all the parameters that are used in the calculation of the EH (see eq. 2.5 in chapter 2.3) are of course potential error sources. Some of these, like the ratio between the surface area of the nanostructure and the projected area, the effective height of the scattering volume or the concentration of the reference solution, can be determined quite accurately and probably do not represent a significant problem. However, especially the parameters concerning the SAM are problematic. The surface density of 4-MBT has to be taken at face value from the literature [33] (as has the orientation of the molecule [39]). The measurements

and calculations done to determine these quantities are usually specific to a certain crystal orientation of Au (Au(111)) in the case of [39]) and were performed on highly regular substrates. Thus, the assumption that these values hold on rough sputtered nanoislands is questionable, but no better alternative was available. In addition, a perfect monolayer coverage is implicitly assumed in eq 2.5 (chapter 2.3). However, the significant worsening of the reproducibility of the SERS signal (see chapter 2.1.2) when changing from spin coating with methylene blue to the 4-MBT monolayer suggests that there are problems with achieving good coverage every time.
Whereas the measured enhancement factors are subject to all potential error sources mentioned above, the same cannot be said for the depolarization ratios. Since depolarization ratios are measured as the intensity ratio of two spectra (to a good approximation) measured of the same molecules on the surface, the quality and homogeneity of the SAM should not affect them too much. The intensity ratios between batches fall in between these two extremes, as on one hand all parameter related errors will cancel out in the ratio, but on the other hand a different monolayer coverage between batches is still possible.
With regard to the simulations, apart from trivial concerns regarding the overall numerical accuracy of the DDA algorithm, that have been assessed in chapter 3.3, and the accuracy of the AFM measurements (see chapter 2.2), additional potential error sources connected to the theoretical background of the calculations can have an impact on the results. The dielectric influence of the 4-MBT monolayer itself is not included in the simulations. Also, the variation of the dielectric function close to the surface [86] (due to quantum mechanics) was ignored. Again, these factors will more strongly effect the enhancement factors then the depolarization ratios. Concerning the enhancement factors, any error in the field strength is amplified by their approximated 4^{th} power dependence on the electric fields. On the contrary, the depolarization ratios have effectively only a ratio of two 2^{nd} power quantities (see eq.3.39 chapter 3.4), and since it is a ratio the errors could even cancel out further. The relative intensities between batches again fall in between, as they are calculated by the ratio of two 4^{th} power quantities of the electric field.
As expected from the error analysis the depolarization ratios show excellent agreement between the simulations and measurements, with the maximum difference being only $\pm$ 16 %. This is a remarkable agreement, and it points perhaps towards a possible application of this approach for the study of substrates with particularly interesting depolarization behaviors as mentioned in [13] for instance.
The intensity ratios between batches are still in good agreement, though

significantly less strongly than the depolarization ratios. The largest difference between simulations and measurements is about 50 %, which is still in the error range from the standard deviations. This means that potential applications such as the comparison of different types of SERS substrates with each other, or perhaps an a priori prediction of the relative performance of nanostructures from highly accurate manufacturing techniques such as lithography might be possible.
Finally, the enhancement factors can only be expected to match for the 797.1 cm^{-1} band, due to the chemical enhancement of the 1078.2 cm^{-1} band. For the 797.1 cm^{-1} band the predictions are reasonably well, with the simulations and the measurements differing by a maximum of about a factor of 2. This is rather good given all the potential error sources involved, but it still severely limits possible applications, where highly accurate predictions about the electric fields would be necessary. For instance, trying to reverse eq. 3.36. (Chapter 3.4) in order to calculate the Raman tensor symmetry or the orientation of the molecule from the combined results of simulations and measurements was an idea already taken into account at the initial stages of this thesis, but this clearly would need much better accuracy of both the measurements and simulations. However, SERS enhancement factors are often only discussed in an order of magnitude context, and the accuracy of the simulations is certainly sufficient for that.
With regards to the 1078.2 cm^{-1} band the results from the simulations and measurements differ, as expected, due to chemical enhancement, with the simulated enhancement factors about a factor of 20 smaller than the measured ones. This is consistent with DFT simulations of a very similar molecule adsorbed on an Au substrate, which [16] give in case of benzenethiol for the same vibrational mode a shift of 20-25 cm^{-1} and a chemical enhancement by a factor of 5-25.

Chapter 5

Conclusion & Outlook

In the first part, which deals with the manufacture and characterization of the substrates, a preparation procedure for highly irregular SERS substrates was developed, that consists of the sputtering of Au nanoislands on either Si wafers or glass microscope slides. These substrates have been thoroughly examined with regards to their reproducibility. As a probe molecule in the early stages (only glass slide substrates tested) Methylene Blue was used and spin coated onto the substrates. Excellent reproducibility (5-10 % depending on the definition) was found in this case. But for the measurement of the enhancement factors the probe molecule was change to 4-MBT (deposited as a self-assembled monolayer) instead of the strongly fluorescent Methylene Blue. Using a SAM of 4-MBT reduced the reproducibility to around 20 % both on glass slides and Si wafers, and the significant increase in uncertainty can be mainly attributed to difficulties with the SAM deposition. In addition, a decrease in batch to batch reproducibility was found concerning substrates manufactured towards the end of the thesis, which can be attributed to variations in the mean thickness of the sputtered Au films (confirmed by AFM). But this cannot be credited to the sputter process itself, but could be attributed to minor problems with the sputter coater occurring at that time. In the interest of high quality AFM measurements, substrates based on Si wafers were preferred to those based on glass slides. The reason was that the surfaces of the glass slides were not really smooth. Two batches of these Si based substrates were characterized using both SEM and AFM in order to get high quality 3D measurements of the nanostructures responsible for the SERS enhancement. Finally, the enhancement factors and depolarization ratios of these batches were measured using established procedures found in the literature [29].
The purpose of this thesis was the development of a simulation toolbox for the calculation of SERS enhancement factors, based on accurate microscopic

measurements of difficult substrates with highly irregular and comparatively small features. But first an excellent 3D characterization of the structure of these substrates by microscopy had to be performed. These substrates represent a challenge in both the AFM measurements and the DDA simulations and are thus well suited for the testing purposes in this thesis. Nevertheless, further improvements are clearly possible. The most obvious next step would be to test a couple of different molecules, as the SAM deposition of 4-MBT introduced some problems. Also, with molecules with defined chain lengths (with a functional group at the end) investigations of the distance dependence would be possible. In addition, given the large variety of SERS manufacturing procedures, testing this approach on several considerably different substrates types (from high-end nanostructuring to particles in suspension) would be very interesting. Testing a larger variety of substrates would be especially challenging from an experimental point of view, as finding a prober microscopic technique for the 3D measurements of the structure of the substrates will be far from trivial.
The second part of the thesis deals with the generation of the software essential for the calculation of both the electric nearfields for the real substrate geometry and the calculation of the enhancement factors from the nearfields. To this aim a Matlab script that implements the discrete dipole approximation was written and tested. The script uses the quasi-static approximation in order to deal with the substrate, the FFT-based acceleration scheme to speed up calculations on rectangular grids and the integrated tensor approach to deal with the singularity of the Green's tensor. The integrated tensor approach was limited to a sufficient number of off-diagonal elements to speed up the algorithm at no loss of accuracy, a novelty for DDA scripts up to now. Tests of the algorithm using examples from Mie Theory and various plasmonic toolboxes confirmed the functionality of the script, and workable solutions (using the available computational resources) for all critical algorithm parameters were found. With the finally established simulation protocol, it is possible to simulate roughly a substrate area of 200x200 nm with a discretization step size of 0.5 nm. In addition, an automated procedure to generate the discretization grid from AFM images in the simulation software was established. For the calculation of the enhancement factors and depolarization ratios from the nearfields the theoretical derivations from Le Ru et al. [32] were used, and the calculations were limited to isotropic bands (depolarization ratios) and isotropic bands with no chemical enhancement (enhancement factors) respectively.
Several improvements of the current simulation software could be the topic of further research. They can be roughly divided into improvements within the realm of classical physics and others within that of quantum mechanics.

Concerning classical physics the most obvious direct improvement to the algorithm would be the incorporation of the novel approach to the dielectric substrate as elaborated by Yurkin et al [65]. Additionally, the addition of the possibility to periodically extend the simulated area [61] and include the dielectric influence of 4-MBT (or any probe SAM) itself in the simulations would be desirable. Of course, with the availability of significantly stronger computational resources the testing of both larger areas and smaller discretization step sizes would also be interesting. Concerning quantum mechanics, the next step would be to incorporate the variation of the dielectric function close to the surface using some semi-classical approach suggested in the literature [87, 88]. Going even further, the variation of the dielectric function across the combined molecule-nanostructure surface complex could be taken into account, which would in any case make full quantum mechanical simulations of the molecule adsorbed on the material of the nanostructure necessary. This would not only have the advantage of being a highly accurate representation of the dielectric function (and thus improve the nearfield calculations), but this would also provide information about the chemical enhancement, orientation and Raman tensor of the vibrational mode of the molecule.

The third and final part of the thesis deals with the comparison between simulated and measured enhancement factors and depolarization ratios. As mentioned above, the comparison is restricted to isotropic bands, and two batches of 8 substrates each are used for the comparison. For the depolarization ratios excellent agreement was found, while the calculated electromagnetic enhancement factors were within about of 2 of the measurement. The larger difference for the enhancement factors can be attributed to a combination of the many uncertainty factors already mentioned, such as the surface coverage/surface density of the 4-MBT monolayer at the substrate, the dielectric influence of the 4-MBT or the variation of the dielectric function close to the surface of the nanostructure.

But altogether this is a very good agreement between simulations and measurements, which confirms the applicability and reliability of all parts of the simulation software. Thus, a useful toolbox for the simulation of the real geometry of SERS substrates is provided by this thesis. At this point two paths for further research can be suggested. One option would be to put a focus on the improvement of the simulation algorithm with the ultimate aim of highly accurate simulations concerning specific tailored substrates (perhaps produced by a high-end nanostructuring techniques). This would enable the calculation (possibly only limited to depolarization ratios) of unknown quantities such as the Raman tensor or the adsorption geometry of molecules. It could be accomplished by a combination of measurement

results, simulation results and reversing eqs. 3.39-3.41 (see chapter 3.4) for the unknown quantities. The second option would be to focus on the application of the method on a broad variety of SERS substrates. The ultimate aim of this would be to provide the SERS community with a least qualitative information about the hot spot distribution, expected the order of magnitude of electromagnetic enhancement that can be expected (as a function of wavelengths) and the depolarization behavior for common SERS substrate types.

References

[1] M. Fleischmann, P.J. Hendra, and A.J. McQuillan. "Raman spectra of pyridine adsorbed at a silver electrode". In: *Chemical Physics Letters* 26.2 (1974), pp. 163–166.

[2] Meikun Fan, Gustavo FS Andrade, and Alexandre G Brolo. "A review on the fabrication of substrates for surface enhanced Raman spectroscopy and their applications in analytical chemistry". In: *Analytica chimica acta* 693.1-2 (2011), pp. 7–25.

[3] Sebastian Schlücker. "Oberflächenverstärkte Raman-Spektroskopie: Konzepte und chemische Anwendungen". In: *Angewandte Chemie* 126.19 (2014), pp. 4852–4894.

[4] Dana Cialla et al. "Surface-enhanced Raman spectroscopy (SERS): progress and trends". In: *Analytical and bioanalytical chemistry* 403.1 (2012), pp. 27–54.

[5] Hongxing Xu et al. "Spectroscopy of Single Hemoglobin Molecules by Surface Enhanced Raman Scattering". In: *Phys. Rev. Lett.* 83 (21 1999), pp. 4357–4360.

[6] Xin Sun and Hao Li. "Gold nanoisland arrays by repeated deposition and post-deposition annealing for surface-enhanced Raman spectroscopy". In: *Nanotechnology* 24.35 (2013), p. 355706.

[7] Ralph A. Tripp, Richard A. Dluhy, and Yiping Zhao. "Novel nanostructures for SERS biosensing". In: *Nano Today* 3.3 (2008), pp. 31–37.

[8] Ping Gao et al. "Surface-enhanced Raman scattering at gold electrodes: dependence on electrochemical pretreatment conditions and comparisons with silver". In: *Journal of Electroanalytical Chemistry and Interfacial Electrochemistry* 233.1 (1987), pp. 211–222.

[9] L. Gunnarsson et al. "Interparticle coupling effects in nanofabricated substrates for surface-enhanced Raman scattering". In: *Applied Physics Letters* 78.6 (2001), pp. 802–804.

[10] Anuj Dhawan, Michael Gerhold, and Tuan Vo-Dinh. "Theoretical Simulation and Focused Ion Beam Fabrication of Gold Nanostructures for Surface-Enhanced Raman Scattering (SERS)". In: *NanoBiotechnology* 3.3 (2007), pp. 164–171.

[11] Song-Yuan Ding et al. "Surface-Enhanced Raman Spectroscopy (SERS): General Introduction". In: *Encyclopedia of Analytical Chemistry*. American Cancer Society, 2014, pp. 1–34.

[12] Martin Moskovits. "Surface-enhanced Raman spectroscopy: a brief retrospective". In: *Journal of Raman Spectroscopy: An International Journal for Original Work in all Aspects of Raman Spectroscopy, Including Higher Order Processes, and also Brillouin and Rayleigh Scattering* 36.6-7 (2005), pp. 485–496.

[13] EC Le Ru et al. "Experimental verification of the SERS electromagnetic model beyond the E4 approximation: polarization effects". In: *The Journal of Physical Chemistry C* 112.22 (2008), pp. 8117–8121.

[14] EC Le Ru and PG Etchegoin. "Rigorous justification of the E4 enhancement factor in surface enhanced Raman spectroscopy". In: *chemical Physics letters* 423.1-3 (2006), pp. 63–66.

[15] EC Le Ru et al. "Advanced aspects of electromagnetic SERS enhancement factors at a hot spot". In: *Journal of Raman Spectroscopy: An International Journal for Original Work in all Aspects of Raman Spectroscopy, Including Higher Order Processes, and also Brillouin and Rayleigh Scattering* 39.9 (2008), pp. 1127–1134.

[16] Semion K Saikin et al. "Separation of electromagnetic and chemical contributions to surface-enhanced Raman spectra on nanoengineered plasmonic substrates". In: *The Journal of Physical Chemistry Letters* 1.18 (2010), pp. 2740–2746.

[17] Encai Hao and George C Schatz. "Electromagnetic fields around silver nanoparticles and dimers". In: *The Journal of chemical physics* 120.1 (2004), pp. 357–366.

[18] Nahla A Hatab et al. "Free-standing optical gold bowtie nanoantenna with variable gap size for enhanced Raman spectroscopy". In: *Nano letters* 10.12 (2010), pp. 4952–4955.

[19] Sebastian Heeg et al. "Polarized plasmonic enhancement by Au nanostructures probed through Raman scattering of suspended graphene". In: *Nano letters* 13.1 (2012), pp. 301–308.

[20] I Sow et al. "Revisiting surface-enhanced Raman scattering on realistic lithographic gold nanostripes". In: *The Journal of Physical Chemistry C* 117.48 (2013), pp. 25650–25658.

[21] Kristin L Wustholz et al. "Structure- activity relationships in gold nanoparticle dimers and trimers for surface-enhanced Raman spectroscopy". In: *Journal of the American Chemical Society* 132.31 (2010), pp. 10903–10910.

[22] Pamela A Mosier-Boss. "Review of SERS substrates for chemical sensing". In: *Nanomaterials* 7.6 (2017), p. 142.

[23] Piotr J Flatau, Graeme L Stephens, and Bruce T Draine. "Light scattering by rectangular solids in the discrete-dipole approximation: a new algorithm exploiting the Block–Toeplitz structure". In: *JOSA A* 7.4 (1990), pp. 593–600.

[24] Bruce T Draine and Piotr J Flatau. "Discrete-dipole approximation for scattering calculations". In: *JOSA A* 11.4 (1994), pp. 1491–1499.

[25] Sheng-Uei Fang et al. "Surface roughness-correlated SERS effect on Au island-deposited substrate". In: *Journal of Electroanalytical Chemistry* 741 (2015), pp. 127–133.

[26] Bhavya Sharma et al. "SERS: Materials, applications, and the future". In: *Materials Today* 15.1 (2012), pp. 16–25.

[27] Vincenzo Amendola, Osman M. Bakr, and Francesco Stellacci. "A Study of the Surface Plasmon Resonance of Silver Nanoparticles by the Discrete Dipole Approximation Method: Effect of Shape, Size, Structure, and Assembly". In: *Plasmonics* 5.1 (2010), pp. 85–97.

[28] Hufang Xu et al. "Deposition of ordered arrays of copper nano dots by using selfassembled nanoporous silica as the template". In: *Microscopy and Microanalysis* 9.S02 (2003), pp. 432–434.

[29] EC Le Ru et al. "Surface enhanced Raman scattering enhancement factors: a comprehensive study". In: *The Journal of Physical Chemistry C* 111.37 (2007), pp. 13794–13803.

[30] Matthew Rycenga et al. "Surface-enhanced Raman scattering: comparison of three different molecules on single-crystal nanocubes and nanospheres of silver". In: *The Journal of Physical Chemistry A* 113.16 (2009), pp. 3932–3939.

[31] Kwan Kim et al. "Surface-Enhanced Raman Scattering Characteristics of 4-Aminobenzenethiol Derivatives Adsorbed on Silver". In: *The Journal of Physical Chemistry C* 115.50 (2011), pp. 24960–24966.

[32] Eric Le Ru and Pablo Etchegoin. *Principles of Surface-Enhanced Raman Spectroscopy: and related plasmonic effects*. Elsevier, 2008.

[33] Pedro HC Camargo et al. "Measuring the SERS enhancement factors of dimers with different structures constructed from silver nanocubes". In: *Chemical physics letters* 484.4-6 (2010), pp. 304–308.

[34] J. L. Martinez, Y. Gao, and T. Lopez-Rios. "Surface-enhanced Raman scattering of obliquely evaporated Ag films". In: *Phys. Rev. B* 33 (8 1986), pp. 5917–5919.

[35] David J. Semin and Kathy L. Rowlen. "Influence of vapor deposition parameters on SERS active Ag film morphology and optical properties." In: *Analytical Chemistry* 66 (23 1994), pp. 4324–4331.

[36] J. Spadavecchia et al. "Au Nanoparticles Prepared by Physical Method on Si and Sapphire Substrates for Biosensor Applications". In: *The Journal of Physical Chemistry B* 109.37 (2005), pp. 17347–17349.

[37] U.S. Dinish et al. "Development of highly reproducible nanogap SERS substrates: Comparative performance analysis and its application for glucose sensing". In: *Biosensors and Bioelectronics* 26.5 (2011), pp. 1987–1992.

[38] Won Joon Cho, Youngsuk Kim, and Jin Kon Kim. "Ultrahigh-Density Array of Silver Nanoclusters for SERS Substrate with High Sensitivity and Excellent Reproducibility". In: *ACS Nano* 6.1 (2012), pp. 249–255.

[39] Xiuneng Song et al. "Density functional theory study of NEXAFS spectra of 4-methylbenzenethiol molecule". In: *Chemical Physics Letters* 645 (2016), pp. 164–168.

[40] Kyoungja Seo and Eric Borguet. "Potential-induced structural change in a self-assembled monolayer of 4-methylbenzenethiol on Au (111)". In: *The Journal of Physical Chemistry C* 111.17 (2007), pp. 6335–6342.

[41] Katsuyoshi Ikeda, Shuto Suzuki, and Kohei Uosaki. "Enhancement of SERS Background through Charge Transfer Resonances on Single Crystal Gold Surfaces of Various Orientations". In: *Journal of the American Chemical Society* 135.46 (2013), pp. 17387–17392.

[42] J. Christopher Love et al. "Self-Assembled Monolayers of Thiolates on Metals as a Form of Nanotechnology". In: *Chemical Reviews* 105.4 (2005), pp. 1103–1170.

[43] Tai Ha Joo, Myung Soo Kim, and Kwan Kim. "Surface-enhanced Raman scattering of benzenethiol in silver sol". In: *Journal of Raman spectroscopy* 18.1 (1987), pp. 57–60.

[44] JHS Green and DJ Harrison. "Vibrational spectra of benzene derivatives-X: monosubstituted nitrobenzenes". In: *Spectrochimica Acta Part A: Molecular Spectroscopy* 26.9 (1970), pp. 1925–1937.

[45] Semion K. Saikin et al. "On the chemical bonding effects in the Raman response: Benzenethiol adsorbed on silver clusters". In: *Phys. Chem. Chem. Phys.* 11 (41 2009), pp. 9401–9411.

[46] Weiwei He et al. "Design of AgM Bimetallic Alloy Nanostructures (M = Au, Pd, Pt) with Tunable Morphology and Peroxidase-Like Activity". In: *Chemistry of Materials* 22.9 (2010), pp. 2988–2994.

[47] "Preparation of Au-Ag coreshell nanoparticles and application of bimetallic sandwich in surface-enhanced Raman scattering (SERS)". In: *Colloids and Surfaces A: Physicochemical and Engineering Aspects* 257-258 (2005), pp. 313–317.

[48] Ludwig Reimer. *Scanning Electron Microscopy*. Springer, 1998.

[49] G. Binnig, C. F. Quate, and Ch. Gerber. "Atomic Force Microscope". In: *Phys. Rev. Lett.* 56 (9 1986), pp. 930–933.

[50] R. Gracia. *Amplitude Modulation Atomic Force Microscopy*. John Wiley and Sons, 2010.

[51] Maxim A Yurkin and Alfons G Hoekstra. "The discrete dipole approximation: an overview and recent developments". In: *Journal of Quantitative Spectroscopy and Radiative Transfer* 106.1-3 (2007), pp. 558–589.

[52] F Michael Kahnert. "Numerical methods in electromagnetic scattering theory". In: *Journal of Quantitative Spectroscopy and Radiative Transfer* 79 (2003), pp. 775–824.

[53] E.M. Purcell and C.R. Pennypacker. "Scattering and absorption of light by nonspherical dielectric grains". In: *The Astrophysical Journal* 186 (1973), pp. 705–714.

[54] B. T. Draine. "The discrete-dipole approximation and its application to interstellar graphite grains". In: *Astrophysical Journal, Part 1* 333 (1988), pp. 848–872.

[55] B. T. Draine and J Goodman. "Beyond Clausius-Mossotti - Wave propagation on a polarizable point lattice and the discrete dipole approximation". In: *Astrophysical Journal, Part 1* 11.2 (1993), pp. 685–697.

[56] Bruce T. Draine and Piotr J. Flatau. "Discrete-Dipole Approximation For Scattering Calculations". In: *J. Opt. Soc. Am. A* 11.4 (1994), pp. 1491–1499.

[57] George H. Goedecke and Sean G. O'Brien. "Scattering by irregular inhomogeneous particles via the digitized Green's function algorithm". In: *Appl. Opt.* 27.12 (1988), pp. 2431–2438.

[58] A. Lakhtakia. "Strong and weak forms of the method of moments and the coupled dipole method for scattering of time-harmonic electromagnetic fields". In: *International Journal of Modern Physics C* 03.03 (1992), pp. 583–603.

[59] J. Rahola. "Solution of Dense Systems of Linear Equations in the Discrete-Dipole Approximation". In: *SIAM Journal on Scientific Computing* 17.1 (1996), pp. 78–89.

[60] Nicolas B. Piller. "Coupled-dipole approximation for high permittivity materials". In: *Optics Communications* 160.1 (1999), pp. 10–14.

[61] Patrick C Chaumet, Adel Rahmani, and Garnett W Bryant. "Generalization of the coupled dipole method to periodic structures". In: *Physical Review B* 67.16 (2003), p. 165404.

[62] Nicolas B. Piller. "Influence of the edge meshes on the accuracy of the coupled-dipole approximation". In: *Opt. Lett.* 22.22 (1997), pp. 1674–1676.

[63] Jackson JD. *Classical Electrodynamics*. New York: Wiley, 1975.

[64] Benjamin E Barrowes, Fernando L Teixeira, and Jin A Kong. "Fast algorithm for matrix–vector multiply of asymmetric multilevel block-Toeplitz matrices in 3-D scattering". In: *Microwave and Optical technology letters* 31.1 (2001), pp. 28–32.

[65] Maxim A. Yurkin and Marcus Huntemann. "Rigorous and Fast Discrete Dipole Approximation for Particles near a Plane Interface". In: *The Journal of Physical Chemistry C* 119.52 (2015), pp. 29088–29094.

[66] K. Lance Kelly et al. "The Optical Properties of Metal Nanoparticles: The Influence of Size, Shape, and Dielectric Environment". In: *The Journal of Physical Chemistry B* 107.3 (2003), pp. 668–677.

[67] Eduardo M. Perassi et al. "Quantitative Understanding of the Optical Properties of a Single, Complex-Shaped Gold Nanoparticle from Experiment and Theory". In: *ACS Nano* 8.5 (2014), pp. 4395–4402.

[68] Sameh Kessentini et al. "Gold Dimer Nanoantenna with Slanted Gap for Tunable LSPR and Improved SERS". In: *The Journal of Physical Chemistry C* 118.6 (2014), pp. 3209–3219.

[69] Stephanie L. Dodson et al. "Engineering plasmonic nanorod arrays for colon cancer marker detection". In: *Biosensors and Bioelectronics* 63 (2015), pp. 472–477.

[70] Roland Schmehl, Brent M Nebeker, and E Dan Hirleman. "Discrete-dipole approximation for scattering by features on surfaces by means of a two-dimensional fast Fourier transform technique". In: *JOSA A* 14.11 (1997), pp. 3026–3036.

[71] T Yamaguchi, S Yoshida, and A Kinbara. "Optical effect of the substrate on the anomalous absorption of aggregated silver films". In: *Thin solid films* 21.1 (1974), pp. 173–187.

[72] Wen-Hui Yang, George C Schatz, and Richard P Van Duyne. "Discrete dipole approximation for calculating extinction and Raman intensities for small particles with arbitrary shapes". In: *The Journal of chemical physics* 103.3 (1995), pp. 869–875.

[73] Philippe Gay-Balmaz and Olivier JF Martin. "Validity domain and limitation of non-retarded Green's tensor for electromagnetic scattering at surfaces". In: *Optics Communications* 184.1-4 (2000), pp. 37–47.

[74] Lihong Gao, F Lemarchand, and M Lequime. "Refractive index determination of SiO2 layer in the UV/Vis/NIR range: spectrophotometric reverse engineering on single and bi-layer designs". In: *Journal of the European Optical Society-Rapid publications* 8 (2013).

[75] James Parsons et al. "A comparison of techniques used to simulate the scattering of electromagnetic radiation by metallic nanostructures". In: *Journal of Modern Optics* 57.5 (2010), pp. 356–365.

[76] Vincent LY Loke et al. "Comparison between discrete dipole approximation and other modelling methods for the plasmonic response of gold nanospheres". In: *Applied Physics B* 115.2 (2014), pp. 237–246.

[77] Juergen Waxenegger, Andreas Truegler, and Ulrich Hohenester. "Plasmonics simulations with the MNPBEM toolbox: Consideration of substrates and layer structures". In: *Computer Physics Communications* 193 (2015), pp. 138–150.

[78] Jan-Patrick Schäfer. "Implementierung und Anwendung analytischer und numerischer Verfahren zur Lösung der Maxwellgleichungen für die Untersuchung der Lichtausbreitung in biologischem Gewebe". PhD thesis. Universität Ulm. Fakultät für Naturwissenschaften, 2011.

[79] Vincent LY Loke, M Pinar Mengüç, and Timo A Nieminen. "Discrete-dipole approximation with surface interaction: Computational toolbox for MATLAB". In: *Journal of Quantitative Spectroscopy and Radiative Transfer* 112.11 (2011), pp. 1711–1725.

[80] Ulrich Hohenester and Andreas Trügler. "MNPBEM–A Matlab toolbox for the simulation of plasmonic nanoparticles". In: *Computer Physics Communications* 183.2 (2012), pp. 370–381.

[81] Jiang et al. "Single Molecule Raman Spectroscopy at the Junctions of Large Ag Nanocrystals". In: *The Journal of Physical Chemistry B* 107.37 (2003), pp. 9964–9972.

[82] Katrin Kneipp et al. "Surface-enhanced Raman scattering and biophysics". In: *Journal of Physics: Condensed Matter* 14.18 (2002), R597.

[83] Hongxing Xu et al. "Unified treatment of fluorescence and Raman scattering processes near metal surfaces". In: *Physical review letters* 93.24 (2004), p. 243002.

[84] Harald Fitzek et al. "Accurate Near-Field Simulations of the Real Substrate Geometry—A Powerful Tool for Understanding Surface-Enhanced Raman Spectroscopy". In: *The Journal of Physical Chemistry C* 122.12 (2018), pp. 6826–6834.

[85] Peter B Johnson and R-W_ Christy. "Optical constants of the noble metals". In: *Physical review B* 6.12 (1972), p. 4370.

[86] Z Fatih Öztürk et al. "Field enhancement at metallic interfaces due to quantum confinement". In: *Journal of Nanophotonics* 5.1 (2011), p. 051602.

[87] Rubén Esteban et al. "A classical treatment of optical tunneling in plasmonic gaps: extending the quantum corrected model to practical situations". In: *Faraday Discuss.* 178 (2015), pp. 151–183.

[88] Yu Luo et al. "Surface Plasmons and Nonlocality: A Simple Model". In: *Phys. Rev. Lett.* 111 (9 2013), p. 093901.

[89] PJ Flatau and BT Draine. "Fast near field calculations in the discrete dipole approximation for regular rectilinear grids". In: *Optics express* 20.2 (2012), pp. 1247–1252.

List of publications

Articles (lead author):

1. **Fitzek, H.M.**, Sattelkow, J., Plank, H. & Pölt P.; *Accurate Near-Filed Simulations of the Real Substrate Geometry – A Powerful Tool for Understanding Surface-Enhanced Raman Spectroscopy.* The Journal of Physical Chemistry. 122, 12, p. 6826-6834 (2018)

2. **Fitzek, H.M.**, Schröttner, H., Wagner J., Hofer, F. & Rattenberger, J.; *High-quality imaging in environmental scanning electron microscopy – optimizing the pressure limiting system and the secondary electron detection of a commercially available ESEM.* Journal of microscopy. 262, p. 85-91 (2016)

3. **Fitzek, H.M.**, Schröttner, H., Wagner J., Hofer, F. & Rattenberger, J.; *Experimental evaluation of environmental scanning electron microscopes at high chamber pressure.* Journal of microscopy. 260, p. 133-139 (2015)

Articles (co-author):

1. Chien, H-T., Pilat, F., Griesser, T., **Fitzek, H.M.**, Pölt, P. & Friedel, B.; *Influence of Environmentally Affected Hole-Transport Layers on Spatial Homogeneity and Charge-Transport Dynamics of Organic Solar Cells.* ACS Applied Materials and Interfaces. 10, p. 10102-10114 (2018)

2. Haas, M., Christopoulos, V-S., Radebner, J., Holthausen, M., Lainer, T., Schuh, L., **Fitzek, H. M.**, Kothleitner, G., Torvisco Gomez, A., Fischer, R., Wunnicke, O. & Stüger, H.; *Branched Hydrosilane Oligomers as Ideal Precursors for Liquid-Based Silicon-Film Deposition.* Angewandte Chemie. 56, p. 14259-14262 (2017)

3. Nachtnebel, M., **Fitzek, H. M.**, Mayrhofer, C., Chernev, B. S. & Pölt, P.; *Spatial localization of membrane degradation by in situ wetting and drying of membranes in the scanning electron microscope.* Journal of membrane science. 503, p. 81-89 (2016)

4. Ganner, T., Rosker, S., Eibinger, M., Kraxner, J., Sattelkow, J., Rattenberger, J., **Fitzek, H. M.**, Chernev, B. S., Grogger, W., Nidetzky, B. & Plank, H.; *Tunable Semicrystalline Thin Film Cellulose Substrate for High- Resolution, In-Situ AFM Characterization of Enzymatic Cellulose Degradation.* ACS applied materials & interfaces. 7, 50, p. 27900-27909 (2015)

5. Geier, B., Gspan, C., Fowlkes, J. D., **Fitzek, H. M.**, Rauch, S., Rattenberger, J., Rack, P. D., Plank, H. & Winkler, R.; *Rapid and Highly Compact Purification for Focused Electron Beam Induced Deposits: A Low Temperature Approach Using Electron Stimulated H2O Reactions.* The Journal of Physical Chemistry. 118, 25, p. 14009-14016 (2014)

Conference talks (speaker):

1. **Fitzek, H. M.**; *Recent developments in correlative SEM-Raman confocal microscopy, examples of application and perspective.* Annual Meeting of the Hungarian Society for Microscopy 2018, Siofok, Hungary (2018)

2. **Fitzek, H. M.**; *Understanding surface enhanced Raman spectroscopy using accurate nearfield-simulation of real substrates.* 9th International Conference on Advanced Vibrational spectroscopy, Victoria, Canada (2017)

3. **Fitzek, H.M.**, Sattelkow, J. & Pölt P.; *Looking for the origin of surface enhanced Raman spectroscopy using an atomic force microscope.* 6th ASEM Workshop, Leoben, Austria (2016)

4. **Fitzek, H. M.**, Brandl, C., Mayrhofer, C., Beuchel, R. I. B., Nachtnebel, M. & Chernev, B. S.; *IR/Ramanmikroskopie: Anwendungen zur chemischen Analyse von mm bis µm.* Soft Matter Workshop 2015, Graz, Austria (2015)

5. **Fitzek, H. M.**, Schröttner, H., Wagner, J., Nachtnebel, M., Hofer, F. & Rattenberger, J.; *Optimizing the Environmental Scanning Electron Microscope for the investigation of wet samples.* Materials Day 2015, Graz, Austria (2015)

6. **Fitzek, H. M.**, Schröttner, H., Wagner, J., Hofer, F. & Rattenberger, J.; *Optimizing the environmental scanning electron microscope - getting high image quality above 1000 Pa.* 12th Multinational Congress on Microscopy, Eger, Hungary (2015)

7. **Fitzek, H. M.**, Schröttner, H., Wagner, J., Hofer, F. & Rattenberger, J.; *Simulating the pressure limiting system of Environmental Scanning Electron Microscopes using the direct simulation Monte-Carlo method.* 5th ASEM Workshop, Graz, Austria (2015)

Conference talks (co-author):

1. Striemitzer R., Pölt P. & **Fitzek, H. M.**; *Dealing with light refraction in 3D mapping in combined Raman/SEM.* 7th ASEM Workshop, Vienna, Austria (2017)

2. Ganner, T., Eibinger, M., Rosker, S., Sattelkow, J., Aschl, T., Rattenberger, J., **Fitzek, H. M.**, Nidetzky, B. & Plank, H.; *Artificial Substrates as Key Element towards Single Enzyme Tracking via High Speed Atomic Force Microscopy in Enzymatic Degradation of Cellulose.* 5th ASEM Workshop, Graz, Austria (2015)

3. Nachtnebel, M., **Fitzek, H. M.**, Mayrhofer, C., Brandl, C., Chernev, B. S. & Pölt, P.; *Characterisation of microfiltration membranes by in situ wetting in the ESEM and FT-IR.* 5th ASEM Workshop, Graz, Austria (2015)

4. Nachtnebel, M., **Fitzek, H. M.**, Chernev, B. S. & Pölt, P.; *In situ analysis of PES microfiltration membrane degradation in the ESEM.* Microscopy Conference 2015, Göttingen, Germany (2015)

Conference poster (presenter):

1. **Fitzek, H. M.**, Schmuck, K., Burtscher, B., Uhde, N., Riemer, C., Miltscho, A., Menguy, J., Ganglbauer, J., Namdar, P., Ranz, M., Messner, R., Müller, H., Moreira, A., Meszaros, R., Winkler, C., Tumphart, S., Hofer, S., Zajki-Zechmeister, K., Zettl, P. & Pölt, P.; *Student vs Spectrometer - Comparing food differentiation by human taste buds and by Raman spectroscopy.* Materials Day 2017, Graz, Austria (2017)

2. **Fitzek, H. M.**, Sattelkow, J. & Pölt, P.; *Understanding surface enhanced Raman spectroscopy using accurate simulations of electric nearfields.* 7th ASEM Workshop, Vienna, Austria (2017)

3. **Fitzek, H. M.**, Sattelkow, J. & Pölt, P.; *Investigation of the near fields of sputtered Au thinfilms used for SERS, using the AFM and DDA.* 16th European Microscopy Congress, Lyon, France (2016)

4. **Fitzek, H. M.** & Pölt, P.; *Where Does the Signal Come From? An Easy-to-use Spatial Characterization Method of the Laser Intensity and Detection efficiency for Confocal Raman Spectroscopy.* Ramanfest 2016, Berlin, Germany (2016)

5. **Fitzek, H. M.**, Lembacher, C. & Chernev, B. S.; *Preventing oil contamination during immersion confocal Raman.* ICAVS 8, Vienna, Austria (2015)

Conference posters (co-author):

1. Rattenberger, J., **Fitzek, H. M.**, Schröttner, H., Wagner, J. & Hofer, F.; *Optimizing the Environmental Scanning Electron Microscope for In Situ Applications.* Materials Science and Engineering 2016, Darmstadt, Germany (2016)

2. Rattenberger, J., **Fitzek, H. M.**, Schröttner, H., Wagner, J. & Hofer, F.; *Pushing the Limits of Environmental Scanning Electron Microscopy. 16th European Microscopy Congress*, Lyon, France (2016)

3. Nachtnebel, M., **Fitzek, H. M.**, Brandl, C., Loulergue, P., Teychene, B. & Pölt, P.; *Spatial characterization of PES/PVP based membranes by FT-IR.* PERMA- MELPRO, Prag, Czech Republic (2016)

4. Nachtnebel, M., **Fitzek, H. M.**, Mayrhofer, C., Brandl, C., Chernev, B. S. & Pölt, P.; *Spatially Resolved Characterisation of Microfiltration Membranes by two Different Microscopic Methods.* Euromembrane 2015, Aachen, Germany (2015)

5. Rattenberger, J., **Fitzek, H. M.**, Wagner, J., Schröttner, H. & Hofer, F.; *Experimental evaluation of Environmental Scanning Electron Microscopes at high chamber pressure [200 - 4000 Pascal].* 18th IMC, Prag, Czech Republic (2014)

Conference proceedings (lead author):

1. **Fitzek, H. M.**, Sattelkow, J. & Pölt, P.; *Understanding surface enhanced Raman spectroscopy using accurate simulations of electric nearfields.* 2017 ASEM. p. 45 (2017)

2. **Fitzek, H.M.**, Sattelkow, J. & Pölt P.; *Looking for the origin of surface enhanced Raman spectroscopy using an atomic force microscope.* 6th ASEM Workshop. Leoben, p. 18 1 p. (2016)

3. **Fitzek, H. M.** & Pölt, P.; *Where Does the Signal Come From? An Easy-to-use Spatial Characterization Method of the Laser Intensity and Detection efficiency for Confocal Raman Spectroscopy.* International Raman Fest. Berlin, p. 50-51 2 p. (2016)

Conference proceedings (co-author):

1. Striemitzer R., Pölt P. & **Fitzek, H. M.**; *Dealing with light refraction in 3D mapping in combined Raman/SEM.* 2017 ASEM. p. 34 (2017)

2. Gspan, C., Grogger, W., Fitzek, H. M., Knez, D., Kothleitner, G., Gatterer, K. & Hofer, F.; *Direct imaging of channel constituents in beryl.* IAMNano 2017. p. 23 (2017)

3. Rattenberger, J., Achtsnit, T., **Fitzek, H. M.**, Schröttner, H. & Hofer, F.; *Universal pressure scanning electron microscopy (UPSEM) –electron microscopy from high vacuum to atmospheric pressure.* MC2017. p. IM1.012 (2017)

4. Rattenberger, J., **Fitzek, H. M.**, Achtsnit, T. & Schröttner, H.; U*niversal pressure scanning electron microscopy (UPSEM) - electron microscopy up to atmospheric pressure.* 13th Multinational Congress on Microscopy. p. 173-175 (2017)

5. Ganner, T., Sattelkow, J., Rosker, S., Eibinger, M., Chernev, B. S., **Fitzek, H. M.**, Kraxner, J., Mayrhofer, C., Aschl, T., Nidetzky, B. & Plank, H.; *Artificial Substrates as Key Element towards Single Enzyme Tracking via High Speed Atomic Force Microscopy in Enzymatic Degradation of Cellulose.* 2015 ASEM Workshop Advanced Electron Microscopy, p. 30-30 (2015)

6. Nachtnebel, M., **Fitzek, H. M.**, Mayrhofer, C., Brandl, C., Chernev, B. S. & Pölt, P.; *Characterization of microfiltration membranes by in-situ wetting in the ESEM and FT-IR mapping.* 2015 ASEM Workshop Advanced Electron Microscopy, p. 32-32 (2015)

7. Pölt, P., Nachtnebel, M., **Fitzek, H. M.** & Chernev, B. S.; *In-situ analysis of PES microfiltration membrane degradation in the ESEM.* 2015 Microscopy Conference., p. 501-502 (2015)

Appendix A

Appendix

A.1 Input parameter list

The full list of input parameters of the simulation is given in four tables split by the respective topic of the simulation. These topics are the simulation algorithm (Table A.1), the data treatment and output files and figures (Table A.2), the physical properties of the scattering problem (Table A.3) and the generation of the geometry (Table A.4). The source code where all the parameters are defined can be found in appendix A.3. A default value of the parameters will be provided where necessary, and all simulations in this thesis were done with the default values, unless explicitly stated otherwise.

Table A.1: Algorithm specific parameters

Parameter name	Description	Default value
par.nx; par.ny; par.nz	Number of discretization steps in x, y and z	Chosen such that the discretization step size is 0.5 nm
par.xlimit; par.ylimit	Size of the simulation in x and y in meters	Not applicable
par.x0; par.y0	Center of the region of interest in the coordinates of the original AFM image in meters	Not applicable
par.maxit	Maximum number of the outer iterations of the gmres-routine; Note: Maximum total number of iterations = par.maxit*par.gm	10
par.gm	Maximum number of the inner iterations of the gmres-routine; Note: If par.gm=0 than the matlab routine bicgstab rather than gmres is used	20
par.tol	The goal minimal residual of the gmres-routine	10^{-2} (see chapter x)
par.order	Order of the initial guess vector for the gmes-routine	0 (0^{th} order = all polarizations chosen as 0)
par.points	If this flag is set (=1) than the final fields are calculated pointwise and not using the FFT-routine from [89]	0 (FFT routine is used for the final field calculation)
par.IT	[a,b,c]; If a=1 the integrated tensor approach is used otherwise the lattice dispersion relation is used for the polarizabilities and no tensor elements are integrated; b is the depth of the off-diagonals that is being integrated; c is a parameter specifying the accuracy of the numerical integration routine used	[1,5,20]; Integrated tensor is used to a depth of 5 (see chapter x)
par.pad_fft	If set to 1 all vectors are zero padded before the FFT (increases speed at the cost of memory)	1 (zero padding is used)
Par.Cscat_ex	If this is set to 1 the more complicated independent equation for the calculation of the scattering cross section [51] is used, otherwise C_{scat} = C_{ext} - C_{abs} (conservation of energy) is used	0 (simple equation is used)

Table A.2: Parameters specific to data treatment, output files and figures

Parameter name	Description	Default value
par.rx; par.ry; par.rz	Improvement factor of the resolution (by interpolation) for the plots generated by par.plotint	4
par.plotgeometry	If this flag is set (=1) than 2 plots of the geometry will be generated; One is showing the simulated geometry according to the function AFM and the other is showing the dipole positions (see chapter x)	1 (geometry is plotted)
par.plotint	If this flag is set (=1) the plots shown in chapter x (fig a-c) are generated	1 (plots are generated)
par.evaldist	If this flag is set (=1) the average electric field strength (also E2 and E4) as a function of distance from the surface will be calculated and plotted	0 (distance dependence is not calculated)
par.null	If this flag is set (=1) the internal fields in the plots generated by par.plotint are displayed as 0 to make the geometry of the scatterer more easily visible	1 (internal fields are not plotted for clarity)
par.Mieel	If this flag is set (=1) a test run where the DDA is compared to Mie Theory on a sphere (with geometry specified by par.Circ) is done	0 (no test run is done)
par.save_Ind	If this flag is set the results (see chapter x) and all generated plots are automatically saved	0 (results are not automatically saved)
par.dist	Distance from the surface at which the 3D-plots (see chapter x; fig a-c) are generated in meters	2 discretization steps sizes

Table A.3: Parameters specific to the physics of the scattering problem

Parameter name	Description	Default value
par.lambda	Wavelength of the incident field in meter	Not applicable
par.m_media	Refractive index of the background medium	1 (=air)
par.layer	[a,b,c,d,e]; If a=1 a dielectric layer is put into the simulation between the substrate and the nanostructure; b = dielectric constant of the layer; c,d = size of the layer in x and y; e = thickness of the layer	a=0 (no dielectric layer is added)
par.substrat_quasi	[a,b]; If a=1 a substrate is simulated using the mirror approximation (see chapter x); b = dielectric constant of the substrate	a=1 (substrate is simulated); b= $\epsilon(SiO_2, \lambda)$; the dielectric constant of SiO2 [74] at the incident wavelength is used
par.eps	[a,b]; Dielectric constant of the scatterer	The dielectric constant of gold [85] at the incident wavelength is used
par.E0	[a,b]; Polarization vector of the incident field	Not applicable

Table A.4: Geometry specific parameters

Parameter name	Description	Default value
par.loadAFM	If this flag is set (=1) and AFM image is load to generate a geometry; otherwise a sphere specified by par.Circ is simulated	1 (AFM image is used for the geometry)
par.hAFM	Allows a shift of the AFM image up or down in meters (was only used for test purposes)	0 (no height shift of the AFM image)
par.Circ	[r,x,y,z]; r is the radius of the sphere in meters; x,y,z are the coordinates of the center of the sphere in meters	Not applicable
par.xleng; par.yleng	Size of the AFM image in x and y in meters	Not applicable
par.path; par.yleng	Path of the AFM image that is used for the generation of the geometry	Not applicable

A.2 Output variables & preprogrammed plots

The list of output variables is given in 3 tables and is sorted by the categories main results (table A.5), plot relevant variables (table A.6) and miscellaneous variables (table A.7). It is important to note that there are several structural arrays containing secondary variables that are mostly irrelevant to users merely interested in using the DDA program. These structural arrays will only be discussed very briefly. Additionally, several preprogrammed plots are available to visualize the data. An example of every preprogrammed plot with a short explanation is shown subsequently to the tables.

Table A.5: Main results output variables

Variable name	Description
X, Y, Z	Coordinates of the grid positions in m
E	A vector of size Nx3 containing the electric field vector (relative to the incident field); E(:,1) is the x-component; E(:,2) the y-component; E(:,3) is the z-component
Eabs	Absolute values of E (at every position)
distv	Is generated when the par.evaldist flag is set; contains the distances, where the average field strength are evaluated.
Eabsmean	Is generated when the par.evaldist flag is set; contains the average field strength as a function of distance from the surface
Eabs2mean	Is generated when the par.evaldist flag is set; contains $\langle \lvert E^2 \rvert \rangle$ as a function of distance from the surface
Eabs4mean	Is generated when the par.evaldist flag is set; contains $\langle \lvert E^4 \rvert \rangle$ as a function of distance from the surface
result_dda	Structural array containing several secondary results and parameters such as the scattering, absorption and excitation cross sections; the termination condition of the iterative solver (relative residuum reached, number of iterations done and flag denoting why the solver stop) and the starting guess of the iterative solver

Table A.6: Plot relevant variables

Variable name	Description
Xdi, Ydi, Zdi	Coordinates of the dipoles used for the "dipole plot" in m
Xsurf, Ysurf, Zsurf	Coordinates of the surface in the "AFM plot"
results_plotref	Structural array containing the information necessary to generate the preprogrammed plots that are created if the par.plotint flag is set; Feeding this variable into the makeplot.m function (see appendix x) will recreated the plots (if they have been close by accident for example)
results_makeplot	Structural array containing the coordinates of the interpolated grids for the plots generated by makeplot.m

Table A.7: Miscellaneous variables

Variable name	Description
cdate	Contains the date and time the simulation finished
FileName	Contains the path the results were automatically saved to if the par.save_Ind flag is set
start_path	Contains the path of the main DDA program and is necessary for the program to located subroutines
par	Structural array containing all the input parameters
var	Structural array containing secondary variables that were generated and used for the calculations such as the polarizability vector; the incident field vector or the polarizations calculated by the iterative solver

There are 3 categories of preprogramed plots that can be generated by setting different flags in the input parameters. The flag par.plotgeometry will generate the two plots shown in figures A.1 and A.2, that show the surface as defined by the function "AFM" (see chapter 3.2.5) and the dipole positions.

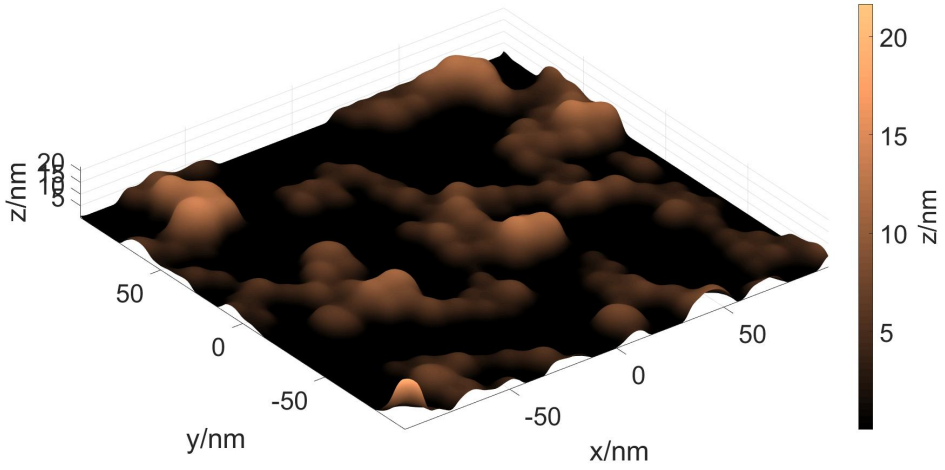

Figure A.1: Preprogramed plot of the function "AFM" that can be generated by setting the par.plotgeometry flag

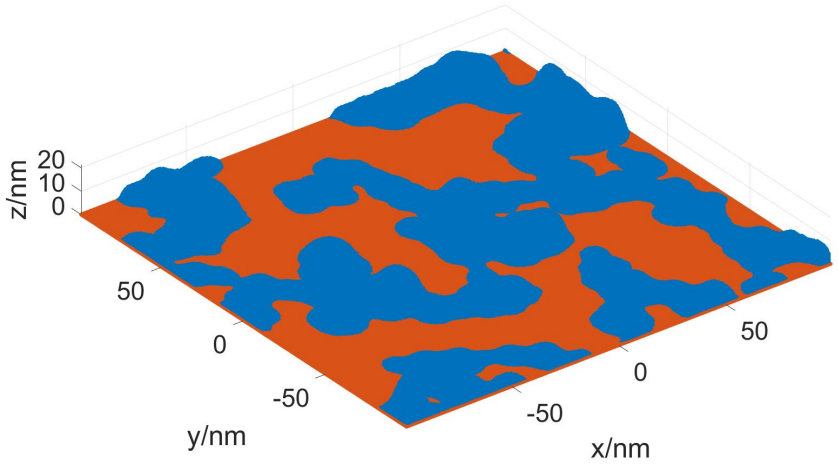

Figure A.2: Preprogramed plot of the dipole positions that can be generated by setting the par.plotgeometry flag

There are 3 plots that are generated if the par.evaldist flag is set. These plots show the average electric field strength, the average field intensity and the average of the E^4 approximation for the SERS intensity as a function of distance from the surface. Examples of these plots are shown in figure A.3-5.

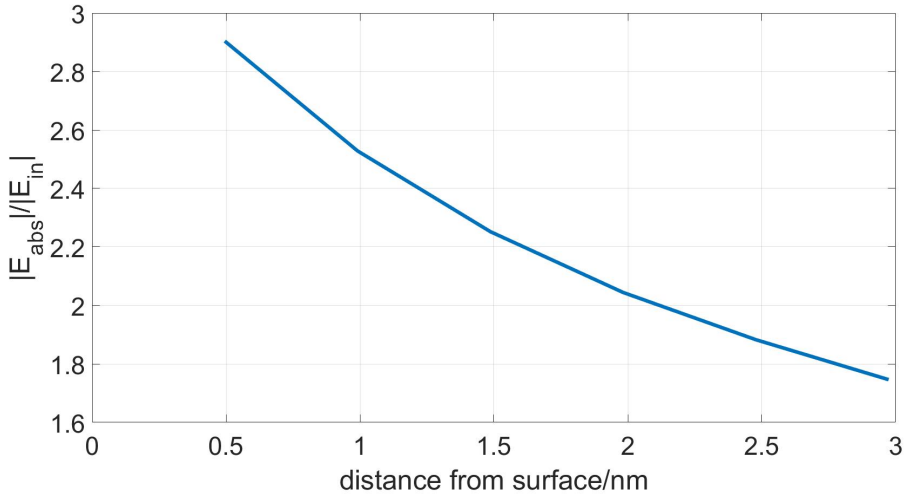

Figure A.3: Example of the plot of the electric field strength that can be generated by setting the par.evaldist flag

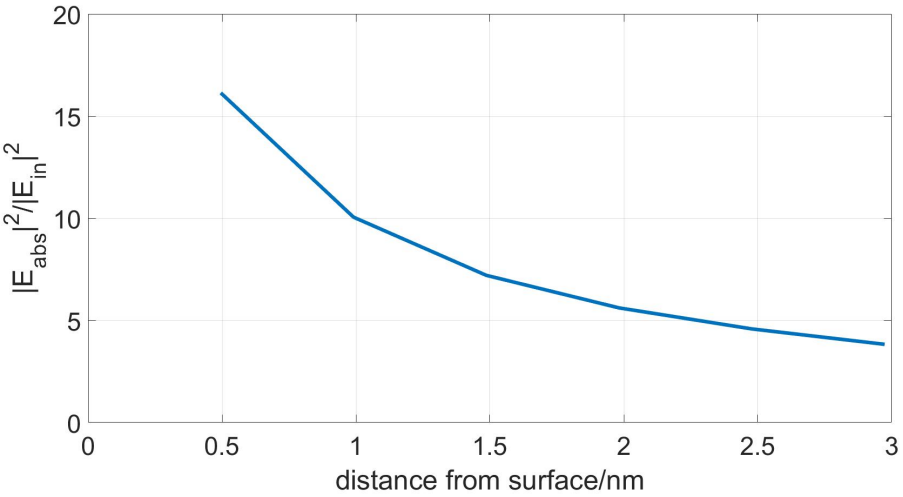

Figure A.4: Example of the plot of the average field intensity that can be generated by setting the par.evaldist flag

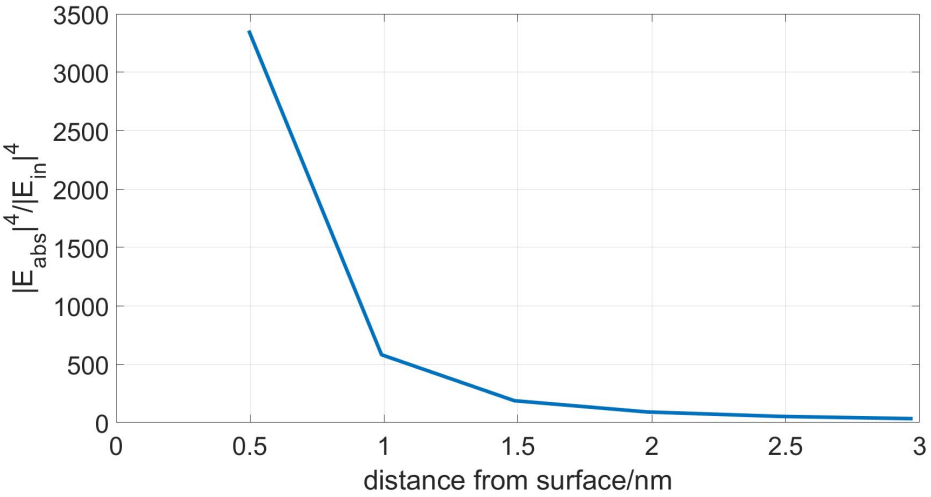

Figure A.5: Example of the plot of the average E^4 approximation for the SERS intensity that can be generated by setting the par.evaldist flag

Finally, three plots that summarize the results of the electric field calculation can be generated by setting the par.plotint flag. The first plot shows an overview of the results by plotting the electric field strength at three cross section through the center of the simulated volume and also the relative residuum that was achieved by the iterative solver as a function of the iterations (Fig. A.6). The second and third plot show a surfaceplot of

the electric field strength at the distance specified by the parameter par.dist from the surface. One of the plots shows the variation of the field strength across the full surface (Fig. A.7), and the other shows the results after the boundaries of the simulation have been cropped (Fig. A.8; reduction of boundaries see Fig. 3.19).

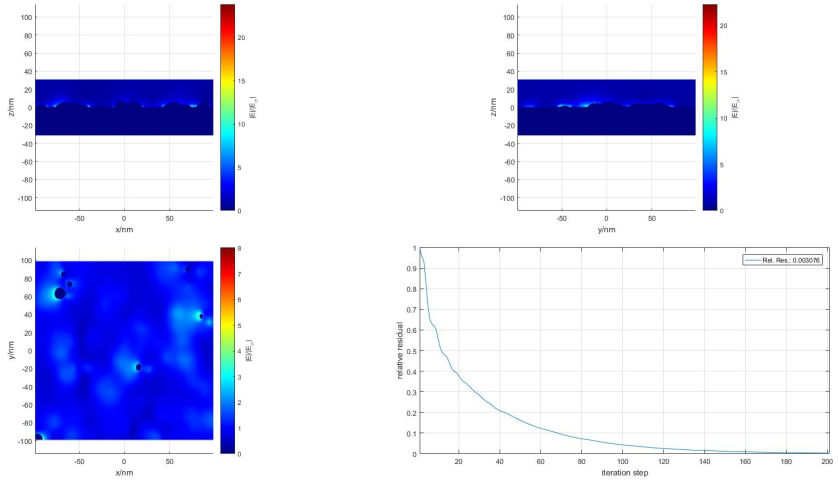

Figure A.6: Overview plots generated by setting the par.plotint flag. The electric field strength at three cross sections through the center of the simulation and the development of the relative residuum (bottom right) are shown

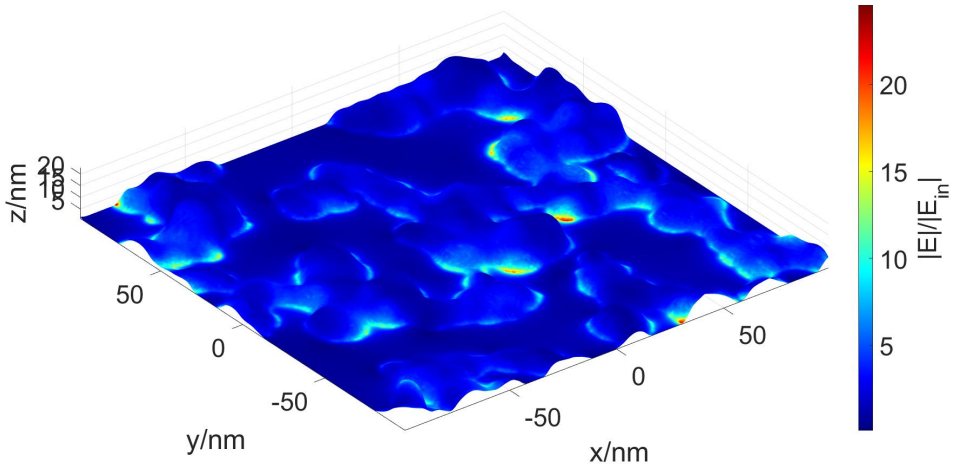

Figure A.7: Plot of the electric field strength at a distance specified by par.dist from the surface. The simulation across the full area is shown. This plot is generated by setting the par.plotint flag

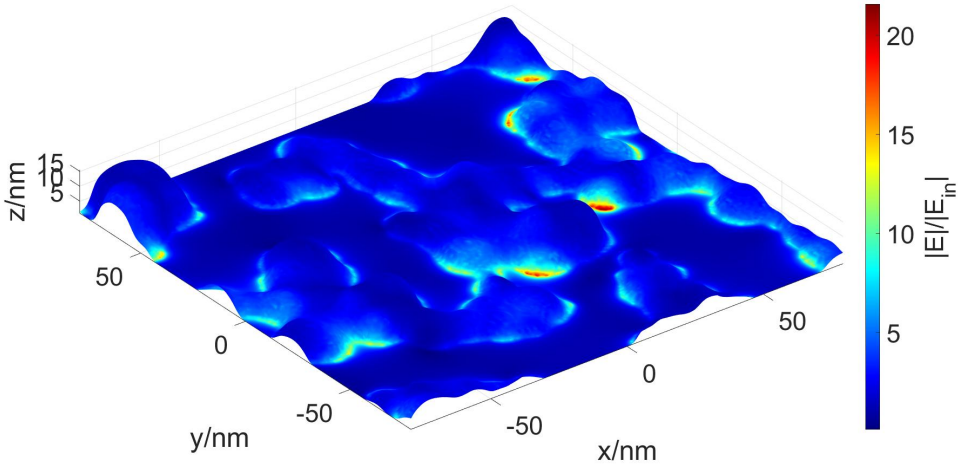

Figure A.8: Plot of the electric field strength at a distance specified by par.dist from the surface. Only the area after the cropping of the boundaries (see fig. xy) is shown. This plot is generated by setting the par.plotint flag

A.3 Source code DDA program

The source code of the DDA program that was developed as part of this thesis is shown on the following pages. Every subsection in this chapter shows one function or sub-function of the develop script. Starting with the run file the subsections are ordered in the same order as they appear in the program and all the subsections are named after the file name of the specific function in question, as this will be the same name as the function-name that appears in the code. In the interest of clarity only files that are central to the operation of the program or are discussed in this thesis elsewhere are shown. Smaller sub-function that perform either secondary or trivial tasks are omitted.

A.3.1 Run file

```
%%%%%Start commands to create a clean workspace%%%%%%%%%%%%%%

close all
clear all
clc

%%%%%%%%%%%%%%%%%%%%%%%%%%%%%%%%%%%%%%%%%%%%%%%%%%%%%%%%%%%%%%%%
%Adding all subfolders containing subroutines to the programm

start_path = fileparts(which(mfilename));
addpath(genpath(start_path))

%%%%%%%%%%%%%%%%%%%%%%%%%%%%%%%%%%%%%%%%%%%%%%%%%%%%%%%%%%%%%%%%

clc
disp('Initializing...')

%%%%%%%%%%%%%%%%%%%%%%%%%%%%Parameter%%%%%%%%%%%%%%%%%%%%%%%%%%
%%%%%%%%%%%%%%%%%Specific to the simulation%%%%%%%%%%%%%%%%%%%

par.nx=24;                          %%%Discretization steps in x
par.ny=24;                          %%%Discretization steps in y
par.nz=24;                          %%%Discretization steps in z

par.xlimit=500.*10^-9; %Maximum size of the simulation in x/m
par.ylimit=500.*10^-9; %Maximum size of the simulation in y/m...
     (Maximum size of the simulation in z is automatically ...
    determined)


```

```
29 par.x0=0.*10^-9; %zeros position in x/m (relevant for large ...
       AFM images)
30 par.y0=0.*10^-9; %zeros position in y/m (relevant for large ...
       AFM images)
31
32
33 par.maxit=1;     %Maximum number of outer iteration in the ...
       gmres-routine
34 par.tol=10^-7;   %Minimal residual goal of the gmres-routine
35 par.order=0;     %Order of the initial guess vector 0=all ...
       zero vector
36 par.points=0;    %1=final fields are calculated pointwise; ...
       not FFT
37 par.gm=1;        %Maximum number of inner iteration in the ...
       gmres-routine
38 par.IT=[1,5,20]; %[x,y,z] x=1 integrated tensor is used; y ...
       depth of off diagonals fully integrated; z numerical ...
       accuracy parameter of the integral
39
40 par.pad_fft=1;   %Use zeropadding to accelerate the FFT (1=...
       true)
41 par.Cscat_ex=0;  %Calculate Cscat using the independent ...
       formular not the simple Cscat=Cext-Cabs (1=true)
42
43 %%%%%%%%%%%%%%%%%%%%%%%%%%%%%%%%%%%%%%%%%%%%%%%%%%%%%%%%%%%%%%%%
44 %%%%%%%%%%%%%data treatmeant parameter%%%%%%%%%%%%%%%%%%%%%%%%%
45
46 par.rx=4;               %Interpolated resolution in x in the ...
       plots
47 par.ry=4;               %Interpolated resolution in y in the ...
       plots
48 par.rz=4;               %Interpolated resolution in z in the ...
       plots
49 par.plotgeometry=1;     %Makes a plot of the geometry with ...
       the dipoles marked as *
50 par.plotint=1;          %Makes a couple of predefined ...
       standard plots of the field intensities
51 par.evaldist=0;         %Makes a plot evaluating the average ...
       field strenght as a function of distance from the surface
52 par.null=1;             %Sets the internal fields to zero in ...
       the field intensitiy plots for clarity
53 par.Mieel=0;            %Starts a test run using Mie Theroy
54 par.save_Ind=0;         %Automatically saves all results and ...
       plots
55
56
57 %%%%%%%%%%%%%%%%%%%%%%%%%%%%%%%%%%%%%%%%%%%%%%%%%%%%%%%%%%%%%%%%
58 %%%%%%%%%%%%%%%%%%%%physical parameters%%%%%%%%%%%%%%%%%%%%%%%%%
59
```

```
60 par.lambda=633.*10^-9;      %wavelength of the incident field
61 par.m_media=1;              %refractive index of the ...
       background
62 par.layer=[0,SiO2_eps(par.lambda.*10^9),par.xlimit,par.ylimit...
       ,-5.*10^-9]; %[x,y,par.xlimit,par.ylimt,z] x=1 puts a ...
       dielectric layer on top of the substrate; y dielectric ...
       constant of that layer; z thickness of that layer (from 0 ...
       to z)
63 par.substrat_quasi=[1,SiO2_eps(par.lambda.*10^9)]; %[x,y] x=1...
        simulated a substrate of dielectric constant y in the ...
       quasistatic approach
64 par.eps=Au_eps(par.lambda.*10^9);% dielectirc constant of the...
        dipoles
65 par.E0=[1,0,0];                  % polarization of the ...
       incident field
66
67 %%%%%%%%%%%%%%%%%%%%%%%%%%%%%%%%%%%%%%%%%%%%%%%%%%%%%%%%%%%%%%%%
68 %%%%%%%%%%%%%%%%%%%%%%%%%%%%%loadAFM?%%%%%%%%%%%%%%%%%%%%%%%%%%
69
70 par.loadAFM=1;                % load an AFM image for the ...
       geometry (default=sphere)
71 par.hAFM=0.*10^-9;            % hight of the lowest point in ...
       the AFM image
72 par.Circ=[10,0,0,0].*10^-9; % defines dimensions of the ...
       default sphere (radius+x,y,z-center)
73 par.xleng=500.*10^-9;        % side length of the AFM image in...
        x/m
74 par.yleng=500.*10^-9;        % side length of the AFM image in...
        y/m
75 par.path='E:\14249_Diss_Fitzek\Computerskripten\Simulationen\...
       Matlab\DDA\Imput\Si_Au17_CundSi_Au20_A\...
       Si_Au20_A_Tap150_020_corrected.txt'; % Path of the AFM ...
       image
76
77 [par.limitx,par.limity,par.limitz,par.AFM] = getAFM(par); % ...
       subroutine to load the AFM image with the correct ...
       dimensions
78
79 %%%%%%%%%%%%%%%%%%%%%%%%%%%%%%%%%%%%%%%%%%%%%%%%%%%%%%%%%%%%%%%%
80 %%%%%%%%%%%%%%%%%%%%%%%%%%%%%DDA solver%%%%%%%%%%%%%%%%%%%%%%%%%
81
82 [E,Eabs,X,Y,Z,result_dda] = DDAcore(par); %Calls main DDA-...
       programm
83 par.dist=2*result_dda.d(1);               %defines default ...
       distance parameter for certain evaluations
84
85 %%%%%%%%%%%%%%%%%%%%%%%%%%%%%%%%%%%%%%%%%%%%%%%%%%%%%%%%%%%%%%%%
86 %%%%%%%%%%%%%%%%Mie testrun subroutines %%%%%%%%%%%%%%%%%%%%%%%%
87
```

```
88 if and(par.Mieel==1,par.loadAFM==0)
89
90     clc
91     disp('Evaluating errors...')
92 [result_mie] = Mieelf(X,Y,Z,E,Eabs,result_dda,par); %%%Calls ...
       subroutine to evaluate the Errors relative to Mie Theory
93 elseif and(par.plotint==1,par.loadAFM==1)
94
95 %%%%%%%%%%%%%%%%%%%%%%makes standard plots%%%%%%%%%%%%%%%%%%%%%%
96
97     clc
98     disp('Making plots...')
99 [results_plotref] = plotrefine(result_dda,par,Eabs,X,Y,Z); % ...
       Generates data for the standard intensity plots
100
101 %%%%%%%%%%%%%%%%%%%%%%%%%%%%%%%%%%%%%%%%%%%%%%%%%%%%%%%%%%%%%%%%%%%
102 %%%%%%%%%%%%%%%%%%%%Plot algorithem conversion%%%%%%%%%%%%%%%%%%%%
103
104 [result_makeplot] = makeplot(results_plotref,result_dda,par);...
        %Makes the standard plots
105 end
106
107 clc
108 if and(par.evaldist==1,par.loadAFM==1)
109 [distv,Eabsmean,Eabs2mean,Eabs4mean] = Evaldist(X,Y,Z,Eabs,...
       par,result_dda); %Subroutine evaluating the distance ...
       dependents of the field intensities
110 end
111 if par.plotgeometry==1
112     clc
113      disp('Ploting geometry...')
114 [Xdi,Ydi,Zdi,Xsurf,Ysurf,Zsurf] = plotgeo(X,Y,Z,result_dda,...
       par); %Subroutine generating some standard plots of the ...
       geometry
115 end
116
117 %%%%%%%%%%%%%%%%%%%%%%%%%%%%%%%%%%%%%%%%%%%%%%%%%%%%%%%%%%%%%%%%%%%
118 %%%Save routine that automatically saves all data and plots%%
119
120 if par.save_Ind==1
121     clc
122     disp('Saving results...')
123 [FileName,PathName,FilterIndex] = uiputfile('.mat');
124 if FileName ~=0
125 cdate=datestr(now,'_yyyy_mm_dd_HHMM');
126 mkdir([PathName,FileName(1:end-4),cdate]);
127 save([PathName,FileName(1:end-4),cdate,'\',FileName(1:end-4),...
       cdate,'.mat']);
128
```

```
handles=findall(0,'type','figure');
for khand=1:numel(handles)
   hand=handles(khand);
   namefig=get(hand,'name');
   saveas(hand,[PathName,FileName(1:end-4),cdate,'\',FileName...
      (1:end-4),cdate,'_',namefig,'.fig']);
end
end
end
clc

%%%%%%%%%%%%%%%%%%%%%%%%%%%%%%%%%%%%%%%%%%%%%%%%%%%%%%%%%%%%%%%%%%%%%%%
%%%%%%%%%%%%%%%%%%%%%%%%END%%%%%%%%%%%%%%%%%%%%%%%%%%%%%%%%%%%%%%%%%%%
```

A.3.2 getAFM.m

```
function  [limitx,limity,limitz,AFM] = getAFM(par)
%This function generates the AFM model for the simulates
if par.loadAFM==1
%The AFM image is turned into a surface function
M=load(par.path);
sM=size(M);
[X,Y]=meshgrid(((0.5:(sM(1)-0.5))-sM(1)./2)./sM(1).*-par....
   xleng,((0.5:(sM(2)-0.5))-sM(2)./2)./sM(2).*-par.yleng);
AFM=TriScatteredInterp(Y(:)-par.x0,X(:)-par.y0,M(:));
Ix=and(X(:)>=-par.xlimit./2,X(:)<=par.xlimit./2);
Iy=and(Y(:)>=-par.ylimit./2,Y(:)<=par.ylimit./2);
Ixy=and(Ix,Iy);
AFM=TriScatteredInterp(X(Ixy),Y(Ixy),AFM(X(Ixy),Y(Ixy))+par....
   hAFM);
%Possible values below zero in the AFM function are removed
AFMhelp=AFM(X(Ixy),Y(Ixy));
IAFM0=AFMhelp<=0;
AFMhelp(IAFM0)=0;
AFM=TriScatteredInterp(X(Ixy),Y(Ixy),AFMhelp);

%The limits of the simulation are determined
limitx=[min(X(Ixy)),max(X(Ixy))];
limity=[min(Y(Ixy)),max(Y(Ixy))];
limitz=[0,max(AFM(X(Ixy),Y(Ixy)))];

%An extra dipole layer is added if enabled
if  par.layer(1)==1
    limitz=[par.layer(5),max(abs(M(:)))];
end

%Dummy variables are putout if the AFM model is not required
else
```

```
    limitx=0;
    limity=0;
    limitz=0;
    AFM=0;
end
end
```

A.3.3 DDAcore.m

```
function [E,Eabs,X,Y,Z,result_dda] = DDAcore(par)
%This functions calls a bunch of subroutines and outputs all ...
   the main results

%This Function generates some trivial parameters of the ...
   scattering problem
[result_dda.n,result_dda.k,result_dda.dmin,result_dda.k0] = ...
   getpar(par);

%This function generates the incident filed and the geometry
[var.I,var.Alpha,var.Ein,result_dda.d,result_dda.N,result_dda...
   .m0,var.Ia,var.Is,var.Elokor1,var.xv,var.yv,var.zv] = ...
   IAlpha(result_dda,par);

%This function calculates the Matrix A and solves the ...
   scattering problem for the polarizations
[result_dda.Cext,result_dda.Cabs,result_dda.Cscat,result_dda....
   Pzestart,result_dda.flag,result_dda.relres,result_dda.iter...
   ,result_dda.resvec,var.Pze] = sloveDDA(result_dda,par,var)...
   ;

%This function calculates the nearfields from the ...
   polarizations on an extended grid
[E,Eabs,result_dda.xlimN,result_dda.ylimN,result_dda.zlimN,X,...
   Y,Z] = NearCalc(result_dda,par,var);
end
```

A.3.4 getpar.m

```
function [n,k,dmin,k0] = getpar(par)
%Some trivial physical parameters are calculated
n=[par.nx,par.ny,par.nz];
    if par.substrat_quasi(1)==1
        n=[par.nx,par.ny,2.*par.nz];
    end
k=[0,0,2.*pi./par.lambda.*par.m_media];
dmin=1./k.*abs(sqrt(par.eps));
```

```
k0=[0,0,2.*pi./par.lambda];
end
```

A.3.5 IAlpha.m

```
function [I,Alpha,Ein,d,N,m0,Ia,Is,Elokor1,xv,yv,zv] = IAlpha...
    (result_dda,par)
%This generates the geometry, polarizability vector and ...
    incident field
%Maximum dimensions are determined
nx=result_dda.n(1);
ny=result_dda.n(2);
nz=result_dda.n(3);
clc
%Tight grid by determining d is build
disp('Tightening grid...')
[d,m0] = dtight(nx,ny,nz,par);

%The maximum value of the z-dimension is determined depending...
     on wheater a sphere, AFM iamge, quasistatic substrate and...
    /or extra dipole layer is used
xv=-ceil(nx./2):ceil(nx./2);
yv=-ceil(ny./2):ceil(ny./2);
zv=-ceil(nz./2):ceil(nz./2);
if par.loadAFM==1
  zv=0:ceil(nz);
  if or(par.layer(1)==1,par.substrat_quasi(1)==1)
    zv=-ceil(nz./2):ceil(nz./2);
  end
end


%Makes the coordinate grid
[xM,yM,zM]=meshgrid(xv,yv,zv);
xv=xM(:).*d(1)+m0(1);
yv=yM(:).*d(2)+m0(2);
zv=zM(:).*d(3)+m0(3);
N=numel(xv);

%Calculates the polarizability with/without extra dipole ...
    layer
[alpha,elokor1]=getalpha(d,result_dda.k0,result_dda.k,par);
if par.layer(1)==1
   [alphasub,elokor1sub] = getalphasub(d,result_dda.k0,...
      result_dda.k,par.m_media,par.layer,par);
end
clc
disp('Getting polarizabilities...')
```

```
%Generates a vector marking all existing dipole positions
[I,Ia,Is,~,~,~,~,~,~] = getInosurf(x,y,z,par);
%Generates the polarizability vector with/without extra ...
   dipole layer
if par.layer(1)==1
Alpha=(Ia./alpha+Is./alphasub);
Elokor1=ones(size(Alpha));
Elokor1(Is)=elokor1sub;
Elokor1(Ia)=elokor1;
else
Alpha=I./alpha;
Elokor1=ones(size(Alpha));
Elokor1(I)=elokor1;
end
%Generates the incident field with/without quasistatic ...
   substrate
Ein = getEin(xv,yv,zv,N,I,result_dda.k,par.m_media,1,par.E0,...
   par.substrat_quasi,m0);
end
```

A.3.6 dtight.m

```
function [d,m0] = dtight(nx,ny,nz,par)
%This function automatically generates a discretiztation ...
   stepsize that thigly fits the problem
%Here a couple of strat guesses are made
if par.loadAFM ==1
    dx=abs(par.limitx(1)-par.limitx(2))./nx;
    dy=abs(par.limity(1)-par.limity(2))./ny;
    dz=abs(par.limitz(1)-par.limitz(2))./nz;
    d=[dx,dy,dz];
    mx=0;
    my=0;
    mz=0;
    if par.layer(1)==1
       mz= par.limitz(1)+ceil(nz./2).*max(d(:));
    end
    if par.substrat_quasi(1)==1
        mz= par.limitz(1);
    end
    m0=[mx,my,mz];
else
dint=65.*10^-9;
v=-150:150;
[x,y,z]=meshgrid(v,v,v);
x=x(:);
y=y(:);
z=z(:);
```

```
26
27 I=zeros(size(x));
28 kw=1;
29 %Here the start guesses are optimized
30 while sum(I(:)) < 10;
31     dint=dint./(kw.^3);
32     dhx=dint;
33     dhy=dint;
34     dhz=dint;
35     I = getInosurf(x.*dhx,y.*dhy,z.*dhz,par);
36     kw=kw+1;
37     if kw>=11
38        break
39     end
40 end
41 ds=[2,1.5,1.2,1.05,1];
42
43 for kf=1:5
44 I=logical(I);
45 xmin=min(x(I));
46 ymin=min(y(I));
47 zmin=min(z(I));
48 xmax=max(x(I));
49 ymax=max(y(I));
50 zmax=max(z(I));
51 dguesx=dhx.*abs(xmax-xmin)./(nx-2);
52 dguesy=dhy.*abs(ymax-ymin)./(ny-2);
53 dguesz=dhz.*abs(zmax-zmin)./(nz-2);
54 dhx=ds(kf).*dguesx;
55 dhy=ds(kf).*dguesy;
56 dhz=ds(kf).*dguesz;
57 I = getInosurf(x.*dhx,y.*dhy,z.*dhz,par);
58 end
59 d=[dhx,dhy,dhz];
60 m0=[par.Circ(2)-0.5.*max(d(:)),par.Circ(3)-0.5.*max(d(:)),par...
       .Circ(4)-max(d(:))./2];
61 % Here the guesse are modified in case there is an extra ...
       dipole layer or quasistatic substrate
62     if par.substrat_quasi(1)==1
63         m0=[par.Circ(2),par.Circ(3),par.Circ(4)-(nx)./2.*max(...
               d(:))];
64     end
65
66
67 if par.layer(1)==1
68     m0(3)=0;
69     if par.substrat_quasi(1)==1
70         m0=[par.Circ(2),par.Circ(3),par.layer(5)-max(d(:))];
71     end
```

```
72 end
73 end
74 %Here a cubic grid is ensured for simplisity
75 d=[1,1,1].*max(d);
76 end
```

A.3.7 getInosurf.m

```
1  function [I,Ia,Is,a1,b1,c1,mx1,my1,mz1] = getInosurf(x,y,z,...
       par)
2  %This function determines if a vector of dipole positions x,y...
       ,z is occupied or not
3  %AFM function laoded
4  if par.loadAFM==1
5  AFM=par.AFM;
6  I=zeros(size(x));
7  %Is dipole inside the bounding box
8  Ix = and(x>=par.limitx(1), x<=par.limitx(2));
9  Iy = and(y>=par.limity(1), y<=par.limity(2));
10 %Is the dipole above 0
11 Iz = z>0;
12 Ixz=and(Ix,Iz);
13 Ixyz = and (Ixz,Iy);
14 %Is the dipole below the substrate
15 I(Ixyz)=z(Ixyz)-AFM(x(Ixyz),y(Ixyz))<=0;
16 %Vector with 1 at every existing dipole position
17 I=logical(I);
18 %Dummy legacy variables
19 a1=0;
20 b1=0;
21 c1=0;
22 mx1=0;
23 my1=0;
24 mz1=0;
25 else
26 %In this case a sphere is used for testing purposese because ...
       par.loadAFM=0
27 a1=par.Circ(1);
28 b1=par.Circ(1);
29 c1=par.Circ(1);
30 mx1=par.Circ(2);
31 my1=par.Circ(3);
32 mz1=par.Circ(4);
33
34 Iep1=Ielip(x,y,z,a1,b1,c1,mx1,my1,mz1);
35 I=Iep1;
36
37 %This takes into account an additional dipole layer if ...
```

```
    enabled
if par.layer(1) == 1
      I=and(I,z>=0);
end
end
if par.layer(1)==1
    Isx=par.layer(3)>=abs(x);
    Isy=par.layer(4)>=abs(y);
    Isz=and(z<=0,z>=par.layer(5));
    Is=and(and(Isx,Isy),Isz);
    Ia=I;
    I=or(Is,Ia);
else
    Is=0;
    Ia=0;
end
end
```

A.3.8 getalpha.m

```
function [alpha,Elokor] = getalpha(d,k0,k,par)
%Calculation of the polarizability according to the IT ...
    formulars
if par.IT(1)==1
i=1i;
A=norm(k0).^2./(norm(k).^2.*4.*pi).*(par.eps-par.m_media.^2);
dm=(d(1)+d(2)+d(3))./3;

F = @(w,th) (((-norm(k).^2.*(1-exp(i.*w.*dm./2))-w.^2.*exp(i...
    .*w.*dm./2))./w).*sin(sqrt(norm(k).^2-w.^2).*cos(th).*dm...
    ./2).*sin(sqrt(norm(k).^2-w.^2).*sin(th).*dm./2))./((norm(...
    k).^2-w.^2).*cos(th).*sin(th));

G = @(be,th) (((norm(k).^2-(norm(k).^2+be.^2).*exp(-be.*dm...
    ./2))./be).*sin(sqrt(norm(k).^2+be.^2).*cos(th).*dm./2).*...
    sin(sqrt(norm(k).^2+be.^2).*sin(th).*dm./2))./((norm(k)...
    .^2+be.^2).*cos(th).*sin(th));

Int1=integral2(F,0,norm(k),0,pi./2,'absTol',10^-20,'relTol'...
    ,10^-20);
Int2=integral2(G,0,Inf,0,pi./2,'absTol',10^-13,'relTol'...
    ,10^-8);
Gint=16./pi.*(Int1+Int2);
alpha=A./(1-Gint.*A);
Elokor=1./(1-Gint.*A);

else
%Calculation of the polarizability according to the LDR ...
```

```
    formulars if the IT is no enabled
i=1i;
V=d(1).*d(2).*d(3);
b1=-1.891531;
b2=0.1648469;
b3=-1.7700004;
S=0;
M=(-1).*(b1+par.eps.*b2+par.eps.*b3.*S).*((k0*d').^2)-(2./3)...
    .*i.*(k0*d').^3;
alpha=V.*(par.eps-par.m_media.^2)./(4.*pi.*(1+(par.eps-par....
    m_media.^2)./(3.*par.m_media.^2))-M.*(par.eps-par.m_media...
    .^2));

Elokor=4.*pi.*alpha./(V.*(par.eps-par.m_media.^2));
end
end
```

A.3.9 getEin.m

```
function Ein = getEin(x,y,z,N,I,k,m_media,zEout,E0,...
    substrat_quasi,m0)
%This function generates the incident field and its ...
    reflection if necessary
i=1i;
k=-k;

%Incident plane wave
Ein=zeros(3*N,1);
Ein(1:N)=exp(i.*(k(1).*x+y.*k(2)+z.*k(3))).*E0(1);
Ein((N+1):2*N)=exp(i.*(k(1).*x+y.*k(2)+z.*k(3))).*E0(2);
Ein((2*N+1):3*N)=exp(i.*(k(1).*x+y.*k(2)+z.*k(3))).*E0(3);

%Reflection of the incident plane wave on the quasitatic ...
    substrate
if substrat_quasi(1)==1
    n1=m_media;
    n2=real(sqrt(substrat_quasi(2)));
    R=(n1-n2)./(n1+n2);

    Ein(1:N)=exp(i.*(k(1).*x+y.*k(2)+z.*k(3))).*E0(1)+E0(1).*R...
        .*exp(-i.*2.*k(3).*m0(3)).*exp(i.*(k(1).*x+y.*k(2)-z.*k...
        (3)));
    Ein((N+1):2*N)=exp(i.*(k(1).*x+y.*k(2)+z.*k(3))).*E0(2)+E0...
        (2).*R.*exp(-i.*2.*k(3).*m0(3)).*exp(i.*(k(1).*x+y.*k...
        (2)-z.*k(3)));
    Ein((2*N+1):3*N)=exp(i.*(k(1).*x+y.*k(2)+z.*k(3))).*E0(3)+...
        E0(3).*R.*exp(-i.*2.*k(3).*m0(3)).*exp(i.*(k(1).*x+y.*k...
        (2)-z.*k(3)));
```

```
21
22
23 end
24
25 %Removing of the incident plane wave on none occupied grid ...
      positions
26 if zEout==1
27 Ih=repmat(I,3,1);
28 Ein(~Ih)=0;
29 end
30
31 end
```

A.3.10 solveDDA.m

```
1  function [Cext,Cabs,Cscat,Pzestart,flag,relres,iter,resvec,...
       Pze] = sloveDDA(result_dda,par,var)
2  %This function solves the core scattering problem
3  nx=result_dda.n(1);
4  ny=result_dda.n(2);
5  nz=result_dda.n(3);
6  %The Matrix A is created with/without IT aproach
7  if par.IT(1)==1
8      clc
9      disp('Integrating tensor...')
10 [var.A,var.Ih,var.pad]=conAIT(nx,ny,nz,result_dda.k,...
       result_dda.d,result_dda.k0,par);
11 else
12     clc
13     disp('Calculating tensor...')
14 [var.A,var.Ih,var.pad]=conA(nx,ny,nz,result_dda.k,result_dda....
       d,result_dda.k0,par);
15 end
16
17 clc
18 disp('Solving Equations...')
19 %A function is defined that calculates the vector matrix ...
       product
20 fze=@(x)  AtimesP(x,result_dda.N,var,par,result_dda);
21 %A start guess for the polarization vector is made if desired
22 [Pzestart] = cgsstartguess(result_dda.N,par.order,var);
23 %The matlab intern routine gmres solves the problem; if gmres...
       is deactivated bicstab is used
24 if par.gm >0
25 [Pze,flag,relres,iter,resvec] = gmres(fze,var.Ein,ceil(par.gm...
       ),par.tol,par.maxit,[],[],Pzestart);
26 else
27 [Pze,flag,relres,iter,resvec]=bicgstab(fze,var.Ein,par.tol,...
```

```
    par.maxit,[],[],Pzestart);
end
%A vector showing the convergance of the calculation as a ...
    function of solver steps is generated
resvec=resvec./norm(var.Ein);
%The crossections are calcualted by a subroutine
[Cext,Cabs,Cscat] = CalcC(result_dda.k,result_dda.d,par,var,...
    Pze);

%The results are stored for later use by the function ...
    NearfieldCalc
if par.points==1
else
I1=repmat(var.I,3,1);

Pze=Pze(I1);
end
end
```

A.3.11 conAIT.m

```
function [A,Ih,pad] = conAIT(nx,ny,nz,k,d,k0,par)
%%%This function constructs the matrix A using the limited IT...
     approach
%Gets some parameteres with regard to the accuracy of the ...
    nummerical integration
i=1i;
depth=par.IT(2);
acc=par.IT(3);

%A large grid for the calculation is defined
xv=-nx:nx;
yv=-ny:ny;
zv=-nz:nz;
[X,Y,Z]=meshgrid(xv,yv,zv);
%Dummy variable giving the size of A in one direction
Al=numel(X);
%Dummy variable for zero-padding if enabled
if par.pad_fft==1
pad=2.^nextpow2(Al);
else
     pad=0;
end
%The empty matrix A variable and some support variables are ...
    generated
A=zeros(Al,6);
Ih=zeros(Al,2);
k=sqrt(k*k');
```

```
25 k0=sqrt(k0*k0');
26 %Volume of a singel discretization is generated
27 V=d(1).*d(2).*d(3);
28 %Rearragnement indices for the Ptimesv function are defined
29 Ih(:,1)=and(and(Z(:)>=0,Y(:)>=0),X(:)>=0);
30 Ifirst=find(Ih(:,1),1)-1;
31 Ih(1:(end-Ifirst),2)=Ih((Ifirst+1):end,1);
32 Ih=logical(Ih);
33 %Grid with right size is generated
34 x=d(1).*(-X(:));
35 y=d(2).*(-Y(:));
36 z=d(3).*(-Z(:));
37 %Some variables are cleared to safe memory as the next bid is...
       the most memory intensive of the entire script
38 clear X
39 clear Y
40 clear Z
41
42 %The matrix A is filed with values from the classical ...
      formular without the IT approach
43 A(:,1)=-exp(i.*k.*sqrt(x.^2+y.^2+z.^2))./sqrt(x.^2+y.^2+z.^2)...
      .^3.*(((x.^2+y.^2+z.^2).*k.^2+i.*k.*sqrt(x.^2+y.^2+z.^2)...
      -1)+((3-3.*i.*k.*sqrt(x.^2+y.^2+z.^2)-k.^2.*(x.^2+y.^2+z...
      .^2))./(x.^2+y.^2+z.^2)).*x.^2).*V;
44 A(:,2)=-exp(i.*k.*sqrt(x.^2+y.^2+z.^2))./sqrt(x.^2+y.^2+z.^2)...
      .^3.*(((x.^2+y.^2+z.^2).*k.^2+i.*k.*sqrt(x.^2+y.^2+z.^2)...
      -1)+((3-3.*i.*k.*sqrt(x.^2+y.^2+z.^2)-k.^2.*(x.^2+y.^2+z...
      .^2))./(x.^2+y.^2+z.^2)).*y.^2).*V;
45 A(:,3)=-exp(i.*k.*sqrt(x.^2+y.^2+z.^2))./sqrt(x.^2+y.^2+z.^2)...
      .^3.*(((x.^2+y.^2+z.^2).*k.^2+i.*k.*sqrt(x.^2+y.^2+z.^2)...
      -1)+((3-3.*i.*k.*sqrt(x.^2+y.^2+z.^2)-k.^2.*(x.^2+y.^2+z...
      .^2))./(x.^2+y.^2+z.^2)).*z.^2).*V;
46 A(:,4)=-(exp(i.*k.*sqrt(x.^2+y.^2+z.^2))./sqrt(x.^2+y.^2+z...
      .^2).^3).*((3-3.*i.*k.*sqrt(x.^2+y.^2+z.^2)-k.^2.*(x.^2+y...
      .^2+z.^2))./(x.^2+y.^2+z.^2)).*x.*y.*V;
47 A(:,5)=-(exp(i.*k.*sqrt(x.^2+y.^2+z.^2))./sqrt(x.^2+y.^2+z...
      .^2).^3).*((3-3.*i.*k.*sqrt(x.^2+y.^2+z.^2)-k.^2.*(x.^2+y...
      .^2+z.^2))./(x.^2+y.^2+z.^2)).*x.*z.*V;
48 A(:,6)=-(exp(i.*k.*sqrt(x.^2+y.^2+z.^2))./sqrt(x.^2+y.^2+z...
      .^2).^3).*((3-3.*i.*k.*sqrt(x.^2+y.^2+z.^2)-k.^2.*(x.^2+y...
      .^2+z.^2))./(x.^2+y.^2+z.^2)).*y.*z.*V;
49
50 %Helpful functions for the nummerical integration are ...
      generated
51 gxx=@(rx,ry,rz) exp(i.*k.*sqrt(rx.^2+ry.^2+rz.^2))./sqrt(rx...
      .^2+ry.^2+rz.^2).^3.*(((rx.^2+ry.^2+rz.^2).*k.^2+i.*k.*...
      sqrt(rx.^2+ry.^2+rz.^2)-1)+((3-3.*i.*k.*sqrt(rx.^2+ry.^2+...
      rz.^2)-k.^2.*(rx.^2+ry.^2+rz.^2))./(rx.^2+ry.^2+rz.^2)).*...
      rx.^2);
```

```
52 gyy=@(rx,ry,rz) exp(i.*k.*sqrt(rx.^2+ry.^2+rz.^2))./sqrt(rx...
       .^2+ry.^2+rz.^2).^3.*(((rx.^2+ry.^2+rz.^2).*k.^2+i.*k.*...
       sqrt(rx.^2+ry.^2+rz.^2)-1)+((3-3.*i.*k.*sqrt(rx.^2+ry.^2+...
       rz.^2)-k.^2.*(rx.^2+ry.^2+rz.^2))./(rx.^2+ry.^2+rz.^2)).*...
       ry.^2);
53 gzz=@(rx,ry,rz) exp(i.*k.*sqrt(rx.^2+ry.^2+rz.^2))./sqrt(rx...
       .^2+ry.^2+rz.^2).^3.*(((rx.^2+ry.^2+rz.^2).*k.^2+i.*k.*...
       sqrt(rx.^2+ry.^2+rz.^2)-1)+((3-3.*i.*k.*sqrt(rx.^2+ry.^2+...
       rz.^2)-k.^2.*(rx.^2+ry.^2+rz.^2))./(rx.^2+ry.^2+rz.^2)).*...
       rz.^2);
54
55 gxy=@(rx,ry,rz) (exp(i.*k.*sqrt(rx.^2+ry.^2+rz.^2))./sqrt(rx...
       .^2+ry.^2+rz.^2).^3).*((3-3.*i.*k.*sqrt(rx.^2+ry.^2+rz.^2)...
       -k.^2.*(rx.^2+ry.^2+rz.^2))./(rx.^2+ry.^2+rz.^2)).*rx.*ry;
56 gxz=@(rx,ry,rz) (exp(i.*k.*sqrt(rx.^2+ry.^2+rz.^2))./sqrt(rx...
       .^2+ry.^2+rz.^2).^3).*((3-3.*i.*k.*sqrt(rx.^2+ry.^2+rz.^2)...
       -k.^2.*(rx.^2+ry.^2+rz.^2))./(rx.^2+ry.^2+rz.^2)).*rx.*rz;
57 gyz=@(rx,ry,rz) (exp(i.*k.*sqrt(rx.^2+ry.^2+rz.^2))./sqrt(rx...
       .^2+ry.^2+rz.^2).^3).*((3-3.*i.*k.*sqrt(rx.^2+ry.^2+rz.^2)...
       -k.^2.*(rx.^2+ry.^2+rz.^2))./(rx.^2+ry.^2+rz.^2)).*ry.*rz;
58
59 %The values in A are replaced up to the specified depth by ...
       the integrated values
60 G=zeros([(depth+1).^3,6]);
61
62 IG=1;
63 for indx=0:depth
64     for indy=0:depth
65         for indz=0:depth
66             if indx+indy+indz ==0
67             else
68                 IG=IG+1;
69 xmin=(indx-0.5).*d(1);
70 xmax=(indx+0.5).*d(1);
71 ymin=(indy-0.5).*d(2);
72 ymax=(indy+0.5).*d(2);
73 zmin=(indz-0.5).*d(3);
74 zmax=(indz+0.5).*d(3);
75
76 G(IG,1)=simp3D(gxx,xmin,xmax,ymin,ymax,zmin,zmax,acc,acc,acc)...
       ;
77 G(IG,2)=simp3D(gyy,xmin,xmax,ymin,ymax,zmin,zmax,acc,acc,acc)...
       ;
78 G(IG,3)=simp3D(gzz,xmin,xmax,ymin,ymax,zmin,zmax,acc,acc,acc)...
       ;
79 G(IG,4)=simp3D(gxy,xmin,xmax,ymin,ymax,zmin,zmax,acc,acc,acc)...
       ;
80 G(IG,5)=simp3D(gxz,xmin,xmax,ymin,ymax,zmin,zmax,acc,acc,acc)...
       ;
```

```
81  G(IG,6)=simp3D(gyz,xmin,xmax,ymin,ymax,zmin,zmax,acc,acc,acc)...
        ;
82
83                  end
84              end
85          end
86  end
87
88  Iit=and(and(abs(x./d(1))<=depth,abs(y./d(2))<=depth),abs(z./d...
        (3))<=depth);
89
90  TGit=abs(z(Iit)./d(1))+abs(y(Iit)./d(2)).*(depth+1)+abs(x(Iit...
        )./d(3)).*(depth+1).^2+1;
91  TGit=round(TGit);
92
93
94  A(Iit,1)=-G(TGit,1);
95  A(Iit,2)=-G(TGit,2);
96  A(Iit,3)=-G(TGit,3);
97  A(Iit,4)=-G(TGit,4).*sign(x(Iit)).*sign(y(Iit));
98  A(Iit,5)=-G(TGit,5).*sign(x(Iit)).*sign(z(Iit));
99  A(Iit,6)=-G(TGit,6).*sign(y(Iit)).*sign(z(Iit));
100
101 %Some variables are cleared to safe memory as the next bid is...
        the most memory intensive of the entire script
102 clear G
103 clear TGit
104 clear Iit
105 clear x
106 clear y
107 clear z
108 %Dummy variable for zero-padding if enabled and FFT of A is ...
        precalcualted
109 if par.pad_fft==1
110 B=zeros(pad,6);
111 for k=1:6;
112     B(:,k)=fft(A(:,k),pad);
113 end
114
115 A=B;
116 else
117  B=zeros(size(A));
118 for k=1:6;
119     B(:,k)=fft(A(:,k));
120 end
121
122 A=B;
123 end
124
```

```
125 clear B
126 Ih=logical(Ih);
127 end
```

A.3.12 AtimesP.m

```
1  function [Y] = AtimesP(P,N,var,par,result_dda)
2  %%%%This function calculates the split up part of the vector ...
       product and rearranges the vector in case their is a quasi...
       -static substrate
3
4  %IF constructed that does the quasi-static substrate
5      if par.substrat_quasi(1)==1
6      %Some parameters are generated
7          nz=ceil(result_dda.n(3)./2);
8          eps_sub=par.substrat_quasi(2);
9          nm=par.m_media;
10         Ref=(eps_sub-nm)./(eps_sub+nm);
11
12     %The polarization vector is flip and rearranges to ...
           reflect the quasi-static substrate
13      Px=P(1:N);
14      Px=reshape(Px,[],nz.*2+1);
15      Px(:,1:nz)=-1.*Ref.*fliplr(Px(:,nz+2:end));
16      P(1:N)=Px(:);
17
18
19      Py=P((N+1):2*N);
20      Py=reshape(Py,[],nz.*2+1);
21      Py(:,1:nz)=-1.*Ref.*fliplr(Py(:,nz+2:end));
22      P((N+1):2*N)=Py(:);
23
24
25      Pz=P((2*N+1):3*N);
26      Pz=reshape(Pz,[],nz.*2+1);
27      Pz(:,1:nz)=Ref.*fliplr(Pz(:,nz+2:end));
28      P((2*N+1):3*N)=Pz(:);
29     end
30
31
32
33 %Out put vector set to zero
34 Y=zeros(size(P));
35
36
37 %The individual products are calculated by Atimesv and ...
       arranged accordingly
38 Yh=Atimesv(P(1:N),1,var)+Atimesv(P((N+1):2*N),4,var)+Atimesv(...
```

```
    P((2*N+1):3*N),5,var)+var.Alpha.*P(1:N);
Yh(~var.I)=0;
Y(1:N)=Yh;
Yh=Atimesv(P(1:N),4,var)+Atimesv(P((N+1):2*N),2,var)+Atimesv(...
    P((2*N+1):3*N),6,var)+var.Alpha.*P((N+1):2*N);
Yh(~var.I)=0;
Y((N+1):2*N)=Yh;
Yh=Atimesv(P(1:N),5,var)+Atimesv(P((N+1):2*N),6,var)+Atimesv(...
    P((2*N+1):3*N),3,var)+var.Alpha.*P((2*N+1):3*N);
Yh(~var.I)=0;
Y((2*N+1):3*N)=Yh;
end
```

A.3.13 Atimesv.m

```
function [Y] = Atimesv(v,ai,var)
%%%This function calculates the fundamental vector product ...
    using the FFT
%Function is split up depending if zeropadding is enabled
if var.pad~=0
%FFTs the input vector with the correct positioning
V=zeros(size(var.A(:,ai)));
V(var.Ih(:,2))=v;
fV=fft(V,var.pad);
%Multiplication in Fourier space
fY=var.A(:,ai).*fV;
%Reverse Fourier transformation and correct positioning
Yh=ifft(fY,var.pad);
Y=Yh(var.Ih(:,1));
else
%same as appove without zeropadding
 V=zeros(size(var.A(:,ai)));
V(var.Ih(:,2))=v;
fV=fft(V);
fY=var.A(:,ai).*fV;
Yh=ifft(fY);
Y=Yh(var.Ih(:,1));
end
end
```

A.3.14 CalcC.m

```
function [Cext,Cabs,Cscat] = CalcC(k,d,par,var,Pze)
%%%Calculates the scattering, absorption and extinction cross...
    -section in different ways
%If consturcted to take into account an added dipole layer; ...
```

```
    if it has been enabled
if par.layer(1)==1
I1=repmat(var.Ia,3,1);
Ih=var.Ia;
else
    I1=repmat(var.I,3,1);
Ih=var.I;
end

%Some support vectors
N=numel(var.Alpha(:,1));
k=sqrt(k*k');

%Generating the vectors with the polarization in x,y,z
Px=Pze(1:N);
Py=Pze((N+1):2*N);
Pz=Pze((2*N+1):3*N);

%C extinction is calculated trivially
Cext=4.*pi.*k.*sum(imag(conj(var.Ein(I1)).*Pze(I1)));

%C absorption is calculated trivially
Cabsx=sum(imag(Px(Ih).*conj(var.Alpha(Ih).*Px(Ih))));
Cabsy=sum(imag(Py(Ih).*conj(var.Alpha(Ih).*Py(Ih))));
Cabsz=sum(imag(Pz(Ih).*conj(var.Alpha(Ih).*Pz(Ih))));
Cabs=4.*pi.*k.*((Cabsx+Cabsy+Cabsz)-sum((2./3).*k.^3.*abs(Pze...
    (I1).^2)));

%C scattering is either calculated from Cext and Cabs, which ...
    is the simple way or directly from the polarizations which...
     is the complex approach
if par.Cscat_ex~=1
%C scattering calculated simply
Cscat=Cext-Cabs;
else
%Detailed calculation of Cscat by summing overall scattering ...
    angles
phi=linspace(0,2.*pi,40);
th=linspace(0,pi,40);
[PHI,TH]=meshgrid(phi,th);
NX=sin(TH).*cos(PHI);
NY=sin(TH).*sin(PHI);
NZ=cos(TH);

S=zeros(1,numel(NZ));

for ind=1:numel(NZ)
    NNxx=1-NX(ind).^2;
    NNyy=1-NY(ind).^2;
```

```
48      NNzz=1-NZ(ind).^2;
49
50      NNxy=NX(ind).*NY(ind);
51      NNxz=NX(ind).*NZ(ind);
52      NNyz=NY(ind).*NZ(ind);
53
54      Phase=exp(-1i.*k.*(var.xv.*NX(ind)+var.yv.*NY(ind)+var.zv...
            .*NZ(ind)));
55
56      Vx=(NNxx.*Px(Ih)+NNxy.*Py(Ih)+NNxz.*Pz(Ih)).*Phase(Ih);
57      Vy=(NNxy.*Px(Ih)+NNyy.*Py(Ih)+NNyz.*Pz(Ih)).*Phase(Ih);
58      Vz=(NNxz.*Px(Ih)+NNyz.*Py(Ih)+NNzz.*Pz(Ih)).*Phase(Ih);
59
60      Fx=sum(Vx);
61      Fy=sum(Vy);
62      Fz=sum(Vz);
63
64      S(ind)=abs(Fx.^2+Fy.^2+Fz.^2);
65
66  end
67
68  Cscat(1)=2.*pi.^2.*k.^4./numel(NZ).*sum(S'.*sin(TH(:)));
69
70  end
71  %If the IT approach was used some correction factors are ...
        applied due to the unit convention used for the IT ...
        approach in this script
72  if par.IT(1)==1
73
74  Cabs=4.*pi.*k.*((Cabsx+Cabsy+Cabsz));
75  if par.Cscat_ex~=1
76  Cscat=Cext-Cabs;
77  else
78    Cscat=Cscat.*mean(d(:)).^3;
79  end
80  Cext=Cext.*mean(d(:)).^3;
81  Cabs=Cabs.*mean(d(:)).^3;
82  Cscat=Cscat.*mean(d(:)).^3;
83  end
84
85  end
```

A.3.15 NearCalc.m

```
1   function [E,Eabs,xlimN,ylimN,zlimN,X,Y,Z] = NearCalc(...
        result_dda,par,var)
2   %This function calculates the nearfield a on big grid
3   clc
```

```
4  disp('Calculating Nearfield...')
5
6  %Limits of the big grid are deterimined depending on if a ...
       sphere, AFM image, quasi-static substrate and/or extra ...
       dipole layer are used
7  xlimN=[-ceil(result_dda.n(1).*0.8),ceil(result_dda.n(1).*0.8)...
       ];
8  ylimN=[-ceil(result_dda.n(2).*0.8),ceil(result_dda.n(2).*0.8)...
       ];
9  zlimN=[-ceil(result_dda.n(3).*0.8),ceil(result_dda.n(3).*0.8)...
       ];
10
11 if par.layer(1) ==1
12     xlimN=[-ceil(result_dda.n(1).*0.5),ceil(result_dda.n(1)...
           .*0.5)];
13     ylimN=[-ceil(result_dda.n(2).*0.5),ceil(result_dda.n(2)...
           .*0.5)];
14     zlimN=[-ceil(result_dda.n(3)./2),ceil(result_dda.n(3))...
           .*0.6];
15 end
16 if par.loadAFM ==1
17 xlimN=[-ceil(result_dda.n(1)./2),ceil(result_dda.n(1)./2)];
18 ylimN=[-ceil(result_dda.n(2)./2),ceil(result_dda.n(2)./2)];
19 zlimN=[0,ceil(result_dda.n(3).*1.2)];
20     if or(par.layer(1) ==1,par.substrat_quasi(1)==1)
21         zlimN=[-ceil(result_dda.n(3).*0.6),ceil(result_dda.n...
               (3).*0.6)];
22     end
23 end
24 nx=abs(xlimN(1)-xlimN(2));
25 ny=abs(ylimN(1)-ylimN(2));
26 nz=abs(zlimN(1)-zlimN(2));
27
28 %ConBig is the equivalent of IAlpha on a big gird
29
30 [var.I2,var.Alpha2,var.Ein2,N,X,Y,Z,var.Pze,var.Elokor] = ...
       conBig(xlimN,ylimN,zlimN,result_dda.d,result_dda.k,...
       result_dda.k0,result_dda.m0,par,var);
31
32 %The nearfields are calcualted from the polarization vector ...
       and put into a nice and easy to understand form
33 [E,Eabs] = NearfieldBig(nx,ny,nz,result_dda.k,result_dda.d,N,...
       result_dda.k0,X,Y,Z,par,var);
34 NE=numel(E);
35 Eh=zeros(NE./3,3);
36 Eh(:,1)=E(1:NE/3);
37 Eh(:,2)=E((NE/3+1):2.*NE/3);
38 Eh(:,3)=E((2.*NE/3+1):NE);
39 E=Eh;
```

```
40 end
```

A.3.16 NearfieldBig.m

```
1  function [E,Eabs] = NearfieldBig(nx,ny,nz,k,d,N,k0,X,Y,Z,par,...
       var)
2
3  %The Matrix A is created on the big grid with/without IT ...
       aproach
4  if par.IT(1)==1
5  [var.A,var.Ih,var.pad]=conAIT(nx,ny,nz,k,d,k0,par);
6  else
7  [var.A,var.Ih,var.pad]=conA(nx,ny,nz,k,d,k0,par);
8  end
9
10 %Subroutine that calculates the nearfields is called and the ...
       absolute value of the nearfields is calculated
11 E=Nearfield(N,var,par,nz);
12 Eabs=sqrt(abs(E(1:N)).^2+abs(E((N+1):2*N)).^2+abs(E((2*N+1)...
       :3*N)).^2);
13
14 end
```

A.3.17 Nearfield.m

```
1  function [E] = Nearfield(N,var,par,nzb)
2  %This function calculates the nearfields an work similar like...
       AtimesP
3  %IF constructed that does the quasi-static substrate
4      if par.substrat_quasi(1)==1
5      %Some parameters are generated
6          P=var.Pze;
7          nz=ceil(nzb./2);
8          eps_sub=par.substrat_quasi(2);
9          nm=par.m_media;
10         Ref=(eps_sub-nm)./(eps_sub+nm);
11
12       %The polarization vector is flip and rearranges to ...
             reflect the quasi-static substrate
13       Px=P(1:N);
14       Px=reshape(Px,[],nz.*2+1);
15       Px(:,1:nz)=-1.*Ref.*fliplr(Px(:,nz+2:end));
16       P(1:N)=Px(:);
17
18
19       Py=P((N+1):2*N);
```

```
20      Py=reshape(Py,[],nz.*2+1);
21      Py(:,1:nz)=-1.*Ref.*fliplr(Py(:,nz+2:end));
22      P((N+1):2*N)=Py(:);
23
24
25      Pz=P((2*N+1):3*N);
26      Pz=reshape(Pz,[],nz.*2+1);
27      Pz(:,1:nz)=Ref.*fliplr(Pz(:,nz+2:end));
28      P((2*N+1):3*N)=Pz(:);
29     %Out put vector set to zero
30     E=zeros(size(P));
31     %The individual products are calculated by Atimesv and ...
           arranged accordingly
32     E(1:N)=var.Ein2(1:N)-(Atimesv(P(1:N),1,var)+Atimesv(P((N...
           +1):2*N),4,var)+Atimesv(P((2*N+1):3*N),5,var));
33
34     E((N+1):2*N)=var.Ein2((N+1):2*N)-(Atimesv(P(1:N),4,var)+...
           Atimesv(P((N+1):2*N),2,var)+Atimesv(P((2*N+1):3*N),6,...
           var));
35
36     E((2*N+1):3*N)=var.Ein2((2*N+1):3*N)-(Atimesv(P(1:N),5,...
           var)+Atimesv(P((N+1):2*N),6,var)+Atimesv(P((2*N+1):3*N...
           ),3,var));
37
38     Ihzer=zeros(size(var.I2));
39     Ihx=logical([var.I2;Ihzer;Ihzer]);
40     Ihy=logical([Ihzer;var.I2;Ihzer]);
41     Ihz=logical([Ihzer;Ihzer;var.I2]);
42
43     E(Ihx)=var.Elokor(var.I2).*var.Alpha2(var.I2).*P(Ihx);
44     E(Ihy)=var.Elokor(var.I2).*var.Alpha2(var.I2).*P(Ihy);
45     E(Ihz)=var.Elokor(var.I2).*var.Alpha2(var.I2).*P(Ihz);
46
47
48
49     else
50
51
52 %Out put vector set to zero
53 E=zeros(size(var.Pze));
54
55 %The individual products are calculated by Atimesv and ...
       arranged accordingly
56 E(1:N)=var.Ein2(1:N)-(Atimesv(var.Pze(1:N),1,var)+Atimesv(var...
       .Pze((N+1):2*N),4,var)+Atimesv(var.Pze((2*N+1):3*N),5,var)...
       );
57
58 E((N+1):2*N)=var.Ein2((N+1):2*N)-(Atimesv(var.Pze(1:N),4,var)...
       +Atimesv(var.Pze((N+1):2*N),2,var)+Atimesv(var.Pze((2*N+1)...
```

```
    :3*N),6,var));
59
60 E((2*N+1):3*N)=var.Ein2((2*N+1):3*N)-(Atimesv(var.Pze(1:N),5,...
    var)+Atimesv(var.Pze((N+1):2*N),6,var)+Atimesv(var.Pze((2*...
    N+1):3*N),3,var));
61
62 %Local field correction is done
63 Ihzer=zeros(size(var.I2));
64 Ihx=logical([var.I2;Ihzer;Ihzer]);
65 Ihy=logical([Ihzer;var.I2;Ihzer]);
66 Ihz=logical([Ihzer;Ihzer;var.I2]);
67
68 E(Ihx)=var.Elokor(var.I2).*var.Alpha2(var.I2).*var.Pze(Ihx);
69 E(Ihy)=var.Elokor(var.I2).*var.Alpha2(var.I2).*var.Pze(Ihy);
70 E(Ihz)=var.Elokor(var.I2).*var.Alpha2(var.I2).*var.Pze(Ihz);
71     end
72 end
```

A.4 Instrumentation

A.4.1 Raman microscope

All the Raman measurements in this thesis were done using the LabRAM HR 800 (with Olympus BX41) shown in figure A.9. For all measurements a laser wavelength of 633 nm (approximately 17 mW maximum power) filtered with an edge filter was used. The system is equipped with two gratings, a 300 lines/mm grating (spectral resolution approximately 2.6 cm^{-1}/pixel) which was used for all measurements were the spectral intensities are a concern and a 1800 lines/mm grating (spectral resolution approximately 0.35 cm^{-1}/pixel) which was only used for the precise determination of band positions in table 4.1. In addition the DuoScan^{TM} Imaging system is available for spectral mappings with variable pixel size. The detector used was a Peltier cooled 1024x256 pixel multichannel CCD detector.

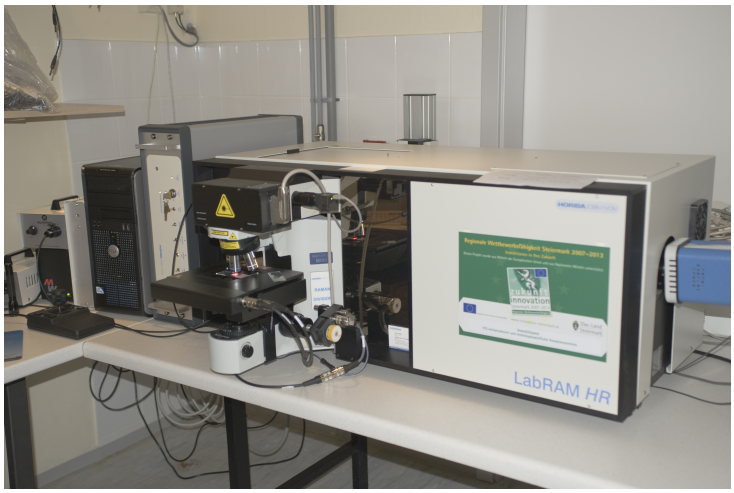

Figure A.9: Raman microscope: LabRAM HR 800 with Olympus BX41

A.4.2 Atomic force microscope

All AFM measurements were done using the Dimension FastScan Bio™ (Bruker) shown in figure A.10. The system is operated by a Nanoscpe V controller (Bruker Nano Surface) and is place in an acoustic enclosure as seen in figure A.10. The room the whole system (controller & enclosure) is operating in is air-conditioned to a temperature of 21 °C for stability. All measurements were performed using fresh MPP-12220-10 cantilever (Bruker AFM Probes), which feature a reflective aluminum caoting and a nominal spring constant of 5 N/m. The scan rate, set point, gain control and drive amplitude was monitored and optimized during the measurements. All data analysis and correction steps were performed using Gwyddion.

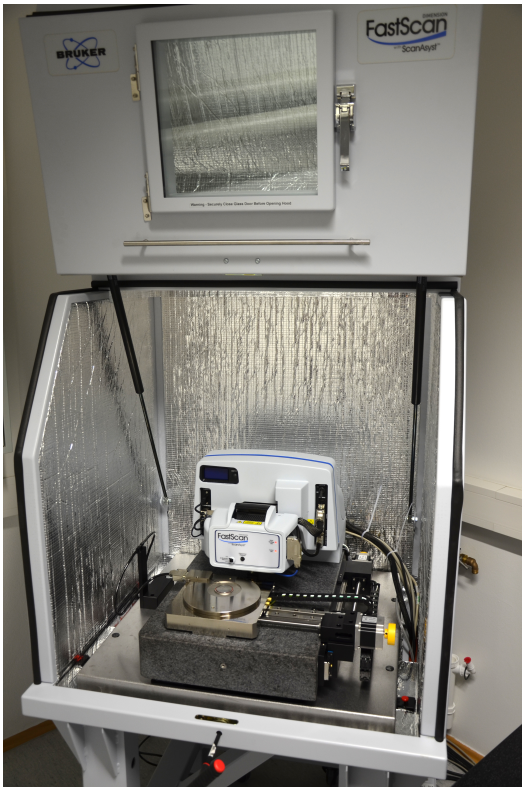

Figure A.10: Atomic force microscope: Dimension FastScan Bio™ (Bruker)

A.4.3 Scanning electron microscope

The SEM measurements were done using the environmental scanning electron microscope (ESEM) Quanta 600 FEG (FEI) shown in figure A.11. The system uses a thermally assisted field emission gun (FEG) and has three operational regimes. The regimes are high vacuum, low vacuum (10-200 Pa) and environmental (10-2000 Pa), of which the low vacuum regimes was used. The low vacuum regimes is especially suitable for the measurement of non conductive samples, because a cascade secondary electron detector (Large Field Detector) can be used to suppress surface charges (induced by the electron beam). The imaging gas was water vapor in all cases and in addition to the LFD-detector a solid state backscattered electron detector (SSD) was available and used.

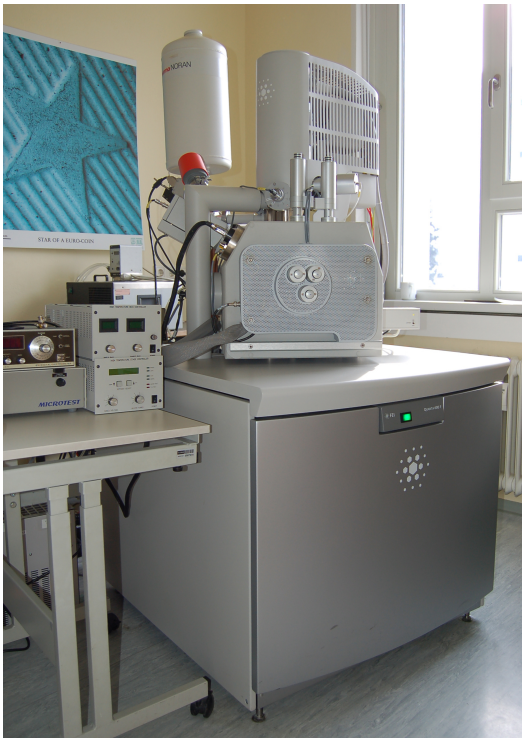

Figure A.11: Scanning electron microscope: ESEM Quanta 600 FEG (FEI)

A.4.4 Sputter coater

All sputter processes in this thesis were done using the EM ACE 600 (Leica) sputter coater shown in figure A.12 and using a highly pure Au sputter target (99.99% Ø 54 x0-2 mm, Leica). Argon was used for the sputter process itself, whereas the venting of the chamber was done using pure nitrogen gas. The EM ACE 600 uses a quartz crystal in the center of the rotating state to monitor the film thickness. For all sputter processes the pre-programmed pre-sputtering procedure (in order to clean the target) was used. The target position of the Au target was always on the right.

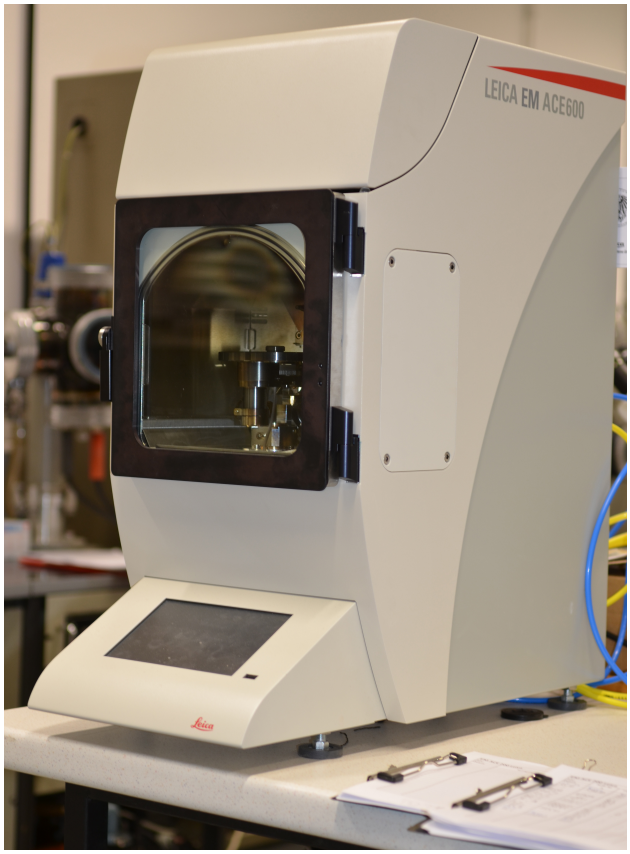

Figure A.12: Sputter coater: EM ACE 600 (Leica)

A.4.5 Computational resources

All computations that required large computational resources were done on the dedicated simulation sever shown in figure A.13. The available memory is 144 GB of RAM, which was also the limiting factor for the size of the simulated area (or total number of simulated dipoles). With regard to processing power two Intel® Xeon® CPUs with 3.07 GHz and 6 cores each. Note that no calculations in the script are done on the graphic board.

Figure A.13: Simulation server